2021

Incinerator Ash Characterization - Implications for Elevated Temperature Landfills

Angel Villarruel-Moore
University of Central Florida

INCINERATOR ASH CHARACTERIZATION – IMPLICATIONS FOR ELEVATED TEMPERATURE LANDFILLS

by

ANGEL VILLARRUEL-MOORE

B.S. University of Central Florida, 2019

A thesis submitted in partial fulfillment of the requirements
for the degree of Master of Science
in the Department of Civil, Environmental, and Construction Engineering
in the College of Engineering and Computer Science
at the University of Central Florida
Orlando, Florida

Summer Term

2021

Major Professor: Debra R. Reinhart

ABSTRACT

The occurrence of temperatures in municipal solid waste (MSW) landfill gas (LFG) extraction systems in excess of 55°C is a problem that has gained much attention in the solid waste industry, both domestically and globally. Facilities which frequently experience such temperatures are termed Elevated Temperature Landfills (ETLFs), and recent research conducted at the University of Central Florida (UCF) has provided strong evidence that ash, both MSW incinerator ash (MSWIA) and coal combustion ash (CCA), when co-disposed with unburned MSW, provides materials which are able to participate in abiotic exothermic reactions that may lead to the development or sustainment of ETLFs. These reactions include ash hydration and carbonation, as well as the oxidation and corrosion of metals commonly found in ash.

Over the course of this project, sixteen ash samples from across the U.S. were analyzed (ten MSWIAs and six CCAs) using spectroscopic and thermal analyses. X-ray diffraction (XRD), x-ray fluorescence (XRF), and scanning electron microscopy coupled with x-ray dispersive elemental spectroscopy (SEM/XEDS) provided insight into ash compositions, while thermal gravimetric analysis (TGA) shed light into the sensitivity of ashes to changes in temperature. Results from this project reveal that the high-temperature incineration of MSW and coal feedstocks, as well as weathering processes impacting these ashes, yields a heterogenous material with many complex mineral and glassy phases. A simple heat-generation equation was developed and, using ash compositions obtained via XEDS, a value termed relative heat potential (RHP) was calculated for each sample. Results show that CCAs may be expected to generate roughly 15% more heat than MSWIAs when deposited in landfills, likely due to their greater aluminum content.

ACKNOWLEDGEMENTS

First and foremost, I would like to extend my deepest gratitude to Dr. Reinhart, Dr. Sohn and everyone at the Environmental Research & Education Foundation (EREF) for providing me with this wonderful opportunity to further my education – this journey has meant more to my family and I than I can probably express. I would also like to thank my colleagues from the laboratory for Advanced Materials and Additive Manufacturing (AM^2) for their support in 'showing-me-the-ropes' when it came to sample preparation and analysis. I would like to extend a special thank you to Thinh Huynh, Kevin Graydon, Dr. Abhishek Mehta, and Dr. Holden Hyer for their patience in trainings and guidance regarding material characterization.

To my siblings, father, and mother – I will always owe all of my successes to you. Without the never-ending love and support from my family, I would not be the man I am today. And to my newlywedded wife, Chloe, thank you for supporting me through the toughest of times. This has been a wild journey, and I cannot tell you how grateful I am for the love and laughter that we have shared throughout these past few years.

TABLE OF CONTENTS

LIST OF FIGURES

LIST OF TABLES

CHAPTER 1 INTRODUCTION

Recent research conducted at the University of Central Florida (UCF) has shown that municipal solid waste incinerator ashes (MSWIAs) and coal combustion ashes (CCAs) may prove troublesome for landfill operators when co-disposed with unburned waste in typical RCRA Subtitle D landfills (Joslyn, 2019). In his study, Joslyn found that there was a strong correlation between Florida landfills which accepted combustion ashes (both MSWIAs and CCAs) and landfills that experienced temperatures in their landfill gas (LFG) extraction systems which were above the permitted limit of 55°C (131°F) established in the Code of Federal Regulations (40 CFR § 60.753). LFG temperatures greater than 55°C could be indicative of elevated temperatures in the bulk MSW itself, and landfills with consistently high temperatures are referred to as Elevated Temperature Landfills (ETLFs). When MSW temperatures are too high, the naturally occurring biological processes may be interrupted due to the formation of conditions which favor thermophiles and inhibit methanogens, thus reducing a landfill's ability to generate methane (Meyer-Dombard et al., 2020; Schupp et al., 2020). Additionally, high temperatures in landfills can negatively impact the quality of leachate produced at these landfills, potentially damage the protective geomembrane liner and landfill gas extraction systems, degrade air quality, and initiate undesired waste settlement (National Resource Council, 2000; Calder and Stark, 2010; Jafari et al., 2017; Benson, 2017). The solid waste industry has expressed great interest in identifying, modelling, and remedying the factors which can lead to the onset and development of ETLFs (Hao et al., 2017).

It is well known that, on average, municipal solid waste (MSW) is being generated at increasing rates in the United States (U.S.). The U.S. Environmental Protection Agency (USEPA) reported that the U.S. experienced nearly a 10% increase in total MSW generation between 2017 and 2018, which translated to roughly 292.4 million tons of MSW generated throughout the country in 2018 (USEPA, 2020). The fate of generated MSW varies considerably, with some waste being landfilled directly, some recycled into products for alternative applications, and some incinerated for energy recovery at facilities termed 'waste-to-energy' (WTE) plants. The combustion process provides many benefits to traditional landfilling, such as the ability to achieve large (around 90%) volumetric reductions prior to final disposal and the ability to recover energy (Psomopoulos et al., 2009; U.S. EPA, 2020). WTE plants, however, generate additional waste streams in the form of MSWIAs and, while some of this material can be reused in construction and transportation applications, there is still a considerable fraction which requires final disposal in MSW landfills or ash monofills (Bertolini et al., 2004; Lynn et al., 2017; Clavier et al., 2021). CCAs produced from power generation are an additional ash source which requires beneficial reuse or final disposal. In 2019 alone, approximately 80 million tons of ash were generated in the U.S., but nearly half were reused in construction and building applications (Adams 2019, American Coal Ash Association). Despite this ~50% reutilization rate for all CCAs generated, an appreciable amount of ashes (combined MSWIAs and CCAs) is still deposited in landfills annually, and these ashes provide reactants which are known to partake in exothermic reactions that may promote ETLF development and sustainment (Hao et al., 2017; Joslyn, 2019).

It is the scope of this project to both provide a deeper understanding into the composition of combustion ashes produced domestically in the U.S. and to investigate the potential heat-generating interactions associated with ashes co-disposed with unburned MSW in typical Subtitle D landfills. Spectroscopic techniques like x-ray diffraction (XRD), x-ray fluorescence (XRF) and x-ray elemental dispersive spectroscopy (XEDS) were employed to understand the variability in chemical composition across ashes generated via different combustion schemes, while thermal gravimetric analysis (TGA) was performed to understand how susceptible ashes were to changes in temperature in a controlled environment. Chemical and physical properties including pH and particle size were also investigated for most ash samples. Ultimately, a Monte Carlo analysis was performed using the generated spectroscopic data and published exothermic reactions (hydration, carbonation, corrosion, etc.) relevant to CCAs and MSWIAs. The findings of this project shed light into the heat-generating potential for six CCAs and ten MSWIAs from facilities throughout the U.S..

CHAPTER 2 LITERATURE REVIEW

2.1 Ash Generation and Processing Techniques

Of the total 292.4 million tons of MSW generated in the U.S. in 2018, roughly 12% (34.5 million tons) was combusted for the purpose of energy recovery (U.S. EPA, 2020). MSWI facilities drastically reduce the amount of material sent to landfills, achieving up to a 70% reduction on a mass basis and 90% reduction on a volumetric basis (Alba et al., 1997; Lam et al., 2010). Despite the benefits of waste minimization and energy production, MSWI facilities generate additional waste streams in the form of bottom ash (BA), fly ash (FA), and other air pollution control (APC) residues which still require reuse or final disposal. BA is the fraction of combusted MSW that is comprised of unburned organic material, inorganic particles, and large remnants of metals, glass, and ceramics, all of which settle down through the grates of the combustion chamber. FA, on the other hand, is the finer fraction which is emitted with the flue gas and is removed via APCs. FA tends to contain fine particles of volatile metals and condensed acids and may be enriched in added reagents like lime or activated carbon for APC (National Resource Council, 2000). APC residues vary depending on the nature of the control in place (e.g., baghouse filters, electrostatic precipitators, acid-gas scrubbers) and are collected after the addition of a sorbent to aid in pollutant removal (Phua et al., 2019). In the U.S., all three of these ash streams are typically mixed to create a single stream termed ‘combined ashes’ and are frequently landfilled together (An, 2015). Although the feedstocks vary considerably compared to MSWI facilities, coal combustion power plants generate the same types of ash streams (FA, BA and APC residues). In a 2019 report, the American Coal Ash Association (ACAA) reported that 78.6 million tons of coal ash were produced from combustion processes in the U.S., but only

37.6 million tons required disposal at landfills or ash monofills while the remaining 40 million tons were beneficially utilized in concrete, cement, and other applications (Adams 2019, American Coal Ash Association).

After ash is generated, various treatment schemes are employed aimed at reducing the environmental impact associated with its disposal. As BA exits the combustion chamber via conveyors, it is typically quenched in water to both reduce its temperature and to help mitigate dust formation during subsequent storage and transportation. Water quenching affects ashes by encouraging the formation of hydration (quench) products like portlandite and hydrocalumite, decreasing the pH and increasing specific surface area (Inkaew et al., 2016). Solidification and stabilization (S/S) methods are also available for ash treatment, but these methods often require the addition of chemicals or binders, like Portland cement, to promote reactions which physically immobilize target ash constituents. Another downfall of S/S techniques are that they often increase the amount of waste requiring disposal, with some S/S methods increasing the waste volume by 50% (Lam et al., 2010). Some countries opt to apply thermal methods, like vitrification or sintering, to further treat FA. These high-temperature thermal methods can create a homogeneous glassy slag with notably reduced volume (up to 60% reduction), toxic organic content and heavy metal leachability (Lam et al., 2010). Some constraints of thermal methods are the high energy costs associated with melting fly ashes at high temperatures (1300-1450°C) and ensuring the operation has adequate corrosion prevention due to the high chloride levels associated with these ashes (Liu et al., 2009). Some research has been conducted to investigate the influence of natural weathering on ash composition. For example, initial weathering periods has been shown to convert unstable metals (Al, Fe and Cu) and minerals (lime, ettringite and

hydrocalumite) to more stable oxide and hydroxide phases (Saffarzadeh et al., 2011). Intermediate weathering can further modify ash compositions by promoting the dissolution of melt products which are enriched with metallic particles. Many of these post-processing techniques are applied to ashes to improve their applicability in construction and transportation projects, but their impacts on ash heat-generating potential in a landfill environment has not been documented.

2.2 Ash Composition

MSWIAs and CCAs compositions are well documented in literature (Alba et al., 1997; Chimenos et al., 1999; Speiser et al., 2001; Chancey, 2008; Liu et al., 2009; An, 2015; Phua et al., 2019). Considerable variation in ash composition exists because of the specifics of the combustion process, for example, which APCs are in place and whether ferrous and non-ferrous metal recovery is performed, but there are many similarities among the ash groups. For typical MSWI facilities, BA tends to be generated in the largest fraction (85%) followed by FA (5%) and APCs (10%) (Phua et al., 2019). BAs tend to contain the largest concentration of iron and other metals with low volatility, while aluminum appears largely in the FA and APC fractions for the opposite reason (Alba et al., 1997). BAs also have been found to be comprised primarily of oxides of silicon, calcium, and iron (Speiser et al., 2001). On the other hand, the dominant oxides for FAs are calcium, silicon, and aluminum while APC residues are dominated not only by oxides of calcium and aluminum, but also by chlorine-bearing mineral phases (Phua et al., 2019). Because FAs and APC residues contain greater concentrations of toxic heavy metals, condensed acid phases, chlorine, and aluminum, they typically require additional treatment prior to reuse in construction projects or final disposal (outside the U.S.) (Bertolini et al., 2004; An, 2015).

Despite these general trends, the complex nature of the incineration process yields ash particles with heterogenous compositions which can make detailed characterization efforts difficult.

2.3 Characterization Techniques

While there exists extensive literature regarding the characterization of incinerator ashes (both MSWIAs and CCAs), there has been little research conducted regarding the implications of ash disposal and heat generation in conventional landfills. One prominent characterization technique that has shown great promise in the fields of mineralogy and materials engineering, particularly for crystalline phases, is x-ray diffraction (XRD). XRD allows for the identification of an unknown sample by simultaneously bombarding the sample's surface with incident x-rays and measuring the location and intensity of the resulting diffracted x-rays via an x-ray detector. The intensity of the measured (diffracted) x-rays are displayed as a function of scan angle ($2\theta°$), and the resulting peaks are characteristic of the crystalline phases present in the sample. These plots can then be analyzed using a database, such as the International Centre for Diffraction Data (ICDD), to determine exactly what crystalline phases are present. Typical XRD results for MSWIAs and CCAs show complex mineralogical compositions with large fractions of amorphous (non-crystalline) components (Kirby and Rimstidt, 1994; Chancey, 2008; Liu et al., 2009; Wei et al., 2011; Phua et al., 2019).

X-ray fluorescence (XRF) is a bulk analytical tool that is often associated with XRD, and both XRF and XRD are non-destructive analytical tools meaning that the same material can be further analyzed with alternative techniques. Like XRD, XRF operates via irradiating a sample with x-rays and measuring the generated fluorescent x-rays which are characteristic of the sample. Unlike XRD, XRF cannot grant insight into the exact speciation of the sample, but rather

gives a general idea of what elements are present. XRF provides quick characterization results which can aid in the identification phase of XRD analysis, although the exact concentrations obtained via XRF are not as reliable as some of the other techniques described in this section.

Scanning electron microscopy coupled with x-ray energy dispersive spectroscopy (SEM/XEDS) is another promising tool to aid in the characterization of combustion ashes. SEM operates on the principle of bombarding a sample with electrons instead of x-rays. The incident electrons enter a sample and, based on the nature of the material, backscattered electrons (BSEs) and secondary electrons (SEs) are emitted and measured via an electron detector. BSEs originate from deeper regions of a sample and tend to highlight compositional differences, with elements of higher atomic weight appearing lighter in color and low atomic weight elements appearing darker. SEs, on the other hand, are generated near the sample's surface and thus provide excellent details of a sample's topography and other surface defects. While SEM is powerful in its own right, characterization efforts are greatly improved when SEM is used in conjunction with XEDS. Here, an x-ray detector measures the characteristic x-rays generated when electrons from the sample fill the vacancies created by emitted BSEs and SEs. When conducted properly, SEM/XEDS can provide accurate quantitative compositional information for a prepared sample. In terms of the characterization of MSWIAs and CCAs, XEDS tends to be one of the more common analytical techniques and can provide detailed information regarding the exact speciation of ash particle components (Chancey, 2008; Wei et al., 2011; Saffarzadeh and Shimaoka, 2014; Saffarzadeh et al., 2016).

Literature regarding the thermal response of incinerator ashes is more limited than for SEM/XEDS and XRD/XRF, especially as it relates to thermal gravimetric analysis (TGA). TGA operates on the principal of heating up a small sample in a controlled environment and simultaneously measuring the mass change, with mass gains associated with processes like oxidation and mass losses associated with the thermal degradation of select compounds. Typically, TGA is conducted in conjunction with differential scanning calorimetry (DSC) to also measure the heat generation or consumption that occurs as a result of the controlled heating. Unfortunately, a DSC cell was unavailable for our analysis. TGA has been applied by various researchers to study the effects of MSWIAs and CCAs as additives for concrete and aggregate production, and results highlight the temperature ranges associated with the decomposition of compounds like carbonates and hydroxides (Wang et al., 2004; Pane and Hansen, 2005; Santos et al., 2013). Knowledge of these temperature ranges can allow for the identification of hydration and carbonation products present in incinerator ashes, which may grant insight into the potential reactivity of MSWIAs and CCAs when disposed of in landfills. Although the exact temperature range varies in literature, it is widely agreed that calcium carbonate ($CaCO_3$) and calcium hydroxide ($Ca(OH)_2$) have been shown to thermally degrade approximately between the temperature ranges of 600-780°C and 440-520°C, respectively (Wang et al., 2004; Pane and Hansen, 2005; Felipe-Sesé et al., 2011; Narode et al., 2021).

Physical and chemical analysis of ashes are also well documented, especially with regards to ash pH and particle size. Incinerator ashes, especially FAs and APC residues, tend to be highly alkaline (pH>9) as a result of additives like lime and sodium bicarbonate, which are used to improve the efficiency of flue gas treatment (Saffarzadeh et al., 2011; Saffarzadeh et al.,

2016). The elevated pH of ashes can play an important role in ash speciation and may dictate what subsequent exothermic reactions take place (Calder and Stark, 2010). The particle size of MSWIAs and CCAs differ slightly as well, with coal combustion producing finer ashes on average (Chancey, 2008; Yu et al., 2013). Regardless of the type of incineration performed, BAs tend to be larger in size compared to FAs and APC residues. This may have implications for reactivity, as finer particles have a greater surface area available to partake in exothermic reactions.

2.4 Heat-Generating Reactions

Due to the negative effects associated with ETLFs, there has been a surge in research aimed at identifying exothermic reactions and conditions requisite for ETLF formation (Grillo, 2014; Hao et al., 2017; Reinhart et al., 2020; Tupsakhare et al., 2020). Although there are documented exothermic biotic processes in landfills – such as the hydrolysis of organics and anaerobic methanogenesis – incinerator ashes appear to partake in abiotic reactions, and these abiotic reactions tend to dominate biotic reactions at elevated temperatures because of inhibition of the microbes responsible for biodegradation processes (Meyer-Dombard et al., 2020; Schupp et al., 2020). Some abiotic reactions of interest are the hydration of oxides formed in the combustion chamber, the subsequent carbonation of newly-formed hydroxides, and the oxidation and corrosion of metals (Calder and Stark, 2010; Hao et al., 2017; Joseph et al., 2018). After their deposition at landfills or ash monofills, there are additional alteration processes which influence the speciation of ash (Speiser et al., 2000; Saffarzadeh et al., 2014). Examples of these transformative processes include cementitious reactions and the dissolution or precipitation of salts, all of which yield new mineral phases with complex compositions. The stability of these

new mineral phases will likely affect the heat-generating potential of ash at different timescales, as there may be some destabilization of the passivating layers protecting ash particles. If these passivating layers are removed or damaged, then the reactive components of materials previously considered inert may become exposed and available for exothermic reactions. Examples of these destabilization processes are the corrosion of heavy metal-bearing glassy phases (Si, Ca, Fe and Al released), the dissolution of lime and portlandite (Ca released), and the corrosion of metallic particles (Fe, Zn and Cu released) (Speiser et al, 2000).

2.5 Summary

As MSW continues to be generated at increased rates in the U.S., and as coal continues to be used as a feedstock for power generation, the quantity of MSWIAs and CCAs disposed of in landfills is expected to remain high. Characterization techniques like XRD, XRF, and SEM/XEDS have been successfully conducted on various MSWIAs and CCAs throughout the world, and results prove that incineration yields ashes with complex compositions that are susceptible to transformation and alteration processes as a result of disposal practices and landfill environments. In recent years, there has also been a rise in research projects aimed at identifying key exothermic reactions and environmental conditions that result in ETLF formation. However, while recently published heat-generating models account for abiotic reactions concerning incinerator ashes, they do not account for the variability in ash composition resulting from different operating parameters at various incineration facilities (Hao et al., 2017). Thus, there is a need for site-specific ash compositions from incineration facilities across the U.S. to gain a deeper understanding about heat-generating potential of MSWIAs and CCAs when disposed of with raw MSW in traditional landfills.

CHAPTER 3 EXPERIMENTAL METHODOLOGY

3.1 Sample Overview and Preparation

In total, six CCAs and ten MSWIAs were investigated over the course of this project. The large number of samples allowed for the characterization of MSWIAs and CCAs from facilities with different incineration technologies, metal recycling practices, and APCs. An overview and brief description of all samples is provided in Table 1. Samples CCA 1-5 and MSWIA 1-5 were initially received and processed at North Carolina State University (NCSU) as part of a joint research effort, while the remaining samples were received and processed at the University of Central Florida (UCF). Samples were processed as required to prepare them for characterization, but because of some differences in composition between MSWIAs and CCAs the initial processing methods differed slightly. CCA samples were first sieved (ASTM-C136) using a 16 mm (5/8 in) screen to separate the samples into coarse and fine fractions. A sand splitter was then used with 1-in openings to divide the fine fraction into halves. One half of the split sample was again added to the sand splitter, and this process was repeated until a representative sample of the desired size was obtained. For MSWIAs, ash samples were first emptied into large pans and thoroughly mixed. Large particles were manually crushed to roughly 2.5 cm (1 in) in size, while pieces larger than 5 cm were removed to prevent damage to the mechanical equipment used in a later step. The remaining material was added to a sand splitter (ASTM-C702) with 4-in chute openings, and one half of the split sample was again added to the splitter until a quarter of the original ash sample was remaining and could be further processed. The remaining sample was then dried in an oven at 80°C for 48 hours, and pieces were again manually crushed until the sample was approximately 1 cm in size. The sample was then added to a Wiley Mill to

mechanically crush the sample, first using a 3 mm screen. The material passing through this 3-mm screen was re-added to the Wiley Mill with a 1 mm screen to obtain a final, representative sample. CCA-6 and MSWIA-6 through 10, were processed slightly differently at UCF. CCA-6 did not contain any large particles which needed removal or crushing; thus, the sample was sieved through a ½ in screen and a representative sample was obtained using the Cone-and-Quartering method (ASTM-C702). MSWIA-6 through 10 were processed similarly to CCA-6, except that there was a need for manually crushing some larger particles which passed through the ½ in screen (see Figure 1). Crushing was performed using a hammer and mortar and pestle until the ash appeared homogeneous and could be analyzed using the characterization methods discussed in Chapter 3. Representative subsamples were then heated at 100°C for at least 30 mins prior to further analyses.

Table 1: Sample Overview

Sample ID	Description
CCA-1	Class C fly ash collected in an ESP at a subcritical pulverized coal power station
CCA-2	Bottom ash collected dry at a subcritical pulverized coal power station
CCA-3	Class C fly ash with sodium carbonate and powdered activated carbon injection collected in a BF at a subcritical pulverized coal power station
CCA-4	Class F fly ash with hydrated lime injection and powdered activated carbon injection collected in a BF at a supercritical pulverized coal power station
CCA-5	Fly ash from a BF with hydrated lime injection at a CFB power station
CCA-6	An aged coal ash + WWTP biosolids mixture
MSWIA-1	Combined ash with little/no aluminum recovery and dolomite addition
MSWIA-2	Combined ash with little/no aluminum recovery
MSWIA-3	Combined ash with aluminum recovery and dolomite addition
MSWIA-4	Combined ash with aluminum recovery
MSWIA-5	Combined ash with high lime rate addition
MSWIA-6	Bottom ash from a WTE facility practicing RDF with no aluminum recovery and some ferrous metal recovery
MSWIA-7	Fly ash from a WTE facility practicing RDF with no aluminum recovery and some ferrous metal recovery; collected from BF and acid gas scrubber
MSWIA-8	Bottom ash from a WTE facility practicing MB with no aluminum recovery and some ferrous metal recovery
MSWIA-9	Fly ash from a WTE facility practicing MB with no aluminum recovery and some ferrous metal recovery; collected from BF and acid-gas scrubber
MSWIA-10	Combined ash from WTE facility practicing ferrous and non-ferrous metal recovery

Note: **BF** – Baghouse Filter; **CFB** – Circulating Fluidized Bed; **ESP** – Electrostatic Precipitator; **MB** – Mass Burn; **RDF** – Refuse Derived Fuel; **WTE** – Waste to Energy; **WWTP** – Wastewater Treatment Plant. **Hydrated Lime** ($Ca(OH_2)$); **Dolomite** – Dolomitic Limestone ($CaCO_3 \bullet MgCO_3$).

Figure 1: Processing Efforts Conducted at UCF for Sample MSWIA-10.

Note: Coarse and fine fractions separated via the 1/2in screen are evident, and the pictured fine fraction was subsequently cone-and-quartered to obtain a representative subsample.

3.2 pH and Particle Size Analysis

The pH of all ash samples was determined according to EPA Method 9045d, which calls for 20 g of ash mixed with 40 mL of de-ionized (DI) water. The sample was mixed for 5 mins and allowed to settle for 15 mins, after which the pH of the resulting supernatant was measured (see Figure 2). The pH was measured using an Oakton pHTestr 30 handheld probe.

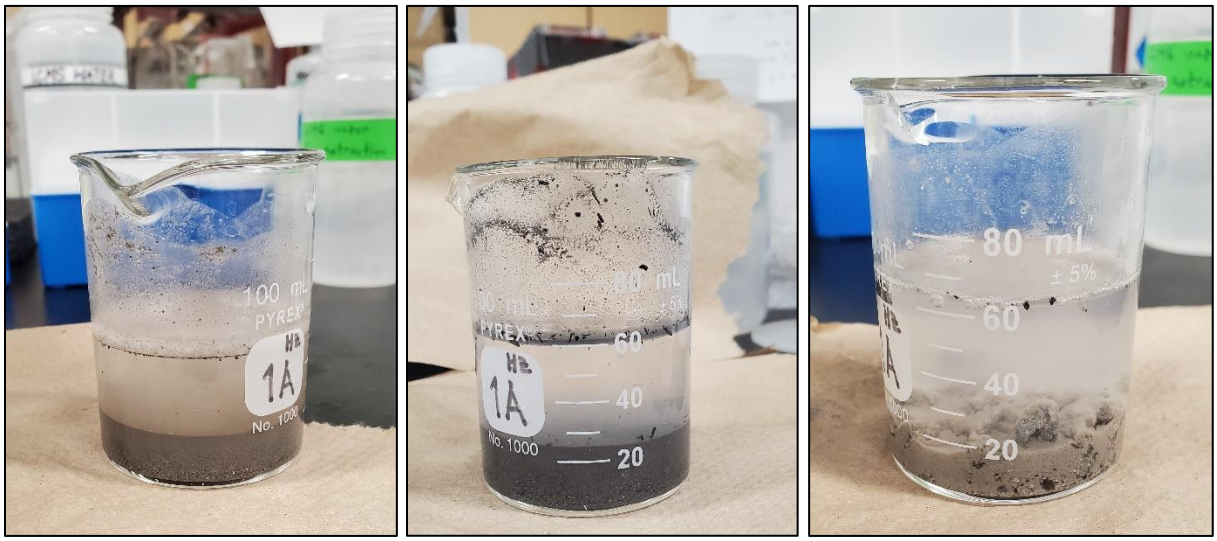

Figure 2: Image of Samples Following 15min Settling Period. Pictured left-to-right: CCA-2→ MSWIA-9 → MSWIA-10

Particle size analysis (PSA) was performed on ashes using a Beckman Coulter LS 13 320 Laser Diffraction Particle Size Analyzer (Figure 3). The LS 13 PSA identifies the size and distribution of particles ranging from 0–2000 μm. For analysis, a small amount of ash was placed in a sample tube which is placed in the PSA. Prior to analysis, samples were dried to ensure that moisture did not cause particles to 'clump' together within the PSA.

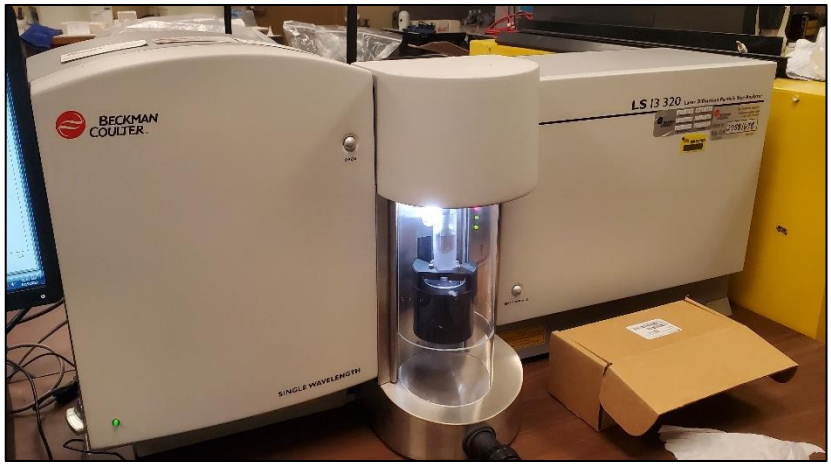

Figure 3: Beckman Coulter LS 13 Particle Size Analyzer (PSA)

3.3 Thermal Response Analysis

The thermal response of ashes was determined via thermal gravimetric analysis (TGA). TGA was performed using a TA Instruments 2950 TGA (see Figure 4) with the help of the Blair Research Group at UCF to develop the analytical method. Roughly 100 mg of ash was placed in an alumina sample pan and heated from room temperature (25°C) to 900°C at a rate of 10°C/min with oxygen as the carrier gas. Care was taken to ensure that the instrument was properly calibrated prior to each analysis, and the equipment was allowed to cool back down to room temperature prior to analyzing the next sample. After each analysis, the alumina sample pan was cleaned using a steel dental scraper to remove any remnants of analyzed ash – the alumina pan was replaced roughly every four experiments due to a buildup of ash remnants. Following the experiment, the TA Analyzer software was utilized to generate curves of both weight loss (mg) and first derivative weight loss (%/°C) as a function of temperature (°C).

Figure 4: TA Instruments 2950 Thermal Gravimetric Analyzer (TGA)

3.4 Spectroscopic Analysis

XRD and XRF analyses were performed simultaneously at the Materials Characterization Facility (MCF) at UCF. Since XRF is a bulk analytical tool, a sample cylinder was filled with dried ashes and analyzed using a PANalytical Epsilon XRF spectrometer. This spectrometer is equipped with a 50kV silver anode that allows for the rapid (roughly 5 mins) detection of elements with atomic numbers of 11 (Na) and greater. XRF concentrations (units of atomic weight %) are reported as either pure elements or as oxides, but for this project the pure metal option was selected since the exact composition of ashes was unknown (for example calcium could be present as an oxide, hydrate, silicate, or some other complex mineral phase). The XRD equipment used was a PANalytical Empyrean X-Ray Diffractometer with a 1.8 kW copper x-ray tube (Figure 5). For some ashes, milling was required to ensure that a plane surface could be achieved when loaded into the sample holder. Typical experimental parameters include a scan range of 10-70° (2θ), a step size of 0.03°, a rotation speed of 2 rev/sec, and a time per step of 90 sec. While the masks and divergence slits applied varied slightly, a fixed incident beam mask of 10 mm, an anti-scatter slit of 1°, and a divergence slit of 1° were typically used. No nickel (Ni) filter was used. Data generated via XRD display diffracted x-ray intensities (counts) as a function of scan angle (2θ°); the HighScorePlus software was utilized to perform phase identification using the International Centre for Diffraction Data (ICDD) database. During phase identification, XRF data were used as an initial reference to determine which mineral phases were present in the ash samples, and results were checked against literature for further verification. Because XRD and XRF are non-destructive analytical instruments, each sample was preserved after analysis to be later mounted and polished for SEM and XEDS work.

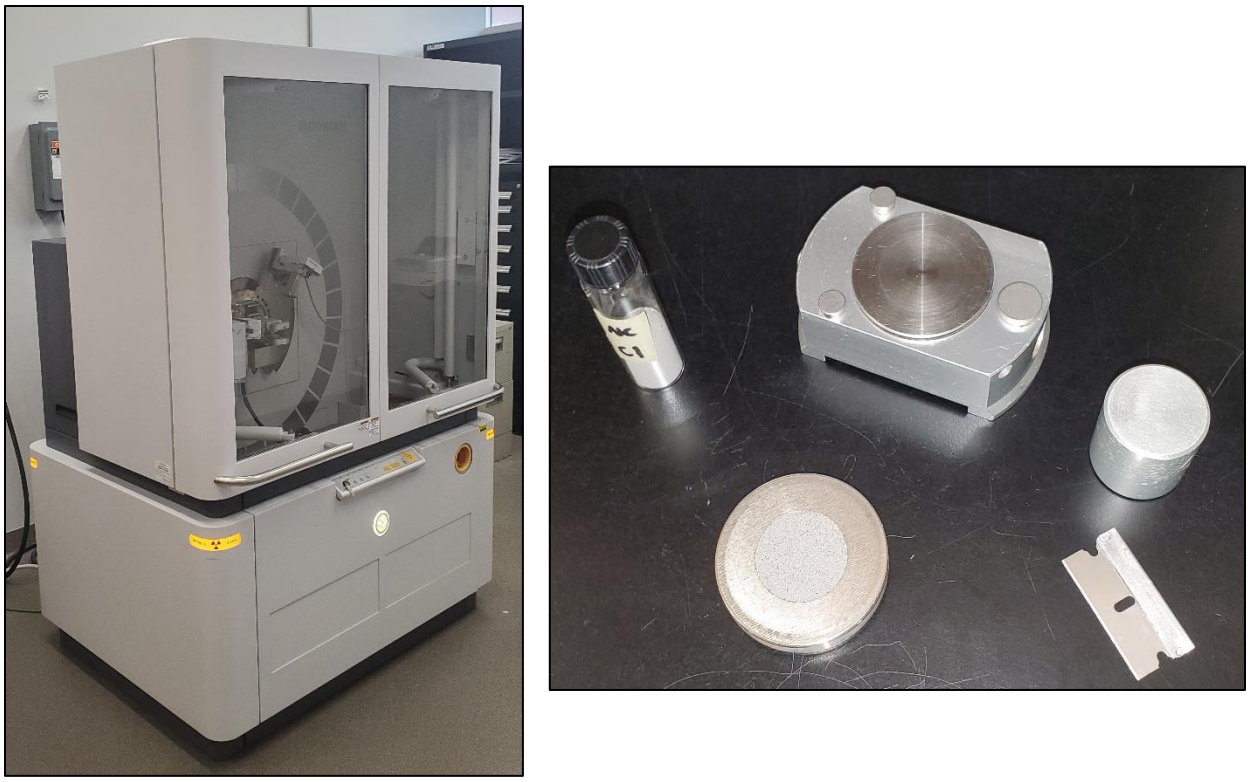

Figure 5: PANalaytical Empyrean X-Ray Diffractometer at UCF's MCF (left) and an Example of a Prepared Sample for XRD Analysis (right)

SEM and XEDS required slightly more preparation prior to analysis. A cylindrical sample mold was first coated with a few drops of epoxy release agent and dried with a heat gun. Dried ash from previous XRD and XRF work was then added to these molds and set aside. In a separate apparatus, a specific amount of epoxy resin and hardener were mixed gently to avoid any excess air entrapment. Once the epoxy mixture was opaque and completely mixed, a small amount was poured into the sample cylinder with ash to create a layer with an initial thickness of roughly 1 mm. This layer was thoroughly mixed and allowed to sit for 30 mins. After this waiting period, the remainder of the epoxy resin and hardener solution was added to the cylindrical mold and the sample was cured at room temperature for at least 8 hrs. Then, the samples were removed and prepared according to typical metallurgical practices using an Allied

MetPrep grinder. Initial grinding was conducted using silicon carbide (SiC) grinding papers in ascending grit units (400, 600, 800, and 1200) using low force (4-8 N) with ethanol as the lubricant. Grinding was typically conducted over 90 sec intervals and progress was checked using an optical microscope to ensure that scratches were being effectively removed. After grinding with a 1200 grit paper, a final polish was achieved using a Buehler magnetic polishing cloth embedded with a 1-μm diamond abrasive using mineral oil as the lubricant. After the final polish, the sample was placed in a beaker with ethanol and cleaned with an ultrasonic bath. Prior to SEM analysis, each sample was sputter coated with a thin layer of gold (~10nm) and carbon tape was used to help adhere the sample to the SEM sample mount – both measures minimize the effects of 'charging' which occurs due to a buildup of electrons on the sample's surface. SEM analysis was conducted using a field-emission SEM (Zeiss Ultra-55^{TM}) at UCF's MCF (see Figure 6). This SEM is equipped with in-lens secondary electron (SE) and backscattered electron (BSE) detectors. For XEDS analysis, a 60 μm aperture was used with an electron voltage of 30 kV and a working distance of 13.1 mm. Elemental analysis was determined via XEDS using at least 3 random locations across the polished sample's surface and concentrations were averaged to achieve a representative ash composition. This SEM is configured with ThermoFisher Scientific's Noran System 7 (NSS) software, which generates XEDS data via Point-and-Shoot and Spectral Imaging functions.

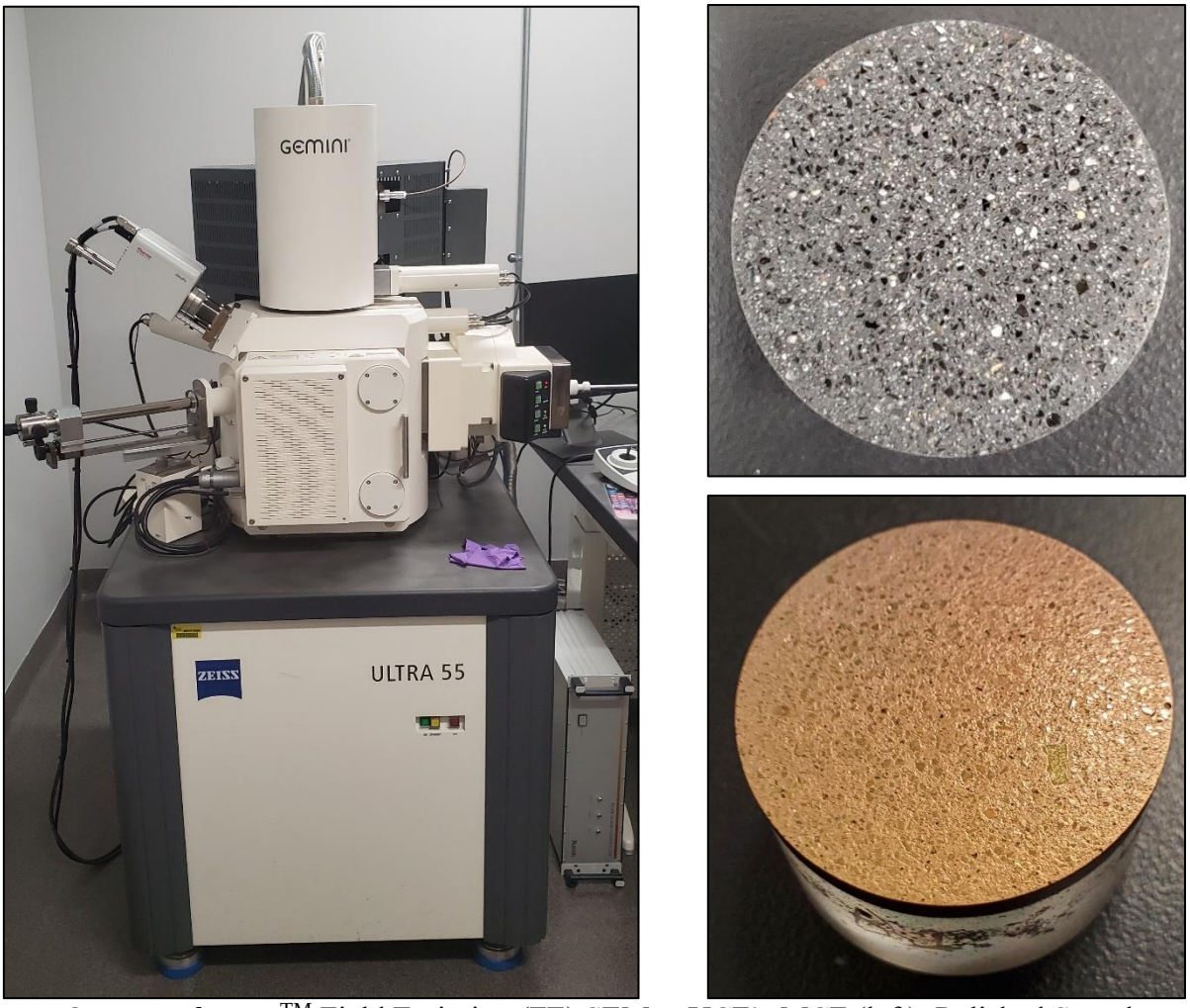

Figure 6: Zeiss Ultra-55™ Field Emission (FE) SEM at UCF's MCF (left); Polished Sample Before (top-right) and After (bottom-right) Gold Deposition for SEM and XEDS Analysis

3.5 Modelling Efforts

Thermodynamic modelling was performed via a Monte Carlo simulation using Oracle Software's Crystal Ball Excel add-in. For this analysis, XEDS data and published exothermic reactions relevant to incinerator ashes were used to generate a value called Relative Heat Potential (kJ/kg Ash) for ash samples according to equation (1).

$$\boldsymbol{Relative\ Heat\ Potential}\left(\frac{kJ}{kg\ Ash}\right) = \sum \boldsymbol{C_i}\left(\frac{kg\ Element}{kg\ Ash}\right) \times \Delta \boldsymbol{H_{rxn,i}}\left(\frac{kJ}{kg\ Element}\right) \times \boldsymbol{f_i} \qquad (1)$$

Here, C_i is the concentration of element *i* determined via XEDS, $\Delta H_{rxn,i}$ is the enthalpy of a reaction relevant to element *i* obtained from literature (Calder and Stark, 2010; Hao et al., 2017; Narode et al., 2021), and f_i is the fraction of element *i* available for any given reaction. The Monte Carlo analysis performs many iterations (n=25,000) where the given parameters are varied according to user-defined statistical distributions. Concentrations varied with normal distributions based on averages and standard deviations obtained via XEDS, while the enthalpies of reaction were held constant. The fractions available for reaction were specific to the reaction type and element of interest, and values were determined based on assumptions. A summary of reactions and associated enthalpies can be found in Table 2 and a summary of fractions used can be found in Table 3. The fraction available for hydration (f_{hyd}) was defined with the assumption that a small amount of ash (roughly 30%) was already hydrated prior to disposal at a landfill, either due to ash quenching or environmental factors. The fraction available for carbonation (f_{carb}) was assumed to be high because of the abundance of CO_2(g) found in landfill environments and the sequential nature of hydration and carbonation reactions. Al and Fe found in ashes were expected to be largely oxidized and corroded prior to disposal in a landfill, but there may be some mechanisms (both physical and chemical) after disposal which destabilize the passivating metal oxide layers surrounding Al- and Fe-bearing particles. If these passivating layers are removed, then the Al and Fe may participate in highly exothermic reactions as illustrated in Table 2. There is a parameter in the field of metallurgy known as the Pilling-Bedworth ratio which highlights differences in stability of various metal oxides. Al_2O_3 is considered a fairly stable oxide based on this metric while Fe_2O_3 is considered unstable. Hence, the fractions available for aluminum ($f_{corr,Al}$, $f_{oxid,Al}$ and $f_{amph,Al}$) were chosen such that Al was

modelled to be slightly less available than iron ($f_{corr,Fe}$ and $F_{oxid,Fe}$) to participate in exothermic reactions due to Al having more persistent passivating layers. It should be noted that this model neglects the effects of time, particle size, pH, and chlorine (Cl) content. While it is difficult to model the exact conditions found in a landfill environment, this analysis provides insight into the relative Heat Generation Potential for ashes based on detailed characterization efforts from facilities with different metal recycling, APCs, and combustion techniques.

Table 2: Summary of Reactions Modelled Using Crystal Ball

Rxn of Interest	**Rxn**	**ΔH_{rxn}**
Ca Hydration	$CaO + H_2O \rightarrow Ca(OH_2)$	-1,629 kJ/kg Ca
Ca Carbonation	$Ca(OH_2) + CO_2 \rightarrow CaCO_3 + H_2O$	-2,866 kJ/kg Ca
Mg Hydration	$MgO + H_2O \rightarrow Mg(OH_2)$	-1,547 kJ/kg Mg
Mg Carbonation	$Mg(OH_2) + CO_2 \rightarrow MgCO_3 + H_2O$	-3,335 kJ/kg Mg
K Hydration	$K_2O + H_2O \rightarrow 2KOH$	-2,618 kJ/kg K
K Carbonation	$2KOH + CO_2 \rightarrow K_2CO_3 + H_2O$	-2,445 kJ/ kg K
Na Hydration	$Na_2O + H_2O \rightarrow 2NaOH$	-3,348 kJ/kg Na
Na Carbonation	$2NaOH + CO_2 \rightarrow Na_2CO_3 + H_2O$	-3,674 kJ/kg Na
Al Corrosion	$Al + 3H_2O \rightarrow Al(OH)_3 + 3/2H_2$	-15,922 kJ/kg Al
Al Oxidation	$2Al + 3/2O_2 \rightarrow Al_2O_3$	-31,058 kJ/kg Al
Al Amphoteric Rxn	$Al + OH^- + 3H_2O \rightarrow Al(OH)_4 + 3/2H_2$	-31,273 kJ/kg Al
Fe Corrosion	$Fe + CO_2 + H_2O \rightarrow FeCO_3 + H_2$	-1,268 kJ/kg Fe
Fe Oxidation	$2Fe + 3/2O_2 \rightarrow Fe_2O_3$	-14,755 kJ/kg Fe

Table 3: Summary of Fractions Used During Crystal Ball Modelling

Fraction Available	Baseline Assumed Value	Assumed Statistical Distribution	Basis for Assumed Value and Statistical Distribution
f_{hyd}	0.7	Normal	• Extent of ash hydration after disposal (some ash hydrated prior to disposal); normal distribution because it is expected that this fraction is symmetric about the mean value of 0.7
f_{carb}	0.85	Normal	• Extent of ash carbonation after disposal; the hydration of oxides is a prerequisite for carbonation based on reactions in Table 2, thus f_{carb} is related to f_{hyd}
$f_{corr,Al}$ $f_{oxid,Al}$ $f_{amph,Al}$	0.25	Exponential Decay	• Al is a more stable oxide (Al_2O_3) than Fe (Fe_2O_3), hence it was modelled with a slightly lower Baseline Assumed Value; exponential decay distribution used because this fraction is expected to be skewed towards 0 when randomized
$f_{corr,Fe}$ $f_{oxid,Fe}$	0.35	Exponential Decay	• Fe oxides (primarily Fe_2O_3) are relatively unstable and may be reduced to Fe for subsequent reactions

A Monte Carlo analysis was conducted for two general purposes: to determine an average Relative Heat Potential for a given material class (i.e. to compare CCAs vs MSWIAs), and to conduct a parametric study to understand the influence of each reaction type on Heat Generation Potential. For the parametric study, a constant fraction input value was varied from 0 to 1 while Crystal Ball varied all other fractions as previously defined and the heat generated was plotted as a function of the fraction value. The goal of this analysis was to identify which reaction type most influenced ash Relative Heat Potential when co-disposed of in a landfill with unburned waste.

CHAPTER 4 RESULTS AND DISCUSSION

4.1 Characterization Efforts

As discussed previously, the goal of this research was to conduct a thorough characterization of freshly-received MSWIAs and CCAs from facilities throughout the U.S., with the goal of identifying key phases or reactions which may be responsible for the development or sustainment of ETLFs. A simple model was formulated to calculate heat generation using ash compositions and published exothermic reactions to gain an understanding of the heat-generating potential for MSWIAs and CCAs. Because of the large number of samples in this study, only example results will be discussed in this section (particularly for XRD and XEDS analyses) while data for the remaining samples can be found in the appropriate appendices at the end of this document. All characterization and modeling efforts were conducted at UCF, and results are presented below.

4.1.1 pH and Particle Size Analysis (PSA)

A summary of pH values for all 16 ashes analyzed can be found in Figure 7. All ashes were highly alkaline (pH>10) except for one sample (CCA-6), which, because of prolonged weathering effects or because of the presence of WWTP biosolids in the sample, appears to be an outlier. This sample was aged outside for at least 15 years, but the ratio of CCA:WWTP biosolids is unknown. In general, MSWIAs tended to be slightly more alkaline than CCAs, likely due to differences in chlorine concentrations and the forms of calcium-bearing phases present. Regardless of these differences, all ashes exhibited values (pH≥8) which may promote the highly exothermic amphoteric reaction of aluminum (Calder and Stark, 2010). Amphoteric refers to the

fact that aluminum can act as both an acid and a base, but for this particular reaction aluminum serves as an acid which reacts with hydroxide according to the equation in Table 2

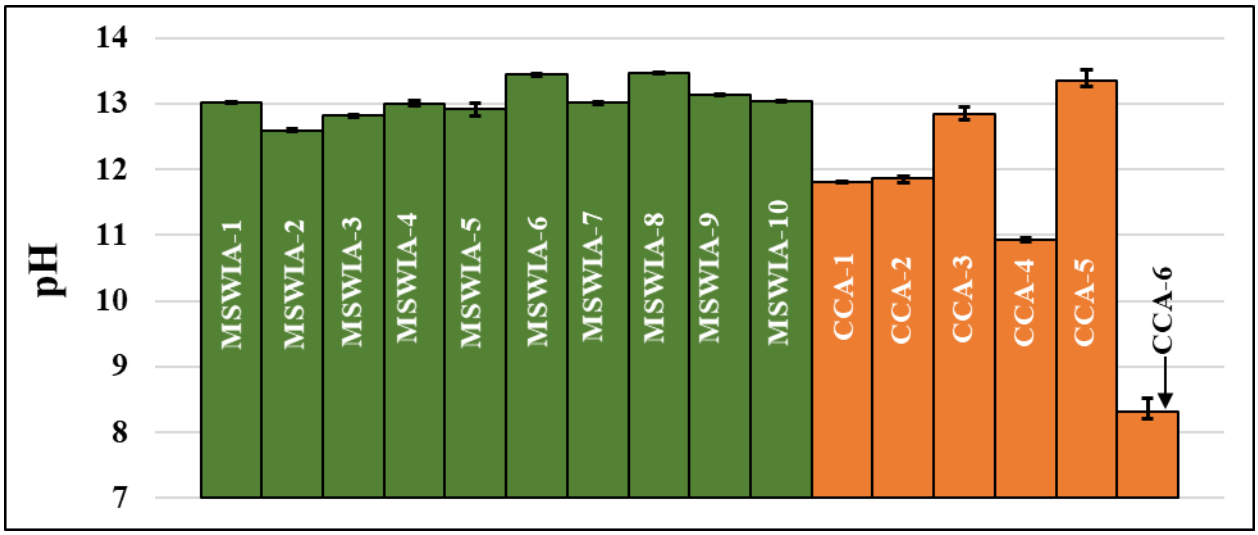

Figure 7: Results of pH Analysis

PSA was conducted for eleven (six MSWIAs and five CCAs) out of the sixteen ash samples following initial sieving and milling efforts. Unfortunately, the particle size analyzer required maintenance which prohibited the timely analysis of the remaining samples. Average MSWIA particle diameters for samples ranged from 0.318 to 1.20 mm, compared to 0.016-0.26 mm for CCA samples. Because the MSWIA samples (Table 5) analyzed were combined bottom and fly ashes, results should not be directly compared with the coal fly ashes presented in Table 4 (CCA- 1,3,4, and 5). However, CCA-2 is a coal bottom ash sample with the largest average particle diameter (260 μm) of all the CCAs analyzed. The mean diameter for CCA-2 was still roughly 20% smaller than the finest combined MSWIA sample analyzed (mean of 318 μm). As

discussed in Chapter 2, there have been similar findings by other researchers which verify that CCAs tend to be generated with finer particle sizes than MSWIAs.

Table 4: PSA Results for CCAs

Parameter	CCA-1	CCA-2	CCA-3	CCA-4	CCA-5
Mean (μm)	30.6	260	16.1	17.2	35.7
Median (μm)	10.6	155	4.10	7.90	18.7
S.D. (μm)	48.9	271	34.5	30.8	39.9
d10 (μm)	1.00	39.1	0.70	1.00	1.50
d90 (μm)	87.2	671	41.7	37.7	96.7

Note: **S.D.** – standard deviation; **d10** and **d90** – the diameters for which 10% and 90% of the total distribution are finer, respectively.

Table 5: PSA Results for MSWIAs

Parameter	MSWIA 1	MSWIA 2	MSWIA 3	MSWIA 4	MSWIA 5	MSWIA 10
Mean (μm)	318	400	722	827	1200	621
Median (μm)	268	310	518	675	1400	467
S.D. (μm)	281	360	635	654	659	522
d10 (μm)	11.9	28.9	26.8	23.0	142	70.1
d90 (μm)	714	995	1740	1790	1920	1460

Note: **S.D.** – standard deviation; **d10** and **d90** – the diameters for which 10% and 90% of the total distribution are finer, respectively

The specific particle size distributions can be found in Figures 8 and 9, while cumulative particle distributions are presented in Figures 10 and 11. CCAs tended to contain particles with sizes concentrated between 0 and 40 μm, except for CCA-2 and CCA-5. There were no obvious trends in particle size among coal fly ashes gathered from different APCs (baghouse filter vs.

electrostatic precipitator) or of different classification types (Class C vs Class F), but there is some indication that coal power plants which use circulating fluidized bed (CFB) combustion (CCA-5) may produce fly ashes that are slightly larger in size and distribution than particles produced from pulverized coal combustion (CCAs 1-4).

An independent two-tailed t-test with a confidence level of 95% was performed to identify whether there was a statistically significant difference in particle size between: CCA bottom ash (CCA-2) and fly ashes (CCAs-1, 3, 4, and 5), CCA bottom ash (CCA-2) and combined MSWIAs (all six samples analyzed), and CCA fly ashes (CCAs-1, 3, 4, and 5) and combined MSWIAs. Findings show that coal bottom ash (M=260 μm, SD=271 μm) was statistically larger in particle size than coal fly ashes (M=24.9 μm, SD=38.5 μm); $t(178)=8.17$, $p<.00001$. Similar findings were revealed, $t(178)=6.81$, $p<.00001$, when comparing coal bottom ash (M=260 μm, SD=271 μm) to combined MSWIA samples (M=680 μm, SD=519 μm), and coal fly ash (M=24.9 μm, SD=38.5 μm) to combined MSWIAs (M=680 μm, SD=519 μm); $t(178)=12.0$, $p<.00001$.

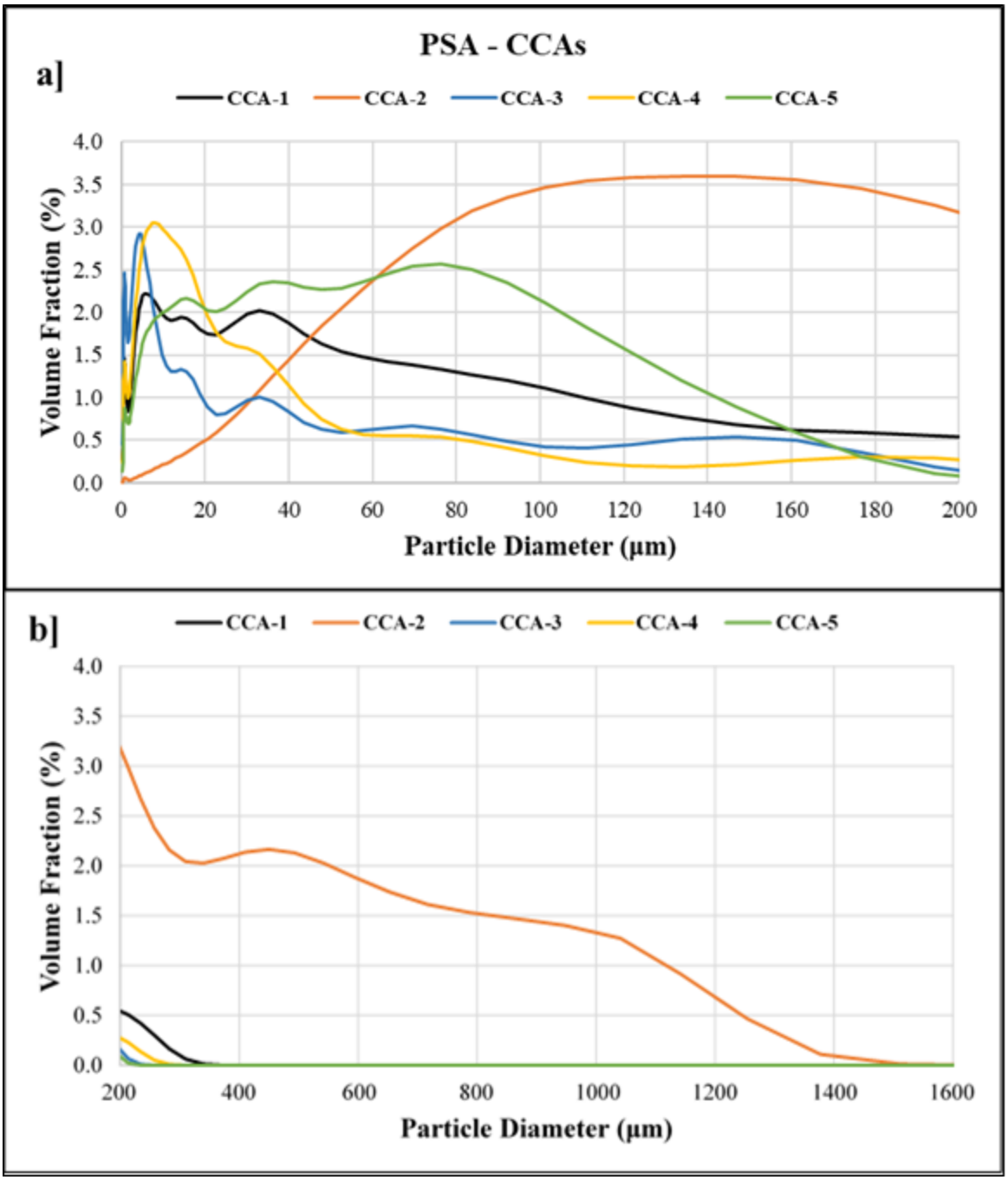

Figure 8: Particle Size Distribution for CCAs **a]** Ranging from 0-200 µm and **b]** Ranging from 200-1600 µm.

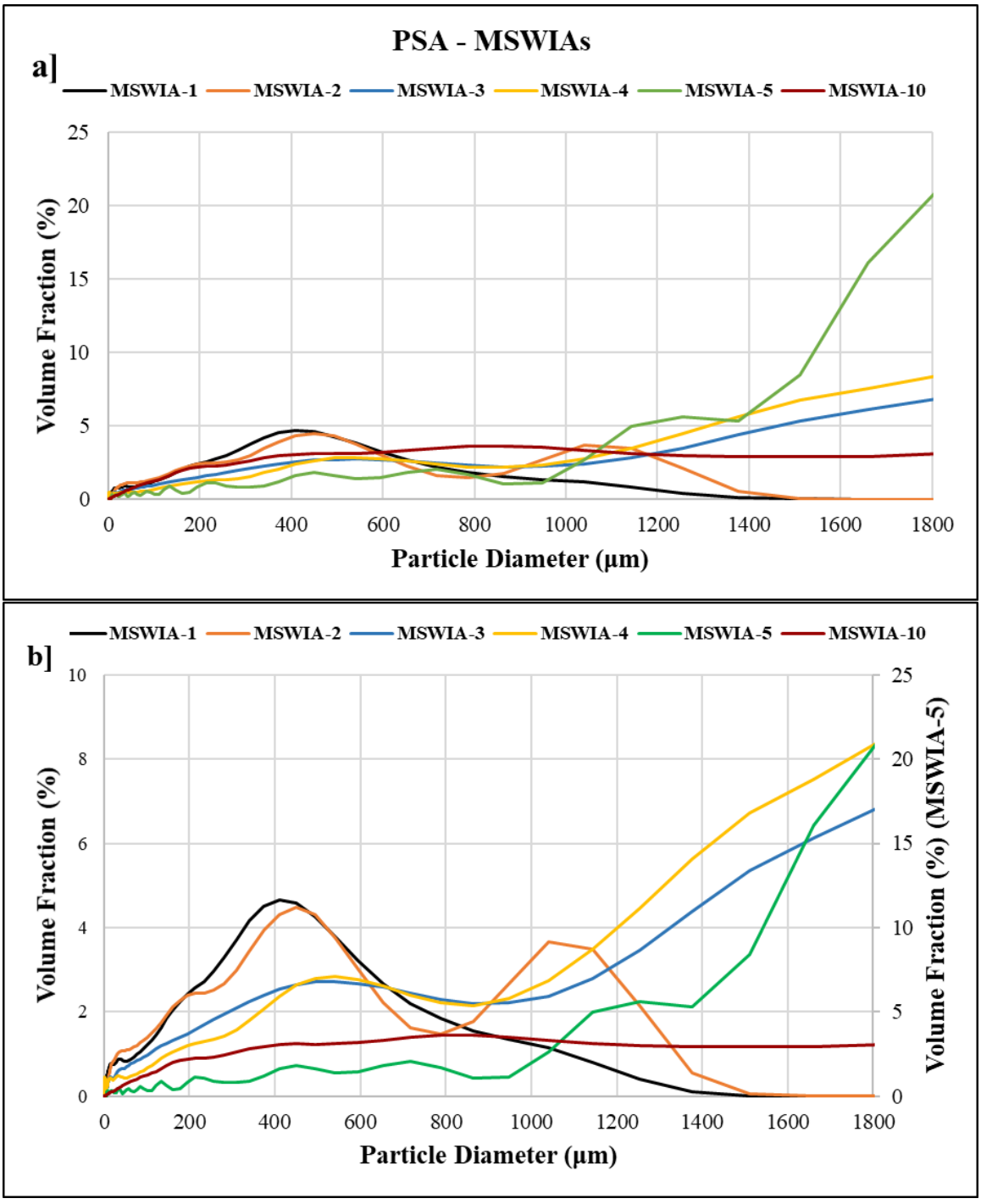

Figure 9: Particle Size Distribution for MSWIAs. **a]** Comparison Between All MSWIA Samples Analyzed with Single Axis and **b]** Comparison with Secondary Axis for Sample MSWIA-5.

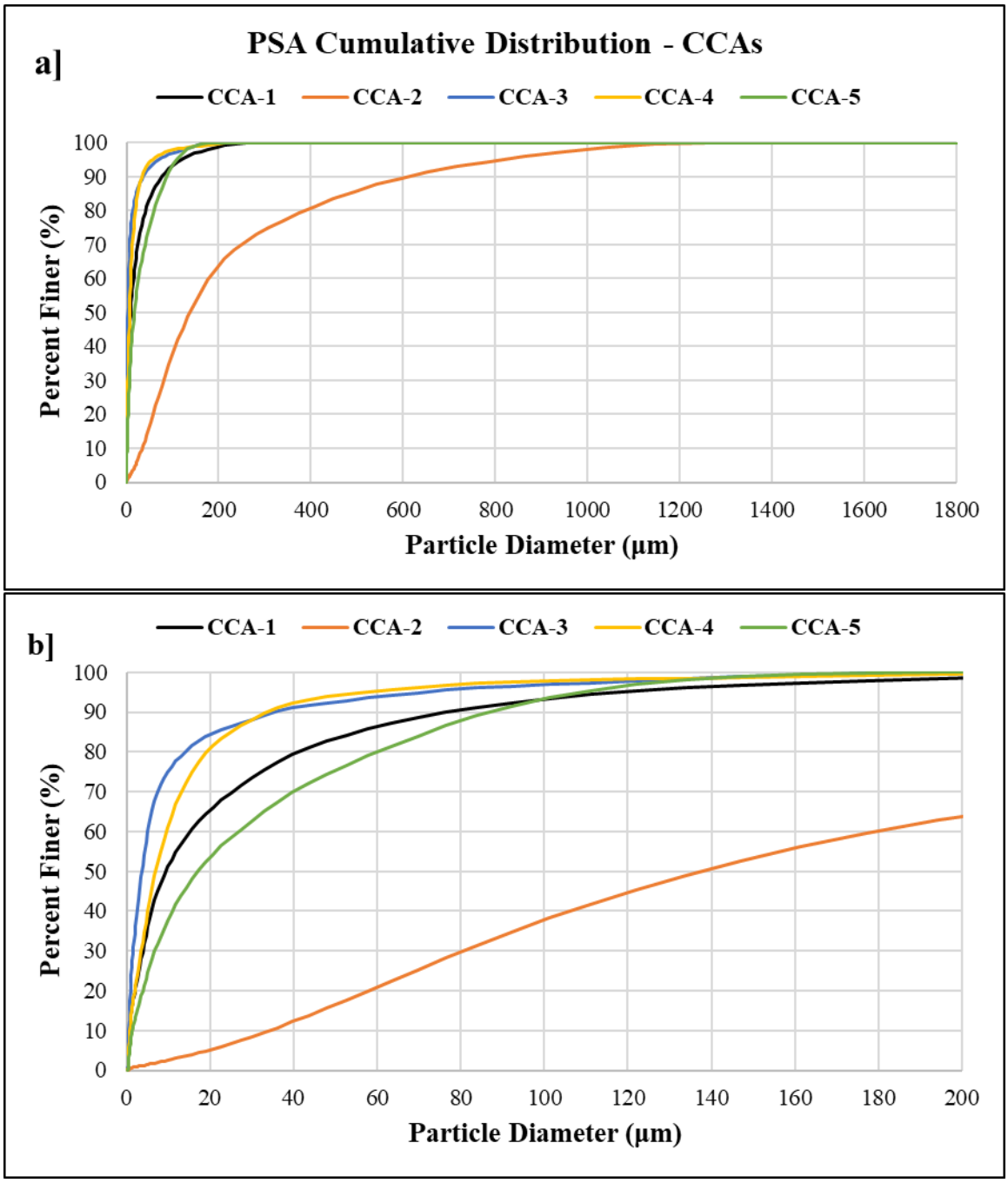

Figure 10: Cumulative Particle Size Distribution for CCAs for **a]** 0-1800 µm Range and **b]** 0-200 µm Range

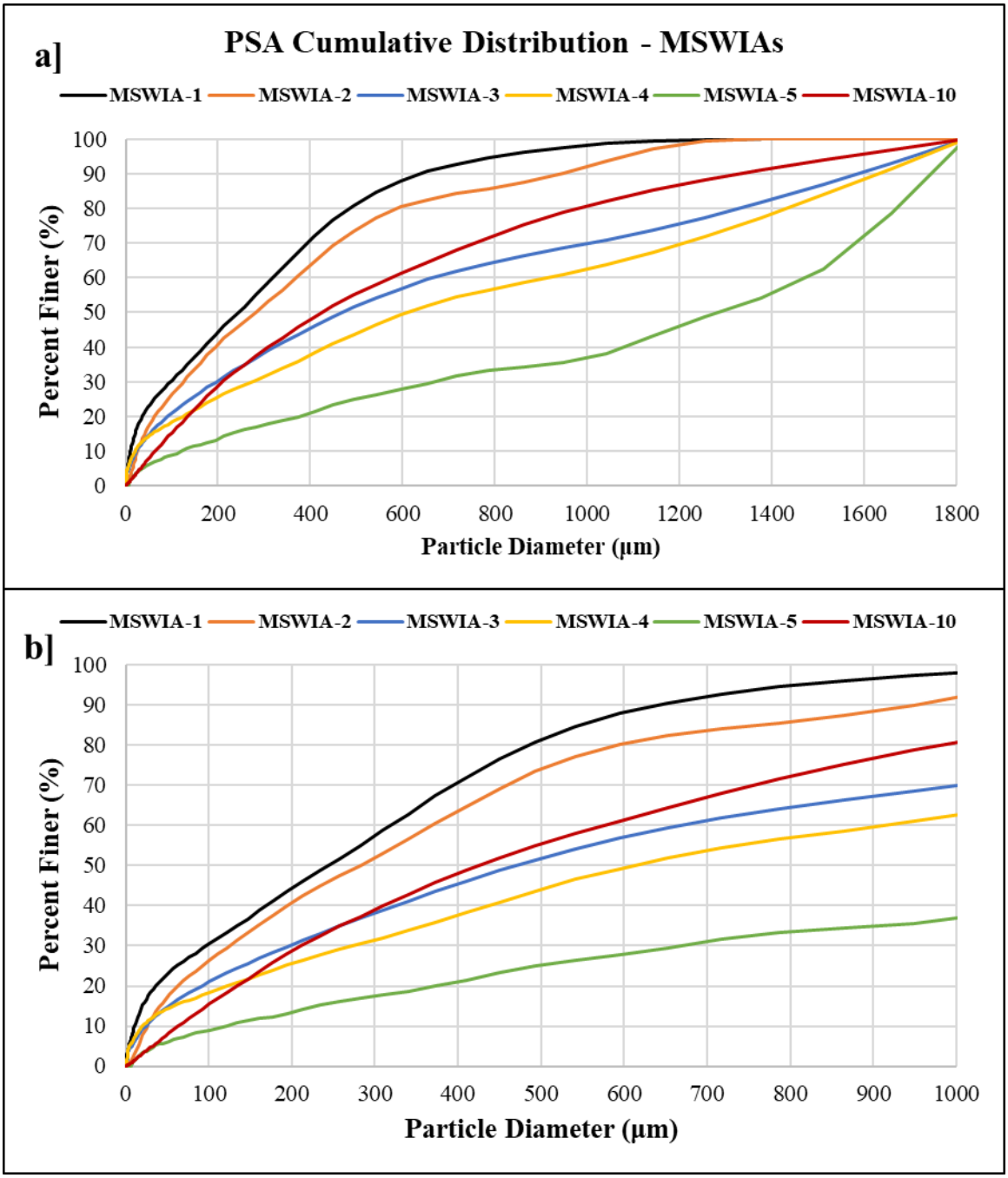

Figure 11: Cumulative Particle Size Distribution for MSWIAs for **a]** 0-1800 µm Range and **b]** 0-1000 µm Range

Coal fly ashes were primarily finer than 100 μm while the bottom ash sample (CCA-2) was comprised mainly of particles finer than 1000 μm (Figure 10b). The particle size distribution for MSWIAs varied across a greater range of particle diameters compared to the CCAs analyzed due to the heterogeneity of MSWIAs. Another interesting finding is that the sample with high lime rate addition (MSWIA-5) exhibited a greater fraction of particles with larger diameters (>1400 μm) than the other MSWIAs, although the exact reason for this is unknown. The only difference between Figures 9a and 9b is that MSWIA-5 was plotted on a secondary axis so that the trend of the remaining samples could be more easily visualized. Results from this analysis show that there may be some influence of non-ferrous metal (Al) recovery on particle size for MSWIAs. MSWIAs-1 and 2 originated from facilities with no appreciable aluminum recovery while MSWIAs-3 and 4 were from facilities which did practice aluminum recovery. MSWIAs-1 and 2 contained particles with finer average diameters than those of MSWIAs-3 and 4, and the size distribution of MSWIAs-1 and 2 exhibits similar trends in the range of 0-800 μm while the size distributions for MSWIAs-3 and 4 also appear similar but across a broader range of 0-1800 μm. A recent project investigated the distribution of ferrous and non-ferrous metals in various size fractions of aged and raw MSWI bottom ash from a German waste incineration facility (Vateva and Laner, 2020). The results of this study highlight the trend that Fe and other heavy metals like Ni and Cr tend to concentrate in the coarse fraction (>31.5 mm) of bottom ash, while Al and Cu concentrations increase with decreasing particle size. If Al is recovered at some point during the incineration process, then there must be a lesser amount of Al present in the finer fractions of combined MSWIA which requires disposal at a landfill compared to ash generated from facilities which do not practice non-ferrous metal recovery. This may have significance

regarding exothermic reactivity when these ashes are co-disposed with unburned MSW in landfills, as a finer ash with greater surface area and metal content can be expected to pose a greater risk for heat generation and ETLF development.

4.1.2 Thermal Gravimetric Analysis (TGA)

As mentioned in Chapter 2, researchers have identified key temperature ranges associated with the thermal degradation of select compounds, of which carbonates and hydroxides are of particular importance to this project because of their potential involvement in exothermic reactions when deposited in landfills. For this study, the mass was recorded prior to, during, and following, the TGA experiment to determine the total weight loss for each ash analyzed. TGA curves for all ashes can be found in Figures 10 and 11, while the total weight loss can be found in Table 6.

Table 6: TGA Results – Total Weight Loss from 25-900°C

Sample ID	Total Weight Loss (%)
CCA-1	0.5
CCA-2	0.1
CCA-3	15.3
CCA-4	4.7
CCA-5	1.6
CCA-6	30.8
MSWIA-1	12.1
MSWIA-2	14.0
MSWIA-3	12.9
MSWIA-4	12.5
MSWIA-5	11.8
MSWIA-6	9.9
MSWIA-7	22.8
MSWIA-8	8.8
MSWIA-9	24.9
MSWIA-10	13.5

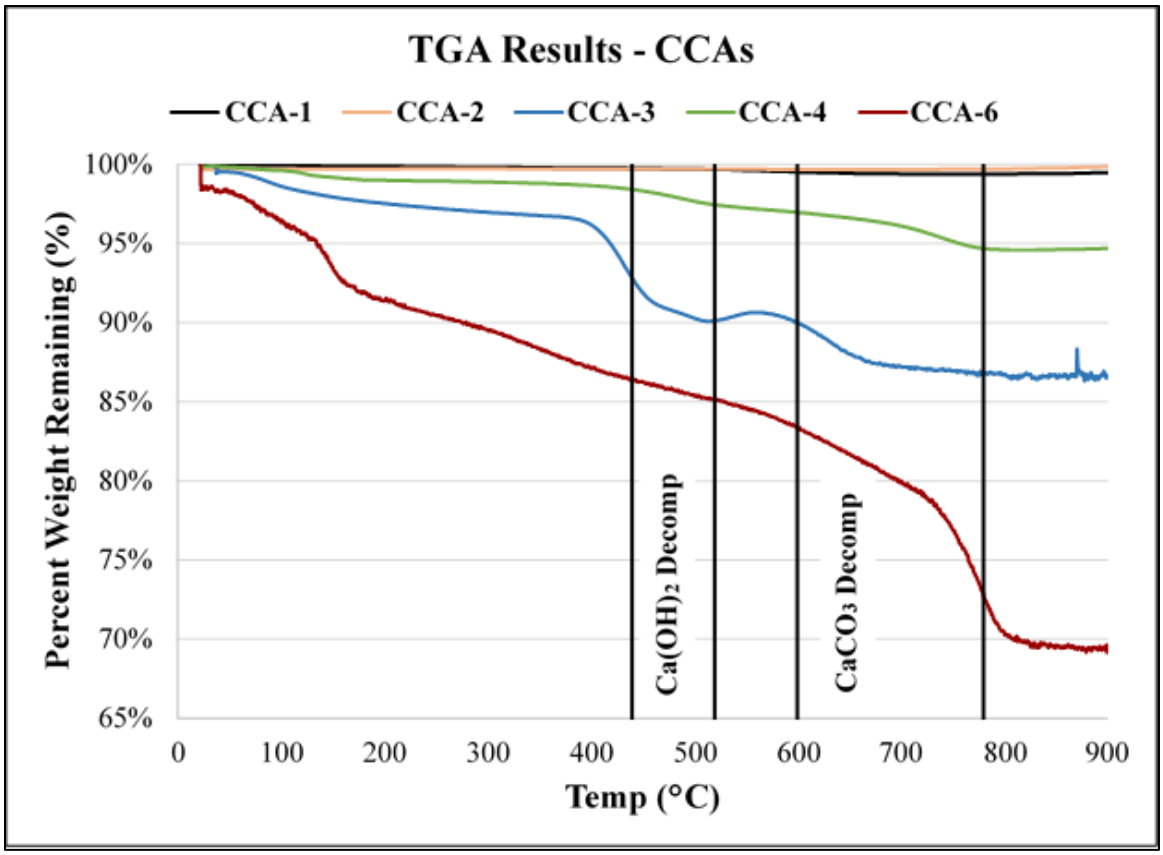

Figure 12: TGA Summary for CCAs

Note: CCA-5 is not shown because of instrumental error, likely due to vibrations which disturbed the TGA. However, initial and final masses were still recorded to calculate the Total Weight Loss (%) value presented in Table 6.

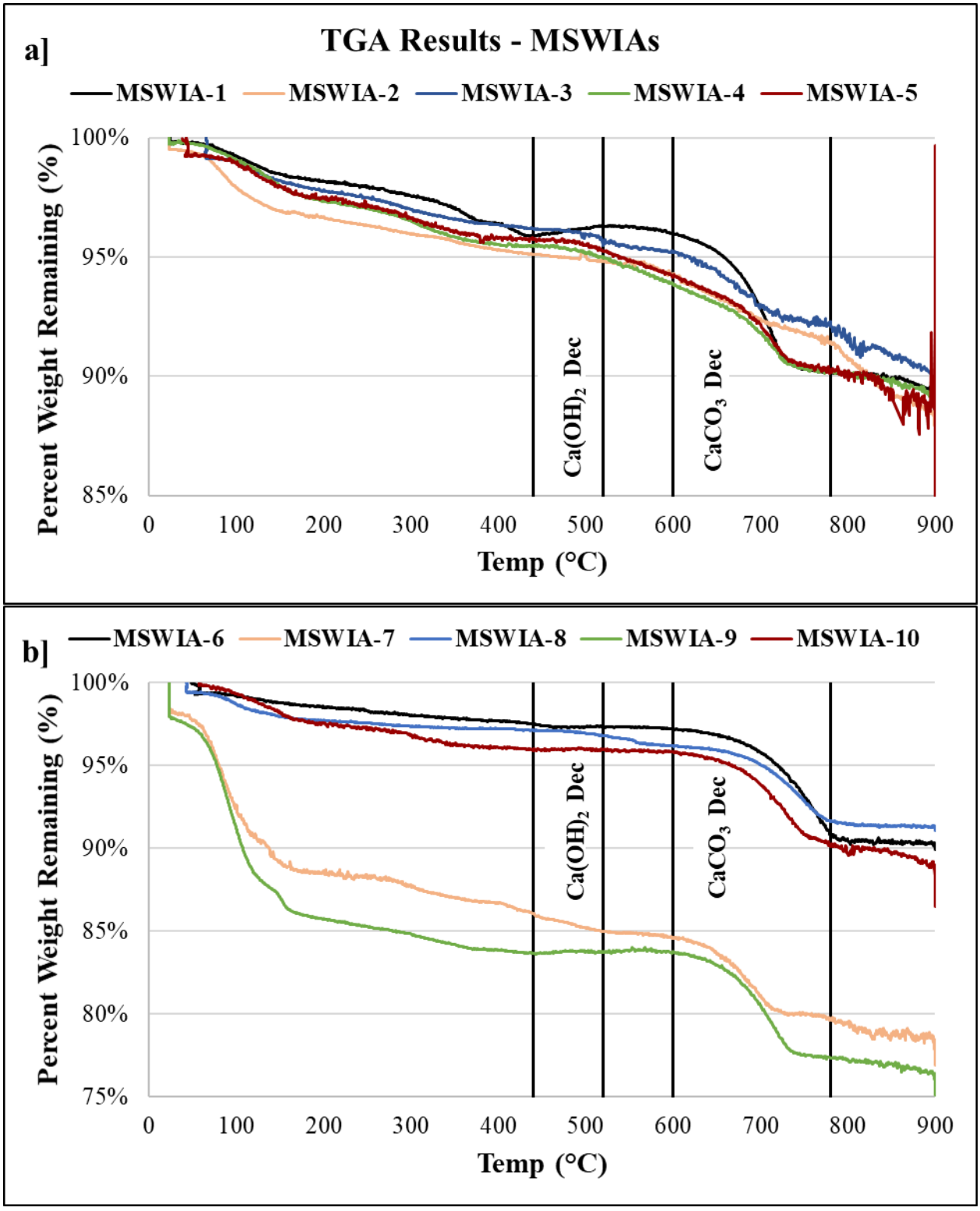

Figure 13: TGA Results for **a]** MSWIAs-1 to 5 and **b]** MSWIAs-6 to 10.

TGA results show that MSWIAs tended to be more susceptible to thermal degradation than CCAs, as the Total Weight Loss (%) data for MSWIAs were greater than most CCA samples, except for the WWTP biosolids + coal ash (CCA-6) and Class C fly ash with sodium carbonate and activated carbon addition (CCA-3). To verify this finding, a two-tailed independent t-test was performed to compare the weight loss between: MSWIAs vs CCAs (excluding CCA-6 because of the influence of WWTP biosolids), MSWIA fly ash (MSWIAs-7 and 9) vs bottom ash (MSWIAs-6 and 8) samples, and CCA fly ash (CCAs-1, 3, 4, and 5) vs CCA bottom ash (CCA-2) samples. Results of this statistical analysis prove that MSWIAs ($M=14.3\%$, $SD=5.0\%$) experienced a significantly greater weight loss between 25 to 900°C compared to CCAs ($M=4.5\%$, $SD=5.7\%$); $t(13)=3.43$, $p=.004$. MSWIA fly ashes ($M=23.8\%$, $SD=1.1\%$) also significantly demonstrated a greater weight loss across this temperature range compared to MSWIA bottom ashes ($M=9.3\%$, $SD=0.57\%$); $t(2)=17.0$, $p=.003$. Lastly, the same weight loss trend was observed for CCA fly ashes ($M=5.5\%$, $SD=0.41\%$) compared to CCA bottom ash ($M=0.1\%$; $SD=0.0\%$); $t(3)=26.2$, $p=.0001$.

CCA-6 exhibited the greatest weight loss of all samples analyzed across the entire temperature range, likely due to the release of physically absorbed water (25-200°C), chemically bound water (300-450°C), and degradation of volatile and organic matter associated with WWTP biosolids (200-400°C) that are not found in pure ash samples (Felipe-Sesé et al., 2011; Narode et al., 2021). CCA-6 also showed a large weight loss associated with the thermal degradation of carbonates (600-780°C), likely due to the prolonged aging of this sample outdoors which allowed for extensive carbonation. Another finding of this experiment was that, for both MSWIAs and CCAs, fly ashes tended to be more susceptible to thermal degradation than bottom

ashes. This is evident by the very low weight loss for CCA-2, the only coal bottom ash sample. MSWIAs-6 and 8 (bottom ashes from separate WTE facilities) also showed a much lower weight loss (9-10% vs. 23-25%) compared to fly ashes gathered from the same facilities (MSWIAs-7 and 9). All six combined MSWIAs exhibited weight losses in a tight range of 12 to 14%, primarily due to the decomposition of calcite ($CaCO_3$) and similar carbonates, as well as chemically bound water.

Figure 13 highlights the fact that MSWI fly ashes contain a greater amount of adsorbed water (~10% by weight) than bottom or combined ashes as evident by the weight loss that occurred between 25-100°C. This may be attributed to the finer particle size of fly ashes, but it is unknown why this trend is not observed for CCAs. Although no quantification was attempted using TGA, Figures 12 and 13 show that most ash samples exhibited little to no degradation of hydroxides in the temperature range of 440 to 520°C, but most samples contained an appreciable amount of carbonates which degrade between 600 and 780°C. This may imply that ashes which are hydrated immediately after their generation – during quenching or external environmental factors – are readily carbonated prior to their disposal in a landfilled environment, meaning that carbonation and hydration reactions may not be the primary mechanisms for heat generation following their disposal in landfills. Samples CCA-3 and MSWIA-1 also showed instances of weight gain between 450 and 600°C, which may be indicative of the exothermic oxidation of a metal which we were unable to identify from literature.

4.1.3 X-Ray Diffraction (XRD) and X-Ray Fluorescence (XRF)

Concentrations determined via XRF were averaged across triplicate samples and results are presented in Tables 7 and 8 – some elements which were detected in trace amounts (units of ppm) were excluded from this table. XRF results were also used to develop ternary phase diagrams for two systems (Ca-Al-Si and Ca-Fe-Si) relevant to incinerator ashes to gain an understanding of the distribution of these elements across different ash types (Figure 14). For a given ternary system, concentrations determined via XRF for each of the three elements were first normalized against one another and then plotted in Excel to gain a visual understanding of each ash's composition. The ternary diagrams produced for both MSWIAs and CCAs are comparable to those reported in literature and ash compositions, particularly for MSWI fly ashes with their reduced aluminum contents, may be similar to that of ordinary Portland cement (OPC) because of high calcium and silicon contents with minor amounts of aluminum (Figure 14a) (Phua et al., 2019). This highlights their potential for reuse in building applications, although some pretreatment may be required to reduce chlorine and aluminum contents (Clavier et al., 2021). Figure 14a also shows that fly ashes contain greater calcium contents than combined and bottom ash fractions due to the use of lime for air pollution treatment. Depending on the phase that calcium is present in, high concentrations may be problematic due to exothermic hydration, carbonation, and precipitation reactions that are likely to occur when ash is co-disposed with raw MSW in landfills. However, these fly ashes (particularly MSWIAs) contain less metallic iron and aluminum than their respective combined and bottom ash fractions. Hence, these combined bottom and fly ashes are likely to be enriched in calcium and chlorine from fly ash and air pollution control residues, while also rich in aluminum and iron from bottom ash fractions.

Table 7: XRF Results for MSWIAs

Element	Sample ID									
	MSWIA-1	**MSWIA-2**	**MSWIA-3**	**MSWIA-4**	**MSWIA-5**	**MSWIA-6**	**MSWIA-7**	**MSWIA-8**	**MSWIA-9**	**MSWIA-10**
Ca	50	38	40	43	46	60	62	53	56	56
Cl	13	27	23	14	15	2.9	23	2.2	22	21
Si	13	11	11	15	12	17	2.5	19	2.4	5.7
Fe	8.7	8.6	10	8.6	9.1	4.2	1.5	13	1.2	2.6
Al	3.8	4.0	3.6	4.3	4.8	4.4	1.6	1.6	0.9	1.8
S	2.4	3.1	3.5	4.3	4.7	2.7	3.1	4.7	6.3	4.7
K	2.3	2.9	3.0	3.3	2.8	1.4	3.2	2.6	5.4	2.8
Zn	1.9	1.9	2.3	1.8	1.9	0.9	1.3	1.2	3.9	2.8

Note: Concentrations expressed as atomic %.

Table 8: XRF Results for CCAs

Element	Sample ID					
	CCA-1	**CCA-2**	**CCA-3**	**CCA-4**	**CCA-5**	**CCA-6**
Ca	40	40	65	33	44	54
Cl	0.4	0.4	14	0.7	0.5	0.6
Si	23	22	4.2	17	22	13
Fe	13	15	4.9	11	9.0	9.9
Al	13	13	3.1	10	11	8.2
S	1.7	1.8	7.7	21	7.3	7.7
K	1.2	1.1	0.7	1.2	1.8	1.9

Note: **ND** – Not Detected; concentrations expressed as atomic %.

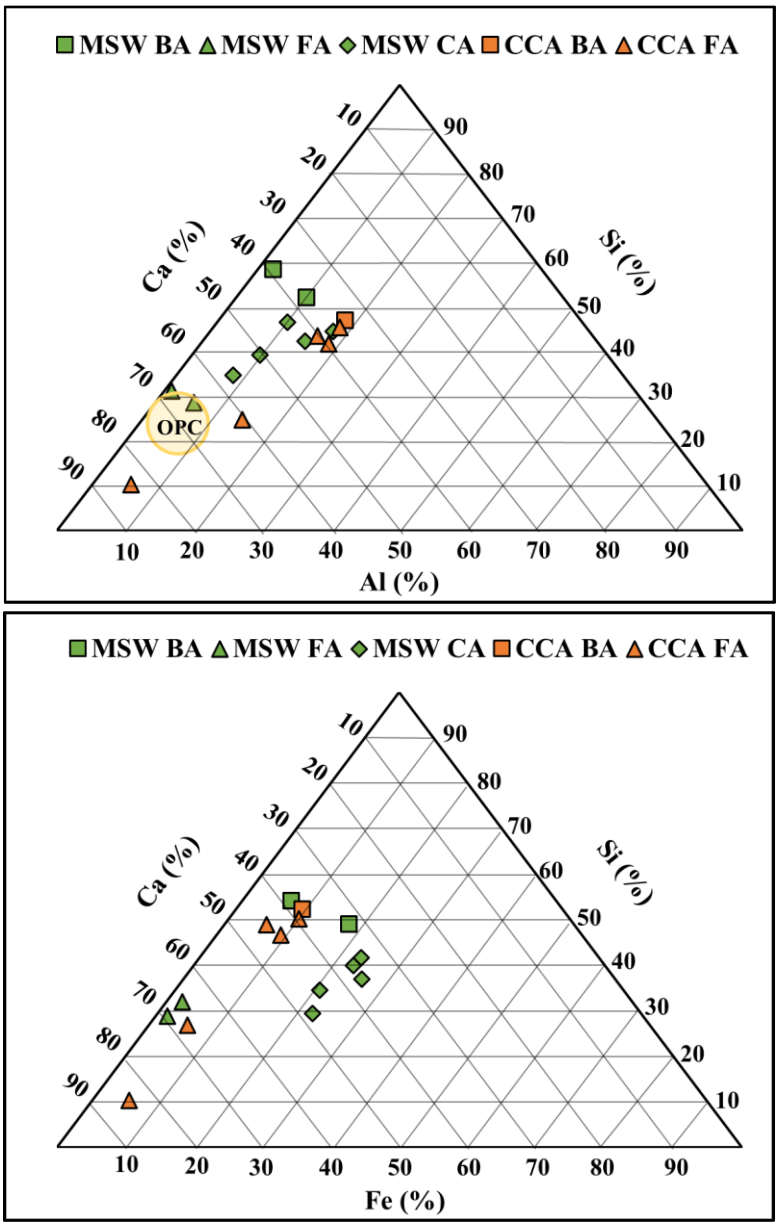

Figure 14: Ternary Phase Diagram Comparison for **a]** Ca-Al-Si System and **b]** Ca-Fe-Si System.

Note: The ordinary Portland cement (OPC) region in Figure 14a was derived from the work of Phua et al. (2019).

From our results, the primary constituents of MSWIAs are Ca, Cl, Si, Fe and Al while the main constituents of CCAs are Ca, Si, Fe and Al. Figure 14 highlights the fact that CCAs contained greater fractions of Al than MSWIAs, while the opposite is true for the Fe observed in many MSWIA samples. These differences in metal content may necessitate future research regarding unique treatment approaches for CCAs vs MSWIAs as it relates to mitigating the formation of ELTFs when these ashes are ultimately disposed. XRF analysis also showed a considerable difference in Cl concentrations between CCAs and MSWIAs, and previous research has highlighted the negative effects of chloride content on ash usability in building materials and enhanced metal corrosion (Joseph et al., 2018; Dontriros et al., 2020). The abundance of chlorine found in MSWIAs is likely due to the incineration of large volumes of plastics and food wastes found in raw MSW. During incineration, these chlorides volatilize and condense on particulate matter in the flue gas which is subsequently removed by APCs such as acid-gas scrubbers or baghouse filters. Hence, chlorine is found predominantly in fly ash and the finer fraction of bottom ash for MSWIAs which, in the U.S., are typically combined and disposed in landfills (Joseph et al., 2018). Crystalline forms of chlorine may dissolve after some time in the presence of water; aquatic chloride promotes the exothermic corrosion of metals.

A rough comparison between XRD patterns for CCAs and MSWIAs can be found in Figures 15 and 16, and detailed phase identification for each sample can be found in Appendix B. In general, XRD patterns revealed a greater amorphous content for CCAs than MSWIAs as evident by the fewer number of well-defined peaks and presence of an amorphous ‘hump’ in all CCA XRD patterns. These amorphous fractions have been noted to contain materials such as aluminosilicates that are more reactive in alkaline environments than the crystalline fraction

(Chancey, 2008). MSWIA XRD patterns show many wide peaks, often with accompanying ‘shoulders’, resulting from the presence of multiple phases with diffraction peaks near the same 2θ. The large amorphous content and abundance of shared diffraction peaks in CCAs and MSWIAs make their complete characterization difficult using strictly XRD.

Quartz (SiO_2) is a crystalline phase identified in nearly all ash samples, regardless of whether the ash originated from coal or refuse. While considered relatively inert across short time periods, there may be some exothermic dissolution of silicate materials, especially in alkaline environments (pH > 8), which results in aqueous silica that can further react with ions present (Wei et al., 2011; Crundwell, 2017). Aluminum was detected in many ashes in the form of complex aluminosilicates (like boggsite, laumontite, and hydrocalumite), sometimes as hydrated calcium aluminum oxides and in one case as aluminum oxide (Al_2O_3). Iron, on the other hand, was predominantly identified as iron hydroxide ($Fe(OH)_3$) and magnetite (Fe_3O_4), and on a few occasions as iron silicate ($FeSiO_4$) and hematite (Fe_2O_3). Calcium was found in many ash samples in the form of anhydrite ($CaSO_4$) and associated with aluminosilicates. Calcium was only detected in the forms of portlandite ($Ca(OH)_2$) and calcite ($CaCO_3$) in one sample, respectively. Despite the strong indication of the presence of carbonates via TGA, calcite and other carbonates were not commonly detected via XRD. The readily reactive form of quicklime (CaO) was not detected in any ash sample, thus verifying that ashes undergo hydration and carbonation processes after their generation that convert this highly reactive form into either portlandite ($Ca(OH)_2$), calcite ($CaCO_3$), or some other complex mineral. Chlorine was identified in a few ashes as calcium chloride hydroxide (CaClOH) and found in many ashes in the crystalline forms of sylvite (KCl) and halite (NaCl), both of which may dissolve after time to

contribute chlorine ions into solution that may promote metal corrosion or 'pitting' that may degrade passive layers on ash particles.

Figure 17 shows a comparison of two representative XRD plots following phase identification. For these particular ashes, complex aluminum and iron-bearing minerals were found in MSWIA-10 despite originating from a facility practicing ferrous and non-ferrous metal recovery, while the Ca-rich CCA-3 was found to be comprised of portlandite, anhydrite and calcium chloride hydroxide. Certain mineral phases identified (e.g., portlandite, hydrocalumite and boggsite) may be of concern to landfill operators because of their instability resulting from changes in environmental factors like declining pH, which occurs from natural weathering (carbonation) in landfills and ash monofills (Saffarzadeh et al., 2011). If destabilized, the metals (Al, Ca, and Fe) present in the mineral structure may be released and made available to participate in exothermic reactions.

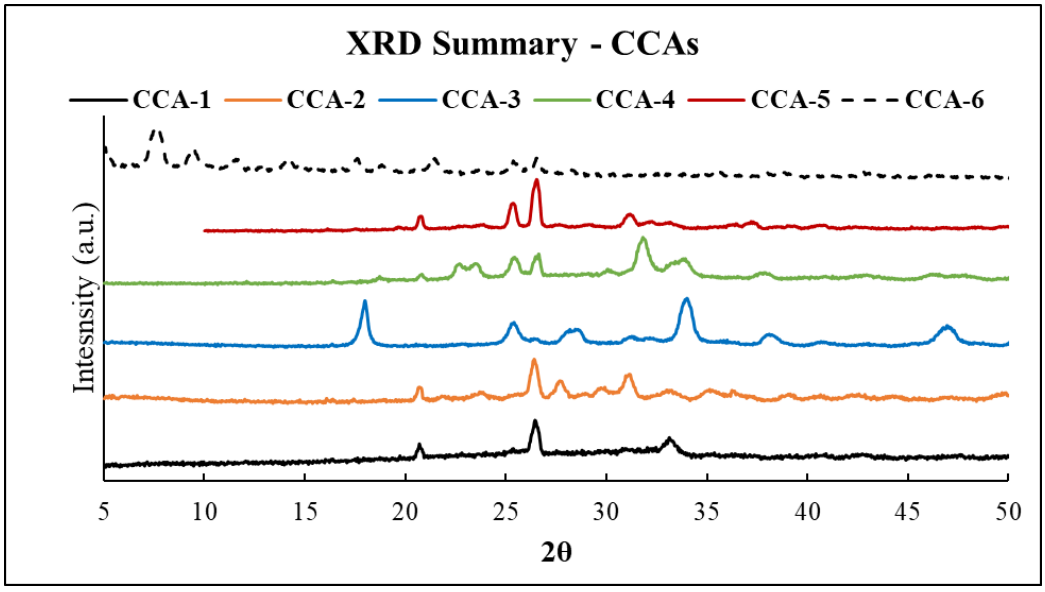

Figure 15: XRD Pattern Comparison for CCAs from 5-50° 2θ.

Note: **a.u.** – Arbitrary Units.

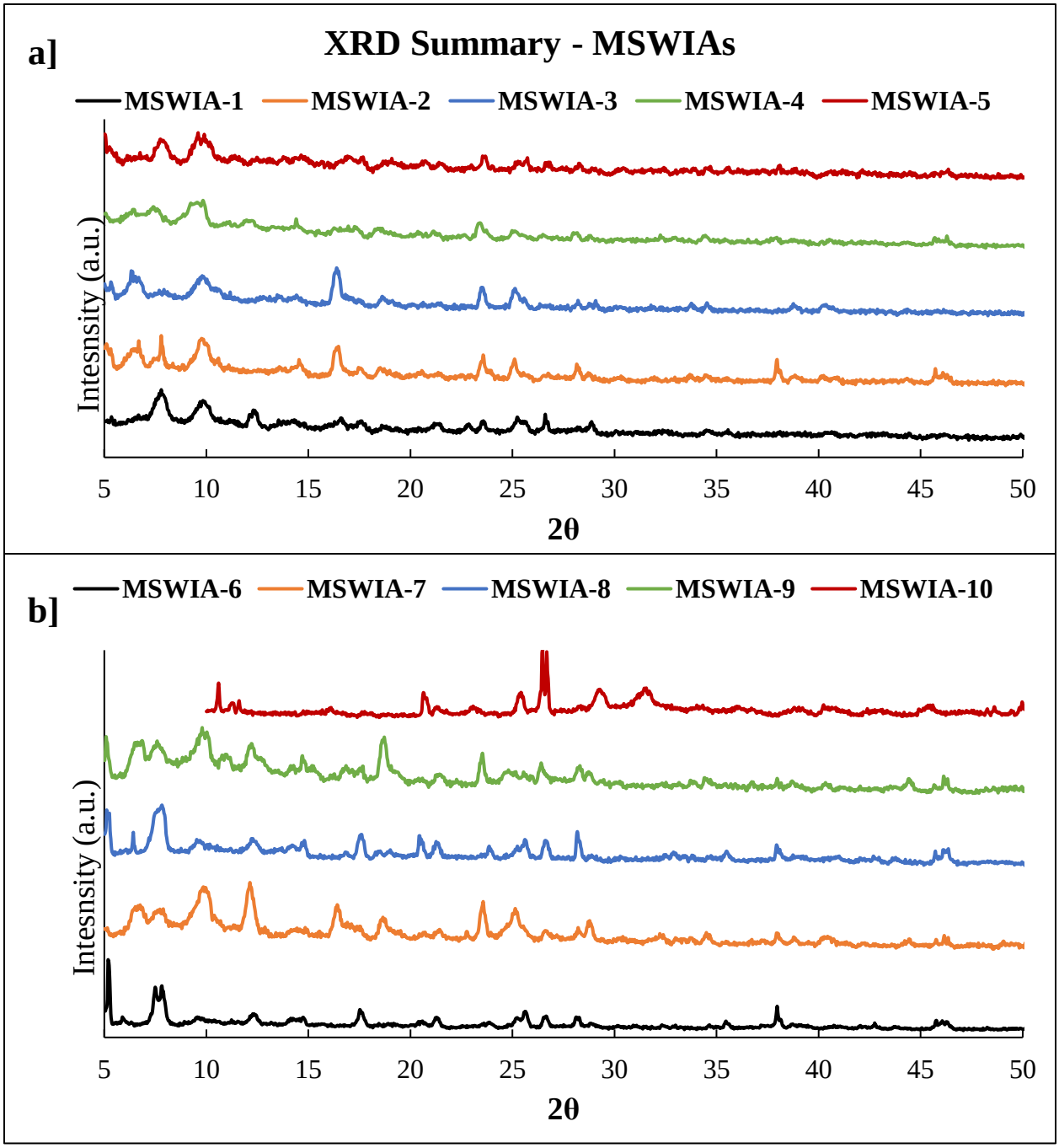

Figure 16: XRD Pattern Comparison from 5-50° 2θ for **a]** MSWIAs- 1 through 5 and **b]** MSWIAs 6 through 10.

Note: **a.u.** – Arbitrary Units.

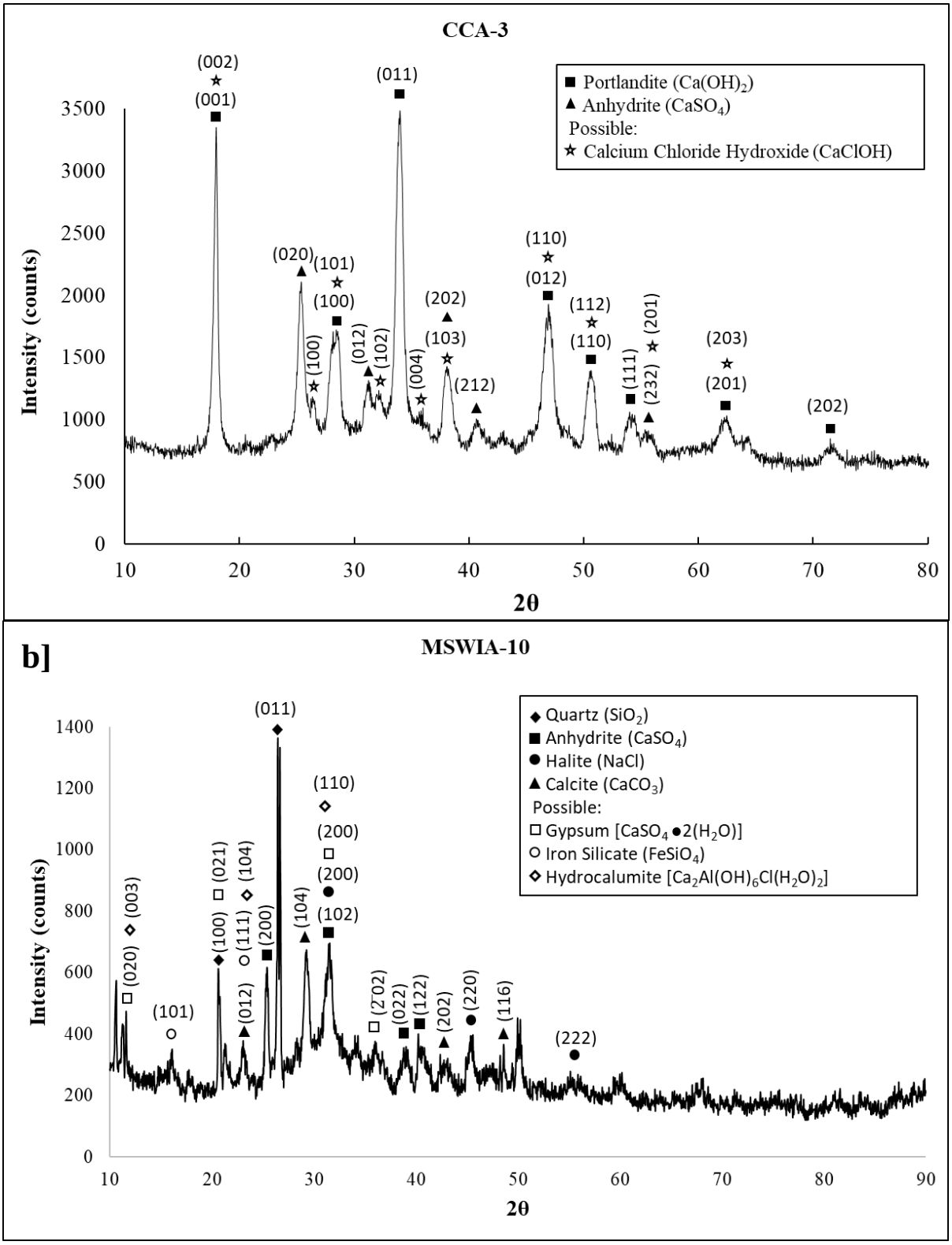

Figure 17: Example of XRD Phase Identification for **a]** CCA-3 and **b]** MSWIA-10

4.1.4 Scanning Electron Microscopy and X-Ray Elemental Dispersive Spectroscopy (SEM/XEDS)

As described in Chapter 3, SEM coupled with XEDS allowed for the detailed characterization of CCAs and MSWIAs after mounting and polishing samples according to typical metallurgical practices. While some samples will be discussed in this chapter for comparison, XEDS data and BSE images for all samples can be found in Appendix A and C. Over the course of this analysis, differences in composition were highlighted by taking representative backscattered electron (BSE) images, which display ash constituents with a higher average atomic weight (or Z number) in a lighter color than those with lower atomic weights. For example, both CCA-1 and MSWIA-7 are fly ashes that contain metallic inclusions (bright particles) based on Figure 18, but the stark differences in size and distribution of these ash materials are also highlighted. At a magnification of 25x and a working distance of 13 mm, it can be seen that coal fly ashes tend to be much finer and circular in shape compared to MSWIAs, likely due to the heterogeneity in size and composition of raw MSW compared to coal feedstocks. It can also be seen that this trend in size is consistent for bottom ashes as CCA-2 contains particles smaller on average than for MSWIA-8, both of which are bottom ash samples. This analysis also proved that bottom ashes in MSWIAs had a larger presence of metallic particles primarily composed of iron with other heavy metal inclusions. Although iron was not as abundant in CCAs compared to MSWIAs, the opposite is true for aluminum based on XEDS analysis. Figure 18 also highlights the fact that coal bottom ash (CCA-2) tended to exhibit materials with more consistent average atomic numbers than MSWI bottom ash (MSWIA-8) because of the greater contrast in color for Figures 18d vs 18b. .

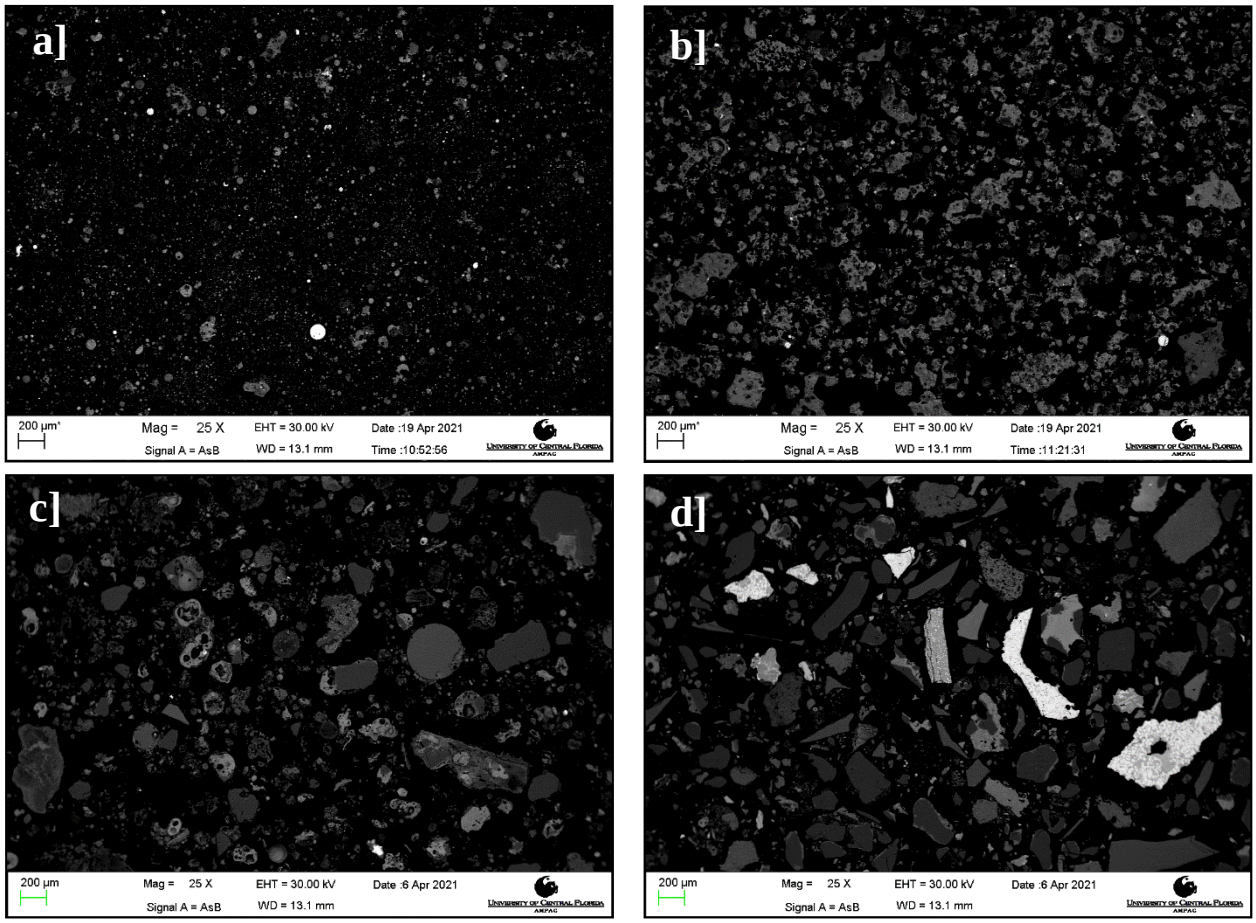

Figure 18: Representative BSE Image for **a]** CCA-1, **b]** CCA-2, **c]** MSWIA-7 and **d]** MSWIA-8.

Low magnification (25 to 50x) spectral maps were also generated for each ash type using the ThermoFisher Scientific NSS software. Figure 19 shows a typical elemental map for a combined ash sample (MSWIA-3). Although this is not a quantitative analysis, these maps help visualize the distribution and relationship among elements found in ash samples. For example, it is apparent that MSWIAs are comprised of oxides or minerals with complex compositions based on the overlap of elemental maps for oxygen with silicon, aluminum, iron, and calcium. Nearly all iron is oxidized to some extent during incineration, and elemental maps show the enrichment of iron-bearing particles with other heavy metals such as titanium, copper, chromium, and zinc.

Other research has investigated the occurrence and distribution of these primary iron-rich phases in MSWIA bottom ash as well as secondary iron-rich phases produced as a result of natural weathering in deposited bottom ash piles (Saffarzadeh and Shimaoka, 2014).

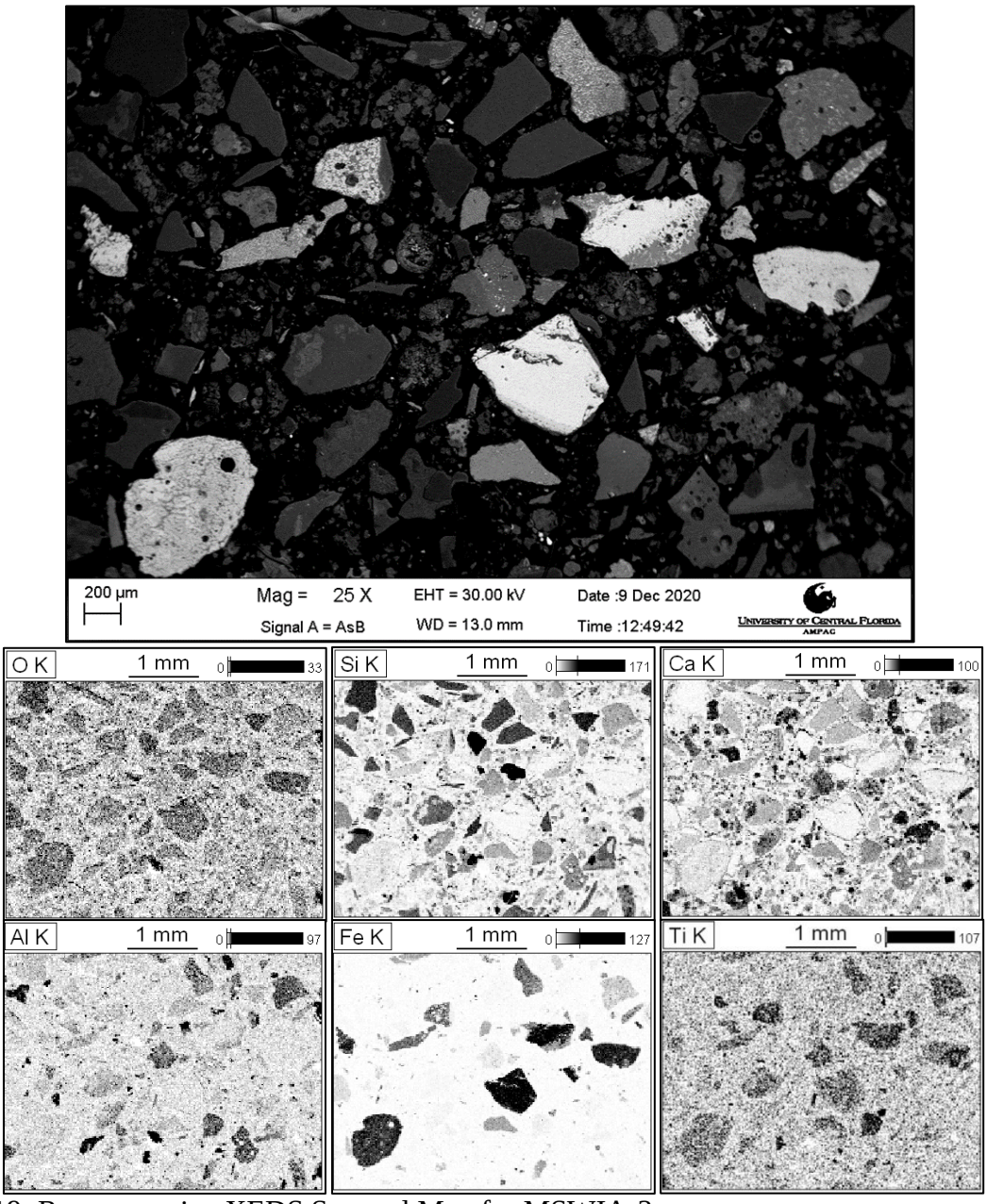

Figure 19: Representative XEDS Spectral Map for MSWIA-3.

From these spectral maps, iron was found to be predominantly associated with oxides and some Ca-Al-Si phases. It is unknown at this point to what extent the reactive iron 'cores' are protected by the oxide and hydration products that encapsulate the iron, especially long term. For example, primary-iron phases like magnetite (Fe_3O_4) are produced in the incinerator and can react in alkaline environments with moisture to produce secondary-iron phases like goethite ($Fe(OH)_3$). These newly-formed phases may produce some oxide-hydroxide films that can protect the central reactive phases from further corrosion or destabilization processes (Saffarzadeh and Shimaoka, 2014).

In a similar manner, aluminum was typically associated with calcium- and silicon-rich phases, often as a glassy matrix with other minor inclusions. Previous research has shown that many of the aluminum-bearing amorphous phases in ash are hindrances to the applicability of ash as supplementary material for building and construction projects because of undesired hydrogen gas generation and self-hardening of ashes due to cementitious reactions (Chancey et al., 2008; Calder and Stark, 2010; An, 2015). In their study, Speiser et al. comments that the thermal degradation of calcite ($CaCO_3$) to lime (CaO) in the incineration chamber produces ash particles with pores due to the degassing of chemically bound CO_2. During quenching, most of this lime is converted to portlandite ($Ca(OH)_2$) because of ash hydration, except for some lime found in the pores which are protected from contact with water. Following quenching, the generated ash undergoes cooling and may experience cracks due to volume contraction which permits water to enter these pores and convert remnant lime to portlandite (Speiser et al., 2000). However, there are additional processes occurring which result in the formation of hydration products enriched in silicon, aluminum, calcium, and iron that nucleate in these cavities after

quenching. Over time, these hydration products may form a protective reaction shell surrounding the ash particle that inhibit further transformation processes (i.e., corrosion, carbonation, dissolution, and precipitation). These glassy aluminum-containing phases have also been shown to contain a large number of fractures and other vesicles which may permit the flow of water or gas into the pore space, thus encouraging these same transformation processes (Wei et al., 2011).

XEDS 'point-and-shoot' images show that many MSWIAs contained iron-rich particles with dendritic structures that were not found in CCAs. These dendritic structures form as a result of the rapid cooling of ash particles containing partially molten iron produced in the incineration chamber. Figure 20 shows an ash particle with a relatively pure iron oxide core (Point 1) and typical iron dendrites (Point 3) which nucleated and grew out of a Ca-Al-Si-rich matrix (Point 2) during cooling. XEDS analysis shows these dendrites to be enriched in iron with some silicon, likely in the form of fayalite (Fe_2SiO_4), while the iron core may be wustite (FeO) as observed in a previous study investigating iron smelting slag (Klemm et al., 2012). Iron in coal ashes, on the other hand, was never found in this as-solidified dendrite form likely due to the absence of large iron scrap wastes that are commonly found in MSW. Table 9 presents compositional information for all ashes which was determined via XEDS by performing area scans across random locations and neglecting the influence of carbon, oxygen, and gold on determined concentrations. Carbon was neglected due to the use of a carbon-rich epoxy to embed these ashes for polishing, while gold was neglected because a thin layer was manually deposited to ensure conductivity, and oxygen was neglected because quantitative XEDS results are not as reliable for elements lighter than sodium. Similar to results from XRF analysis, MSWIAs contained nearly double the amount of iron compared to CCAs, except for MSWI fly ash samples (MSWIAs-7 and 9).

Aluminum, on the other hand, was typically found in greater quantities in CCAs than for MSWIAs. MSWI fly ashes also tended to contain greater contents of chlorine than other ashes (except CCA-3) as a result of acid-gas removal. Across all samples, calcium and silicon were found to be the dominant phase present, likely in the form of the calcium-aluminum-silicate glassy phases found in abundance via XRD and SEM/XEDS. These glassy matrices have a high affinity for metal entrapment, yielding mineral phases with different minor inclusions and may serve as a passivating layer protecting these inclusions at shorter timescales.

Although excluded from our modeling efforts, additional exothermic reactions involving these glassy and mineral phases are likely to take place in landfill environments. For example, a previous study found that MSWI bottom ash was comprised of up to 50% glassy phases; at a pH>9 the critical glass-forming element silicon dissolves which would allow for the dissolution and release of elements bound in the glass matrix (Wei et al., 2011). And, since aluminum and iron were detected within these glassy phases in the current study via XEDS (Figures 19 and 20), there is a strong potential for exothermic reactions to take place involving these metals upon silicon dissolution, whether via metal oxidation or precipitation as some new mineral phase. Calcium products like portlandite may also react with silica to exothermically form amorphous calcium silicate hydrate phases ($Ca(OH)_2 + SiO_2 \leftrightarrow CaH_2SiO_4$; ΔH_{rxn}= -40 to -140 kJ/mol) (Speiser et al., 2000). Hence, it would be important to the solid waste industry to understand the mechanisms surrounding the dissolution of these complex mineral phases and the subsequent fate of the metals embedded within these calcium-silicon-rich matrices.

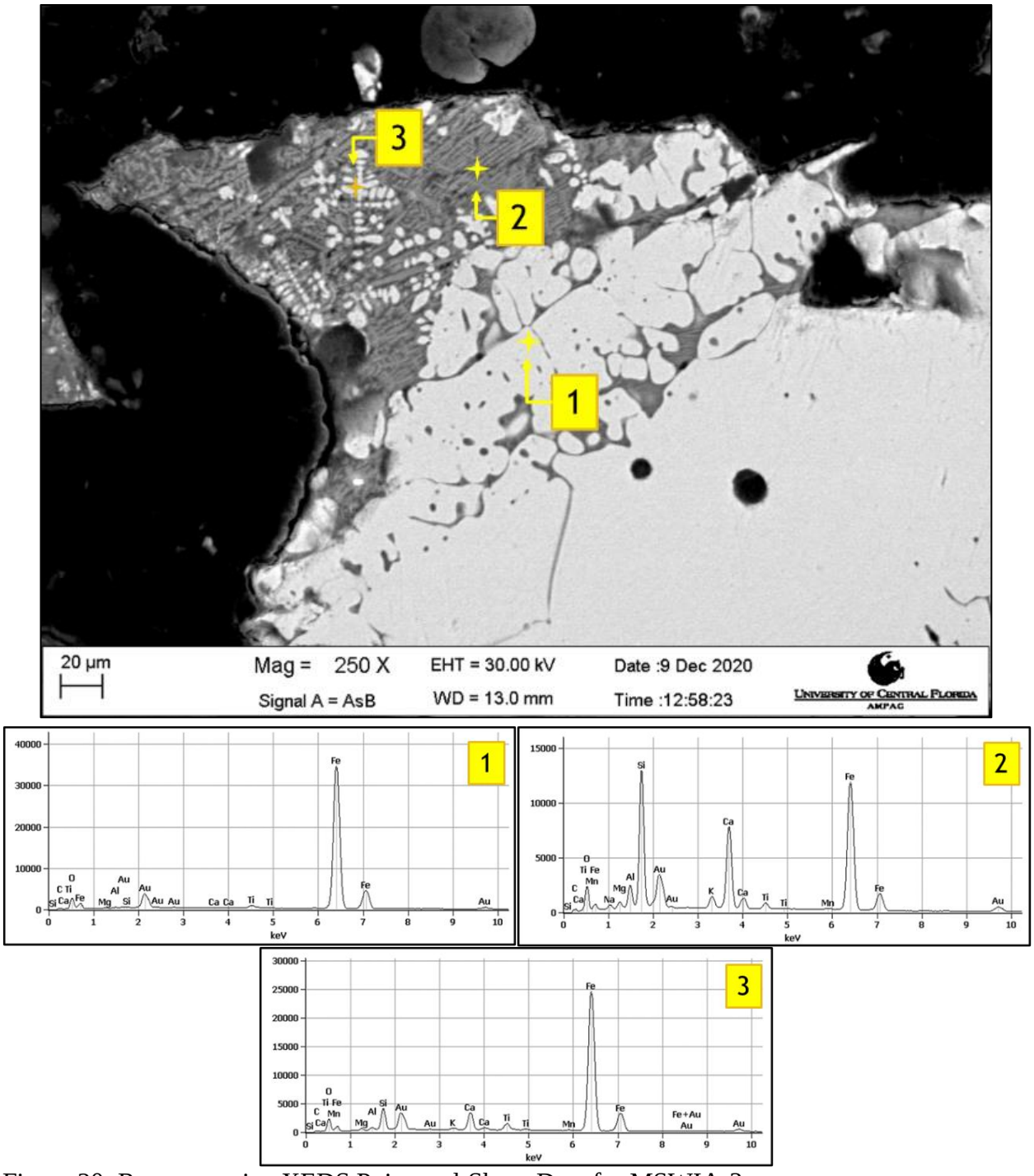

Figure 20: Representative XEDS Point-and-Shoot Data for MSWIA-3.

Note: Gold (Au) was detected because the sample was sputter coated with a thin layer to reduce the effects of 'charging'.

Table 9: XEDS Data for All Ash Samples

Sample Type	Average Concentration (Weight %)													
	Na	Mg	Al	Si	Cl	K	Ca	Ti	Cr	Mn	Fe	Cu	Zn	S
CCA-1	1.7	3.0	15.2	36.6	2.8	0.9	29.7	2.4	0.0	0.0	7.5	0.0	0.0	0.0
CCA-2	1.3	2.8	15.3	38.8	3.2	0.9	28.2	2.3	0.0	0.0	7.3	0.0	0.0	0.0
CCA-3	0.0	0.7	4.1	7.5	13.2	0.7	60.9	0.3	0.0	0.0	3.9	0.0	0.0	8.6
CCA-4	4.1	2.6	13.6	30.5	6.5	1.0	28.7	2.1	0.0	0.0	6.1	0.0	0.0	4.8
CCA-5	0.1	1.7	13.6	36.1	4.1	1.6	32.9	1.5	0.0	0.3	4.6	0.0	0.0	3.5
CCA-6	0.0	0.6	9.5	19.9	4.2	1.3	48.8	1.1	0.1	0.0	4.2	0.0	0.0	10.6
MSWIA-1	3.9	2.1	12.0	29.9	3.3	1.2	24.9	1.0	0.2	0.3	16.9	0.4	1.2	0.0
MSWIA-2	12.2	0.7	5.8	23.3	6.7	2.4	29.9	1.4	0.1	0.1	14.2	0.8	0.9	0.0
MSWIA-3	0.0	0.8	5.6	23.5	6.9	1.7	38.3	1.7	0.1	0.2	18.1	0.1	1.1	0.0
MSWIA-4	1.8	1.5	6.7	30.8	4.5	1.7	28.3	2.8	0.2	0.3	17.9	0.1	1.0	0.0
MSWIA-5	2.9	1.7	9.3	26.5	5.3	1.5	26.4	1.6	0.1	0.3	18.6	0.9	1.3	0.0
MSWIA-6	7.4	2.1	8.1	40.7	3.2	1.3	29.1	1.6	0.1	0.2	5.5	0.7	0.1	0.0
MSWIA-7	2.3	1.2	3.3	24.1	12.0	0.8	49.3	1.4	0.1	0.0	1.7	0.0	0.8	3.1
MSWIA-8	3.8	1.3	1.7	42.3	3.0	0.9	28.3	0.4	0.1	0.0	15.7	0.1	0.3	2.1
MSWIA-9	0.6	1.4	1.7	20.9	11.9	0.9	50.2	0.7	0.0	0.0	1.2	0.0	2.9	7.8
MSWIA-10	3.9	1.1	5.0	21.2	7.9	1.3	47.1	1.0	0.1	0.2	6.6	0.2	0.9	0.0

Note: Concentrations were obtained by averaging XEDS data for three random locations across the sample's surface.

4.2 Modelling Efforts

As described in Chapter 3, a simple model (Equation 1) was developed based on published reactions (Table 2) relevant to CCAs and MSWIAs to calculate a value termed Relative Heat Potential (RHP). A Monte Carlo simulation was performed using quantitative elemental data obtained via XEDS (Table 9) as model input to gain a deeper understanding of the RHP for CCAs and MSWIAs (e.g., relative values, uncertainty, parametric sensitivity). For this model, a baseline RHP value was calculated using an average composition for MSWIAs and CCAs and a number of assumptions (Table 3) regarding the *fraction available* (f_i) parameter. Then, a parametric study was conducted to observe the influence of each reaction type on RHP by varying f_i. CCA-6 was not included in this analysis as measured characteristics show that it is an outlier because of the influence of WWTP biosolids.

4.2.1 Monte Carlo Simulation for 'Baseline Case'

For the baseline case, results comparing typical CCA and MSWIA heat production values are presented in Figure 21. As can be seen, this baseline condition yielded average RHP values for CCAs and MSWIAs of 3,700 and 3,300 kJ/kg ash, respectively. This 13% difference in RHP is significant, as discussed shortly, and shows that, for representative CCA and MSWIA compositions, the potential for heat generation when deposited in a landfill is greater for CCAs than for MSWIAs. Although they were not considered in this modelling effort, the influence of particle size and chlorine content may compound this finding due to increased metal corrosion and surface area available for reactions to take place. The baseline average RHP values for MSWIAs and CCAs fall between reported values for the aerobic and anaerobic decomposition of organic waste, with glucose as a representative carbon source. These values are -1,770 kJ/mol (-

9,830 kJ/kg $C_6H_{12}O_6$) and -100 kJ/mol (-555 kJ/kg $C_6H_{12}O_6$) for aerobic and anaerobic decomposition, respectively (Geosyntec Consultants, 2014). Using these values as a reference, heat generation from landfilled MSWIAs and CCAs is roughly 30% of the total heat generated due to aerobic waste decomposition, and roughly six times greater than the heat from anaerobic waste decomposition.

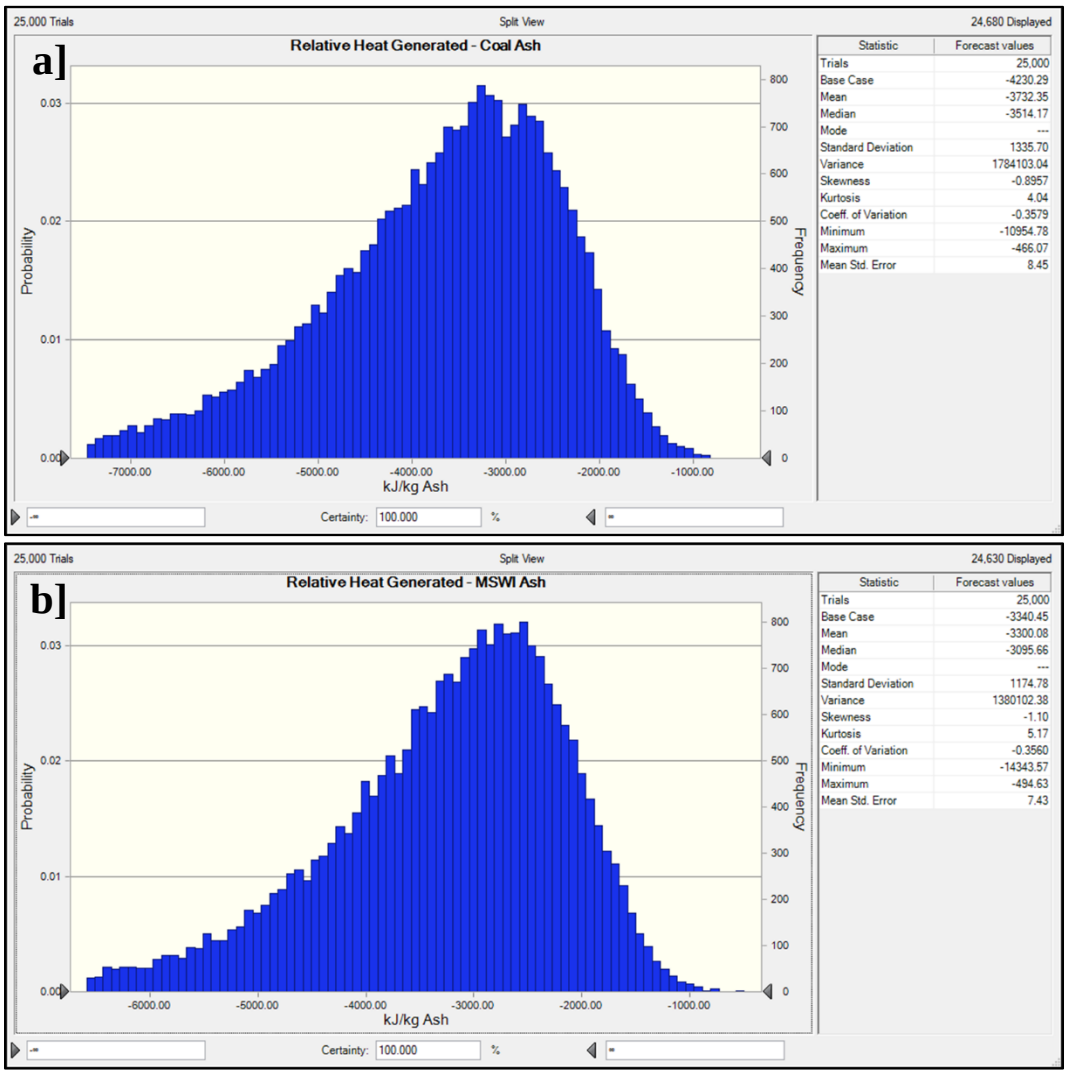

Figure 21: Comparison Between Baseline Relative Heat Potential Values for **a]** CCAs and **b]** MSWIAs.

To examine the effects of individual ash compositions on variations in RHP, this same analysis was applied based on respective XEDS concentrations for each ash; findings are summarized in Figure 22. Additionally, a two-tailed independent t-test was performed to explore the significance of the difference in calculated RHP. Findings show that CCAs (M=3890 kJ/kg, SD=444 kJ/kg) produced significantly more heat than MSWIAs (M=3130 kJ/kg, SD=568 kJ/kg) for the same model parameters; $t(14)=3.02$, $p=.009$. The increased RHP for some CCAs compared to MSWIAs is likely due to the magnitude of the enthalpy associated with aluminum- and iron-based reactions (-31,000 kJ/kg Al for the amphoteric aluminum reaction compared to -1,630 kJ/kg Ca for calcium hydration), and the greater content of aluminum in CCAs and MSWIA-1 compared to the remaining MSWIA samples (Table 9). Despite MSWIAs having greater amounts of iron compared to CCAs, the alkaline pH of ashes provide aluminum with an additional amphoteric reaction that iron cannot participate in, hence under these high-pH conditions, aluminum is expected to be more active in exothermic reactions when deposited in landfills. To verify the increased exothermic activity associated with greater aluminum concentrations, plots of RHP vs Al and Fe Contents were developed and are presented in Figure 23. Figure 23a highlights the direct relationship between heat generation and Al content for both CCAs and MSWIAs, but no such trend could be observed for changes in Fe content (Figure 23b). This implies that rigorous non-ferrous (aluminum) metal recovery in MSW WTE facilities may result in the greatest reduction in potential exothermic activity for ashes when co-disposed with unburned MSW in landfills, although ferrous metal recovery is also recommended due to the abundance of Fe detected in many MSWIA samples.

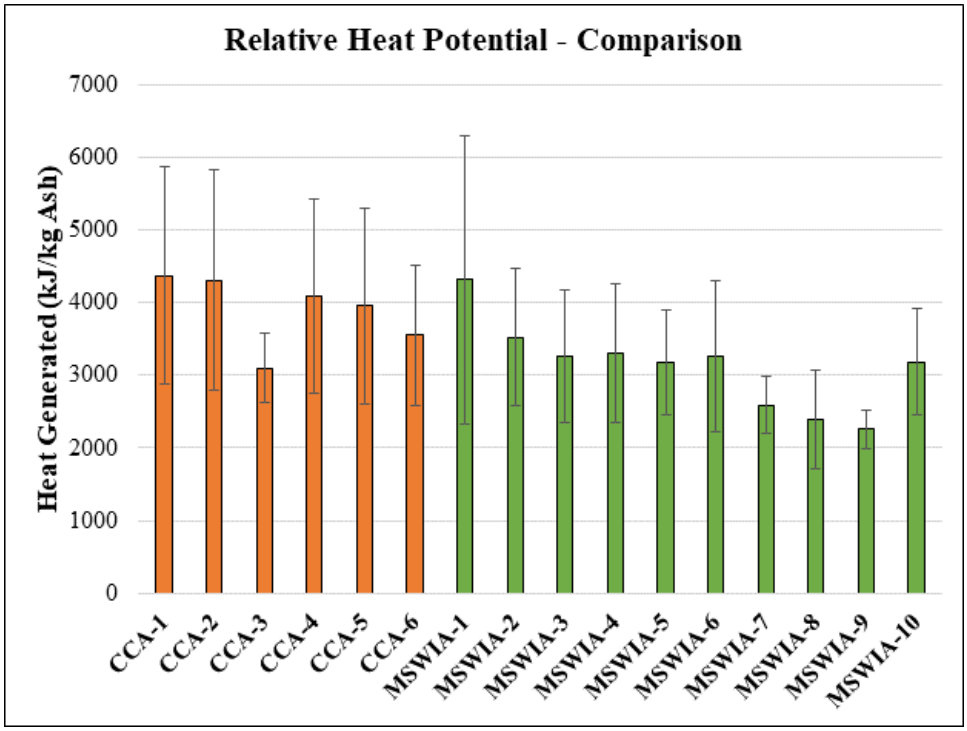

Figure 22: Monte Carlo Analysis - Comparison of Relative Heat Potential (RHP) (kJ/kg) for CCAs and MSWIAs

Note: Error bars are based on standard deviations of RHP values across all 25,000 iterations for each ash sample.

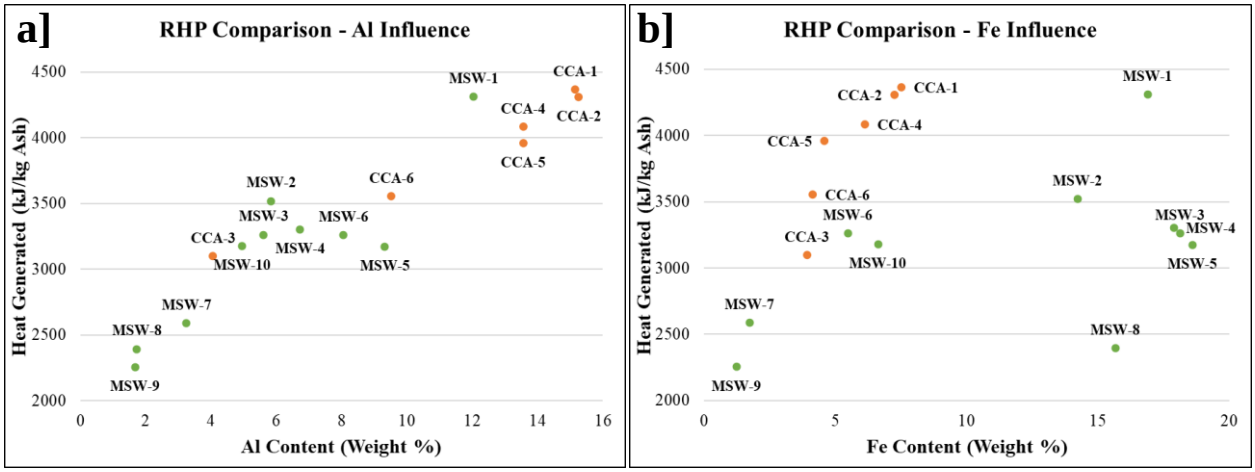

Figure 23: Monte Carlo Analysis – Influence of **a]** Al Content and **b]** Fe Content on Relative Heat Potential (RHP) for CCAs and MSWIAs.

4.2.2 Monte Carlo Simulation Parametric Study

To gain further insight into the effects of the *fraction available* (f_i) of each element for each reaction type on RHP, one fraction was sequentially increased from 0 to 1 (Figure 24) while all other reactions were varied using the Crystal Ball software and previous assumptions. Physically, a f_i value of 0 signifies that none of element *i* is available to partake in that reaction (i.e., a $f_{oxid,Fe}$ value of 1 means that all of the observed iron was available for oxidation). While it is not expected that these fractions will achieve a value of 1 in real systems, especially for metal oxidation and corrosion reactions, this study was useful in highlighting which reactions contribute most to heat generation based on observed, representative XEDS compositions. The same process was conducted for f_i values from 0 to 0.1 to gain an understanding of how RHP varies at this low fraction range (Figure 24c and 24d). RHP values were determined for each increment of f_i and plotted as a function of *f*. Because of the comparable magnitude between ΔH_{rxn} for aluminum oxidation and amphoteric reaction, their trends were very similar throughout this parameterization and thus only $f_{oxid,Al}$ is shown in Figures 23 and 24. In addition to the summary presented in Figures 23 and 24, the maximum RHP values obtained throughout this parameterization are presented in Table 10 for CCAs and MSWIAs, as well as the calculated percent difference between the two ash types.

Table 10: Parametric Study - Comparison of Maximum Relative Heat Potential (RHP)

Condition	Maximum RHP (kJ/kg)		Percent Difference (%)
	MSWIA	CCA	
f_{hyd}	3,530	3,980	12.5
f_{carb}	3,480	3,920	12.7
$f_{oxid,Al}$	4,780	6,360	33.1
$f_{corr,Al}$	4,050	5,090	25.7
$f_{amph,Al}$	4,800	6,380	33.1
$f_{oxid,Fe}$	4,560	4,360	- 4.40
$f_{corr,Fe}$	3,390	3,791.3	11.7
Baseline	3,300	3,730	13.1

Note: $\boldsymbol{Percent\ Difference}\ (\%) = \frac{RHP_{CCA} - RHP_{MSWIA}}{RHP_{MSWIA}} * 100\%$; a negative Percent Difference correlates to a greater RHP for MSWIAs vs CCAs for a given condition.

When comparing the maximum RHP values from Table 10, it can be seen that CCAs demonstrated a greater heat generation potential than MSWIAs across all parameterizations, except where MSWIAs had higher iron availability for oxidation (greater $f_{oxid,Fe}$) which produces slightly more (4%) heat due to increased iron concentrations in the combined and bottom ash samples. A review of Figure 24 shows that, for MSWIAs at respective fractions greater than 0.4, both iron and aluminum oxidation were the dominant heat-generating reactions and the slope of these curves indicate that the calculated RHP was most sensitive to changes to these fractions. For CCAs, aluminum oxidation and corrosion were the dominant heat-generating reactions because of the reduced iron contents found in coal ash samples. When f < 0.1, (Figure 24a and 24b) it can be seen that iron oxidation played a critical role in heat-generation for both MSWIAs and CCAs, hinting that there is some threshold around $f_i = 0.2$ which signals the transition from

iron-dominating to aluminum-dominating heat-generation mechanisms. This is likely due to the increased stability of aluminum oxides compared to iron oxides (Table 3), meaning there is less aluminum available to react than iron. However, above this threshold the magnitude of the heat generated from aluminum oxidation trumps the effects of oxide stability and so aluminum contributes the most heat to the system. It was also interesting that, despite the greater abundance of alkali and alkaline earth metals, variation in carbonation and hydration reactions resulted in the lowest changes to RHP calculated across all parameterizations.

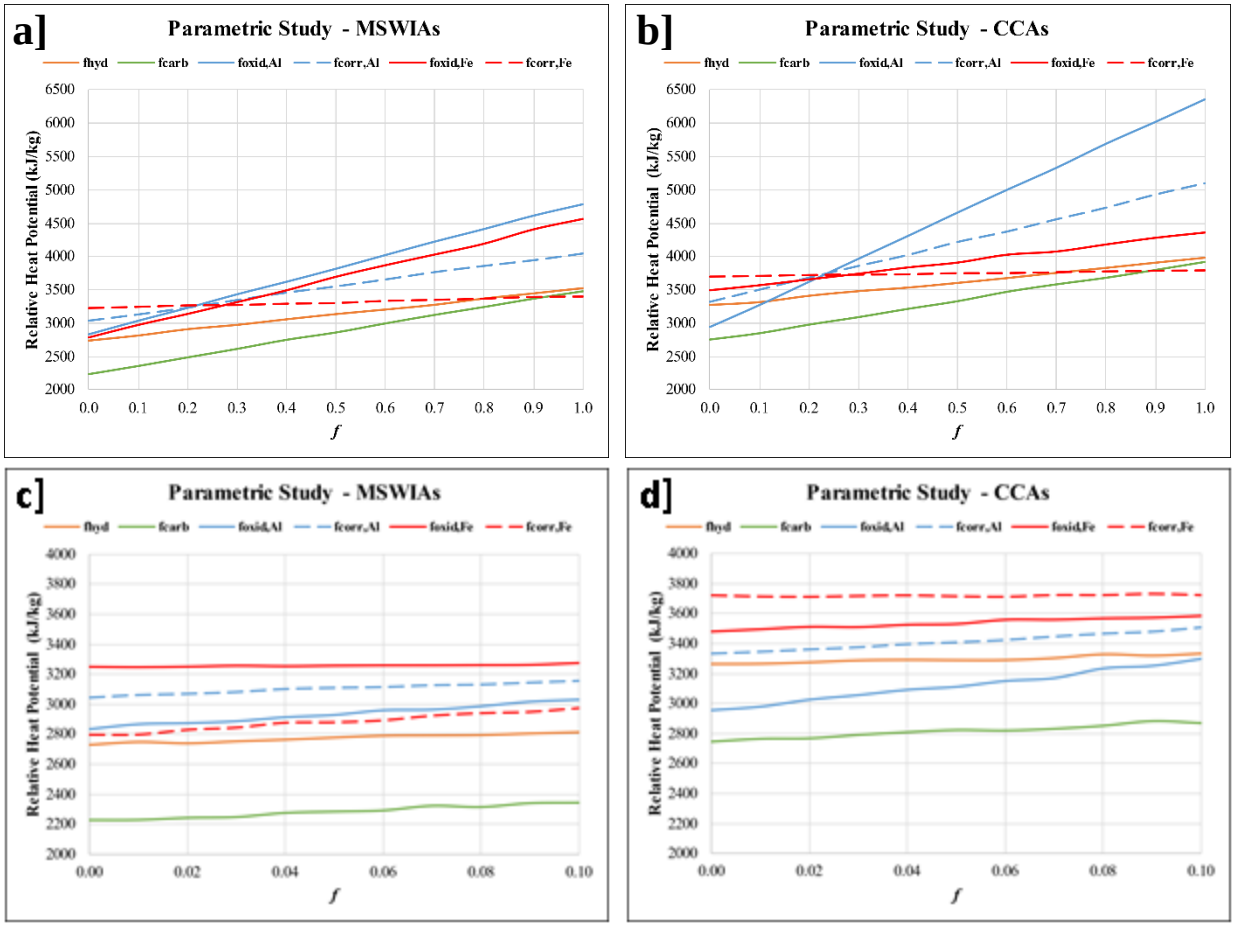

Figure 24: Monte Carlo Analysis - Parametric Study Results for $0<f<1$ Range for **a]** MSWIAs and **b]** CCAs, and for $0<f<0.1$ Range for **c]** MSWIAs and **d]** CCAs.

CHAPTER 5 CONCLUSIONS AND FUTURE WORK

5.1 Conclusions

Rigorous characterization efforts for ten MSWIAs and six CCAs revealed that all ashes were highly alkaline (pH>10) except for one coal + WWTP biosolids mixture (CCA-6), and were comprised of complex, heterogeneous mineral and glassy phases enriched in calcium, silicon, aluminum, and iron. SEM images and PSA results showed that coal ashes were significantly finer than MSWIAs for both bottom and fly ash fractions ($t(178)=6.81$ and $t(178)=12.0$, respectively), and morphologies of coal ashes tended to be spherical compared to the highly-irregular MSWIAs. The amorphous, or non-crystalline, content of these ashes made complete characterization via XRD difficult but common phases identified were quartz (SiO_2), anhydrite ($CaSO_4$), sylvite (KCl), halite (NaCl), hydrocalumite ($Ca_2Al(OH)_6Cl(H_2O)_2$), and other calcium-aluminum-silicate (CAS) minerals. Iron was commonly detected via XRD as hydroxides ($Fe(OH)_3$), and sometimes as magnetite (Fe_3O_4) and hematite (Fe_2O_3) which is consistent with literature. SEM/XEDS analysis and XRF ternary diagrams highlight the greater contents of iron in MSWIAs compared to CCAs, and XEDS 'Point-and-Shoot' results showed the presence of wustite (FeO) and silicon-enriched fayalite (Fe_2SiO_4) dendritic structures in MSWIAs that were not present in CCAs. Iron was also closely associated with other heavy metals such as nickel, zinc, copper, and lead. Aluminum, on the other hand, was found in greater concentrations in CCAs than MSWIAs and was closely associated with calcium- and silicon-bearing phases, likely in the form of glassy CAS phases which have been noted to be highly reactive and problematic in building and construction applications, although the extent of reactivity and heat generation associated with these phases is unknown.

TGA results shed light on the fact that MSWIAs were significantly more susceptible to thermal degradation than CCAs, $t(13)=3.43$, $p=.004$, as evidenced by the greater average weight loss for MSWIAs (14%) compared to CCAs (4.5%). The same trend is true for fly ashes compared to bottom ashes, for both CCAs ($t(3)=26.2$, $p=.0001$) and MSWIAs ($t(2)=17.0$, $p=.003$). The weight loss associated with the temperature range of 600 to 780°C for most samples highlights the fact that carbonation likely converted much of the existing portlandite ($Ca(OH)_2$) to calcite ($CaCO_3$) prior to our analysis. Hence, the carbonation of existing hydrated materials in combustion ashes is likely to take place prior to their deposition in landfills. The lack of observance of pure metals (like elemental Al and Fe) and some metal oxides (like CaO) via XRD and SEM/XEDS show the complex effects of aging, or weathering, on ash constituents that convert these highly reactive phases into metastable mineral forms.

To quantify the effects of the calcium-, aluminum-, and iron-bearing phases identified via spectroscopic analyses, a simple model was used to approximate the heat generating potential for each ash through a parameter termed Relative Heat Potential (RHP) (kJ/kg ash). Reactions pertaining to the observed complex mineral phases are limited in literature and thus were excluded from modeling efforts. The RHP value was calculated using published enthalpies of reaction (ΔH_{rxn}) for ash hydration, carbonation, metal corrosion and oxidation, and the amphoteric reaction of aluminum. These enthalpies were used in conjunction with XEDS concentrations (C_i as weight %) and assumed fraction availability (f_i) to calculate a representative RHP value for not only each individual ash sample, but also MSWIAs and CCAs as a group. For typical CCA and MSWIA compositions (baseline case), model results show that coal ashes have a significantly greater RHP (3,700 kJ/kg ash vs 3,300 kJ/kg ash) than MSWI ashes, $t(14)=3.02$,

p=.01, primarily due to differences in aluminum and iron concentrations. A parametric study was conducted to understand the influence of each modelled reaction type on heat generation, and results show that aluminum oxidation and amphoteric reactions most significantly influence predicted heat generation for both ash types (CCAs and MSWIAs), but iron oxidation is also important for MSWIAs due to the greater abundance of iron in MSW ashes than in coal ashes. At this point, the stability of iron- and aluminum-bearing phases in ashes is unknown, especially in rugged and alkaline environments like landfills – stability here refers to the persistence of passivating oxide shells and glassy matrices that encapsulate many ash constituents. Dissolution of zero valent metals increases the probability of a great deal of heat generation by reactions pertaining to these metals and others found in raw MSW. Therefore, it may be a good practice for WTE plant operators to enforce, at a minimum, ferrous and non-ferrous metal recovery as a measure to mitigate the occurrence of ETLFs. It may also be beneficial to age ashes such that the metastable mineral forms are fully converted to stable end-products, and to ensure that environmental conditions, like surrounding pH, are maintained at a level that preserves these complex mineral phases.

5.2 Future Work

Findings from this work highlight the importance of understanding both the exact speciation of metals in ashes, and the stability of their mineral forms at different timescales. If these passivating layers, whether oxide scales, hydration products, or protective glassy matrices, are destabilized or dissolved because of factors like chlorine content or pH changes, then the bound metals can be released and potentially participate in highly exothermic reactions after their deposition in landfills. It would thus be of interest to the solid waste community to

investigate the distribution of these mineral phases in ashes as a function of well-documented processing parameters such as incineration temperature and technologies, the type and efficiency of ferrous and non-ferrous metal recovery technologies, and the duration of ash weathering prior to final disposal in a landfill or ash monofill. The conditions required to ensure ash stability should also be investigated further, especially as it relates to pH as there is likely to be a tradeoff between operating at alkaline vs neutral pH values. For example, alkaline pH tends to promote the dissolution of silicon and the exothermic aluminum amphoteric reaction, while a lower pH may increase metal leachability and degrade some stable mineral phases like ettringite.

Future models should aim to account for additional reactions such as mineral dissolution and subsequent re-crystallization, aluminum- and iron-hydration, as well as other reactions involving metals which may be disposed of in increased frequency due to technological advances (e.g., lithium from e-waste). It would be of particular interest to expand upon already-published heat-generation models to account for changes in the mineral compositions found in ashes as a function of time and pH. Such a model might produce results that can serve as a guideline for the solid waste community to develop standardized methods for ash handling and treatment from its generation up until its ultimate disposal, with the goal of producing the most stable mineral phases. It would also be of interest for these models to investigate the influence of both disposal strategies within MSW landfill cells and pressure on reaction rates and heat generation after ash disposal. With regards to ash generation and handling practices, it may be of interest to WTE facility and landfill operators in the U.S. to establish standardized ash generation and handling procedures with the goal of producing a more consistent ash stream that may ultimately be co-disposed of with unburned MSW in Subtitle D landfills. And on a final note, as the amount of

MSW incinerated in the U.S. is expected to increase in the coming years, it would be beneficial not only to investigate alternative uses for both fly and bottom ashes in construction applications, but also to improve their efficiencies in such projects. This will help decrease the quantity of ash annually deposited in landfills, thus reducing a significant source of materials in landfills that are able to participate in exothermic reactions which may lead to the development and/or sustainment of elevated temperature landfills (ETLFs).

APPENDIX A: SEM BSE MICROGRAPHS

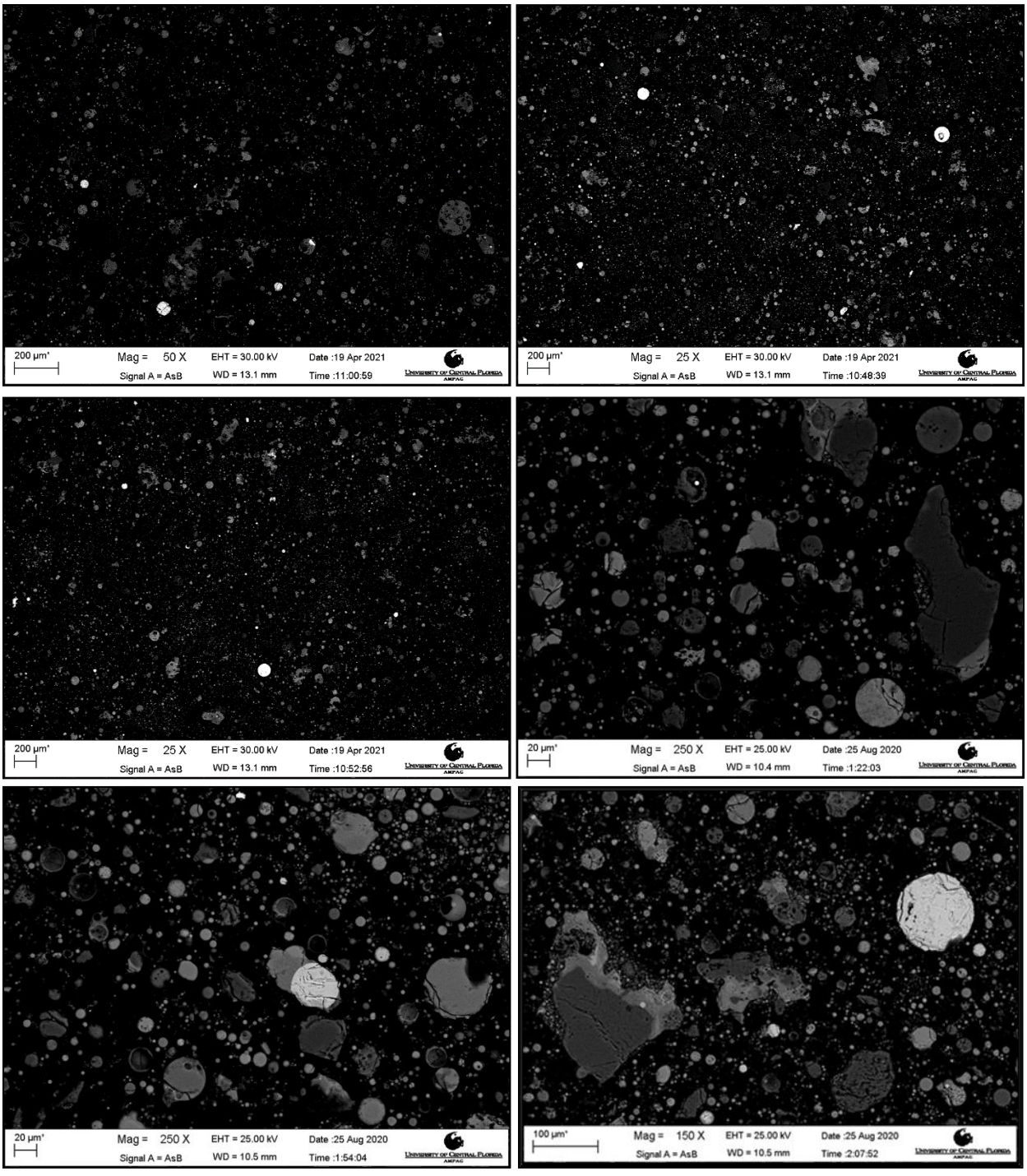

Figure A 1: Representative BSE Images of CCA-1

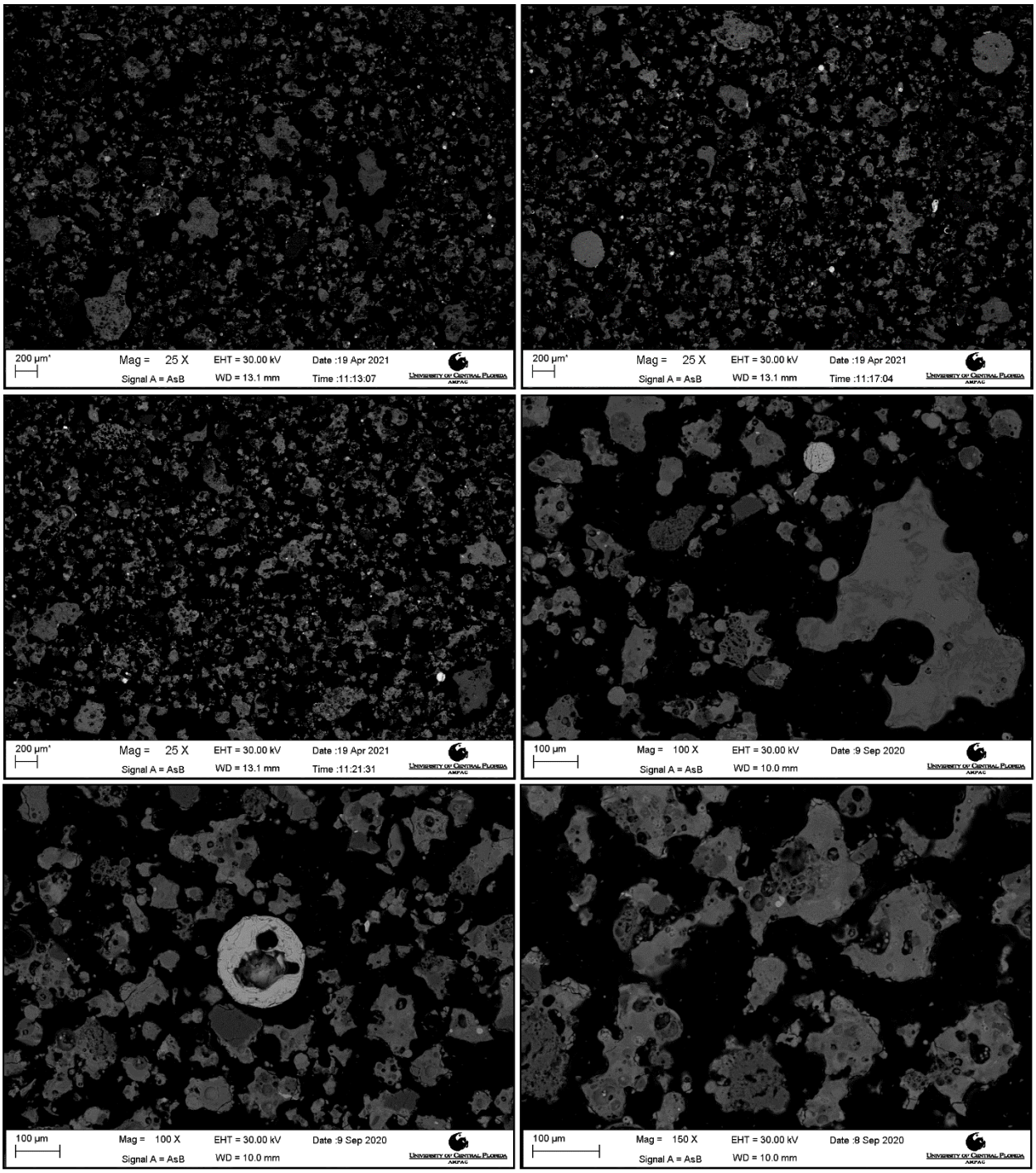

Figure A 2: Representative BSE Images of CCA-2

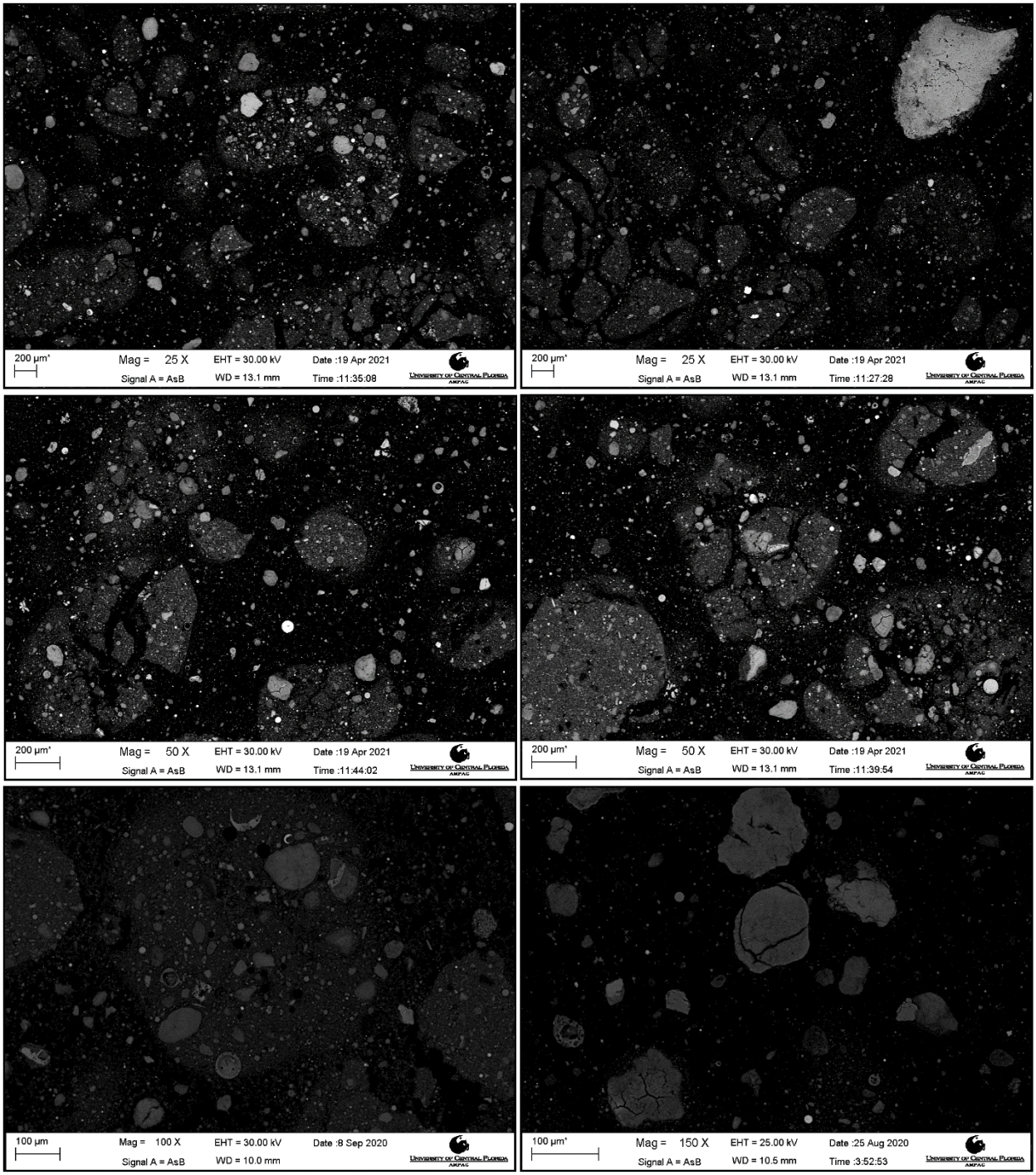

Figure A 3: Representative BSE Images of CCA-3

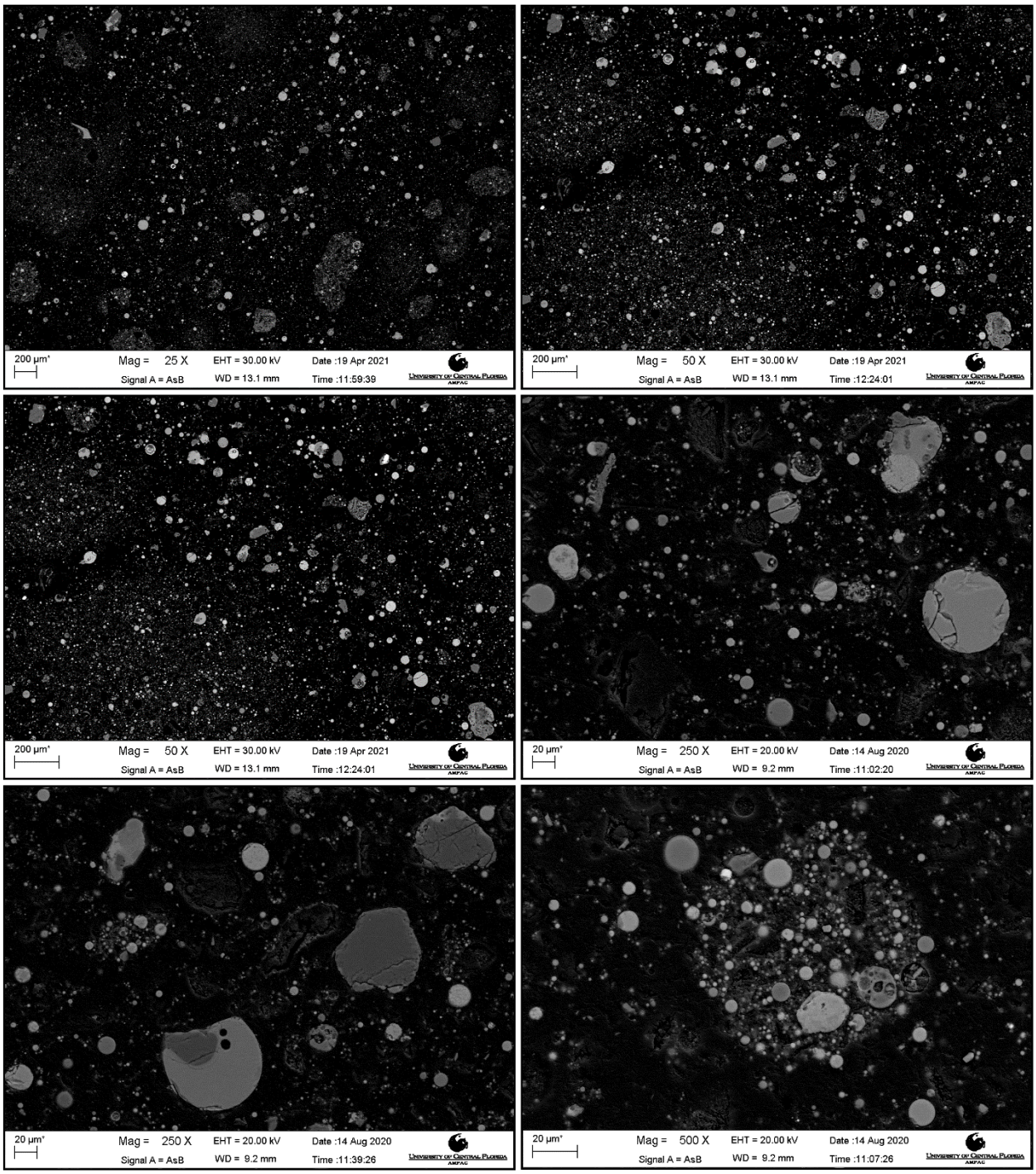

Figure A 4: Representative BSE Images of CCA-4

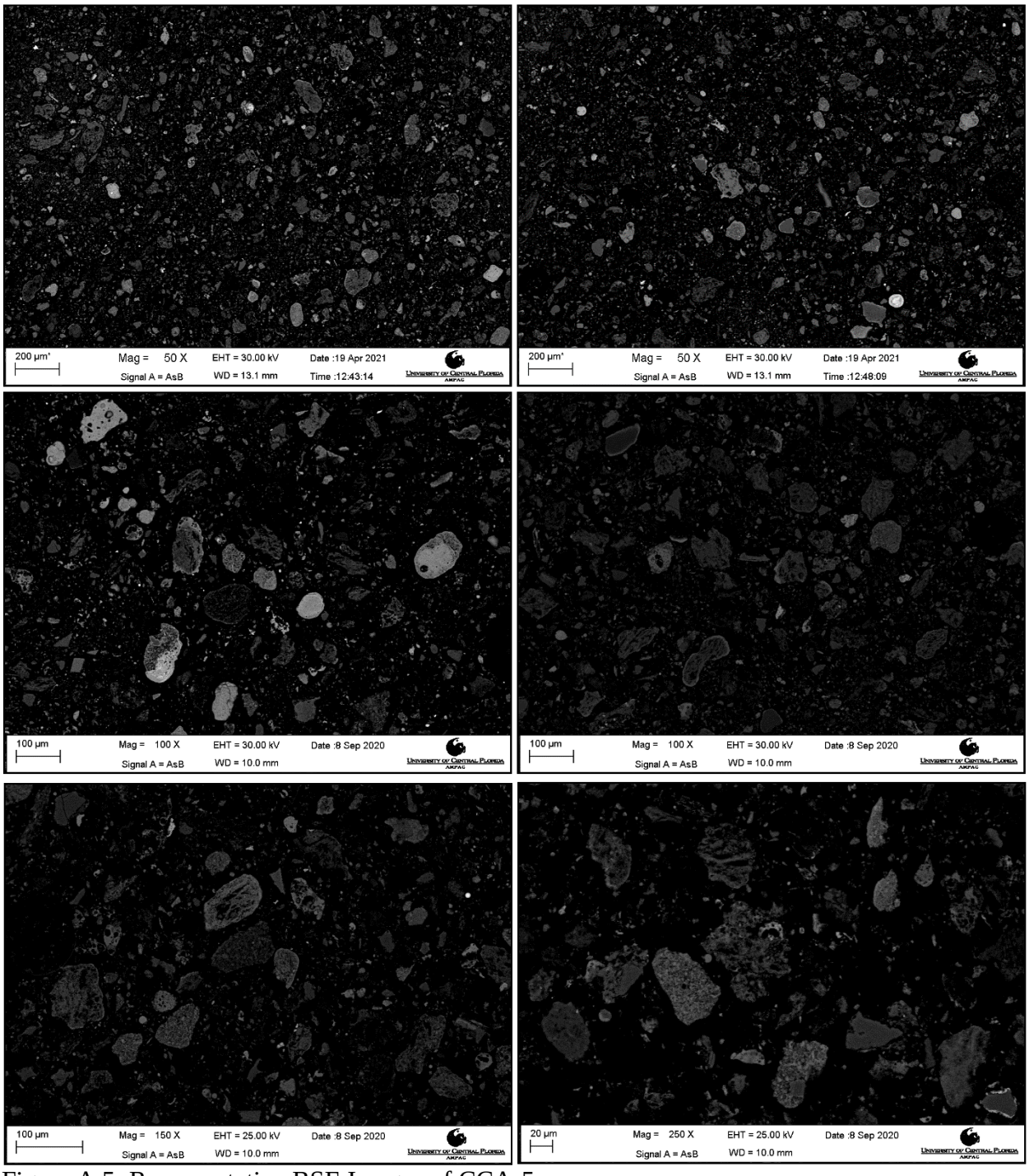

Figure A 5: Representative BSE Images of CCA-5

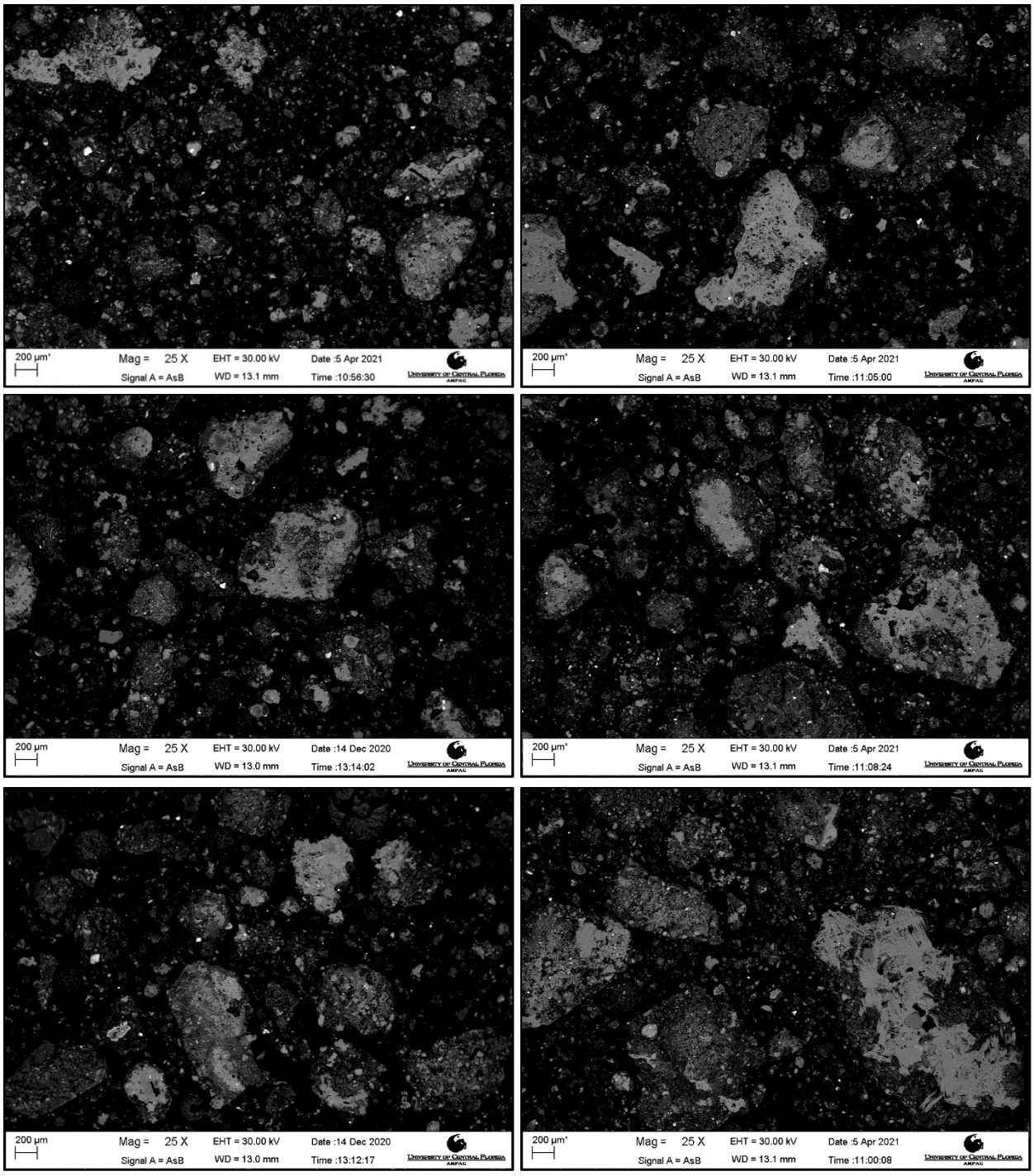

Figure A 6: Representative BSE Images of CCA-6

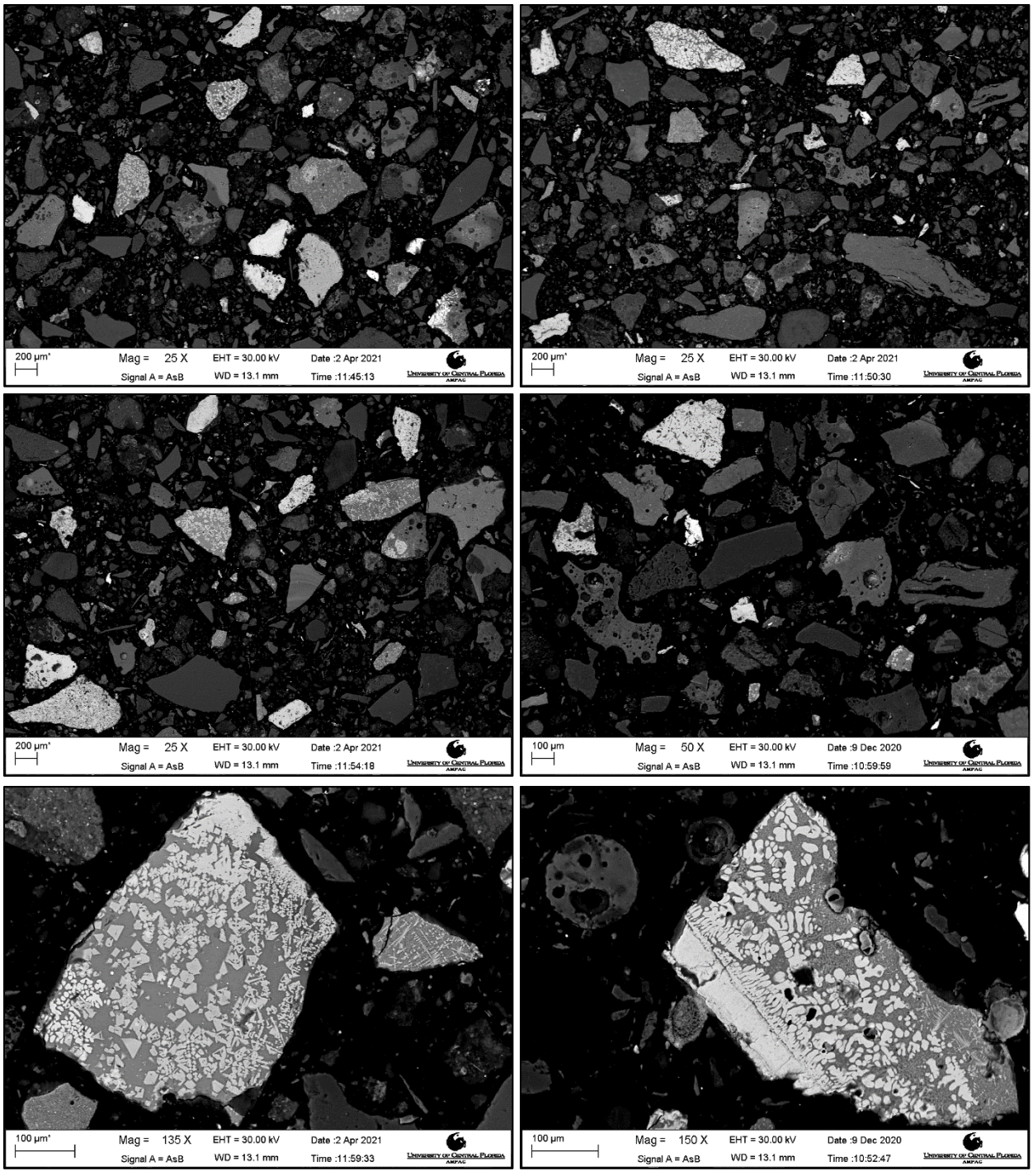

Figure A 7: Figure A 8: Representative BSE Images of MSWIA-1

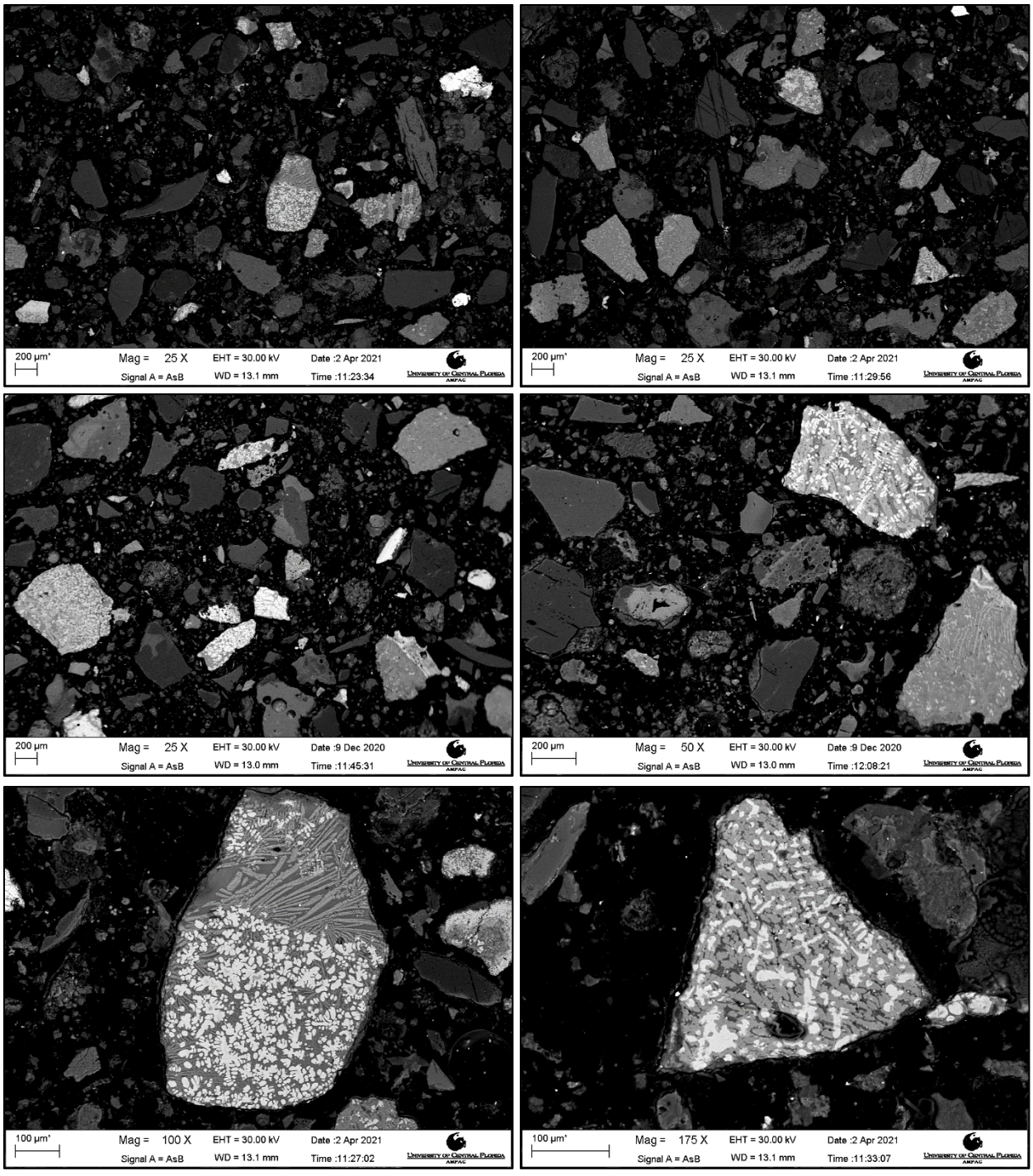

Figure A 9: Representative BSE Images of MSWIA-2

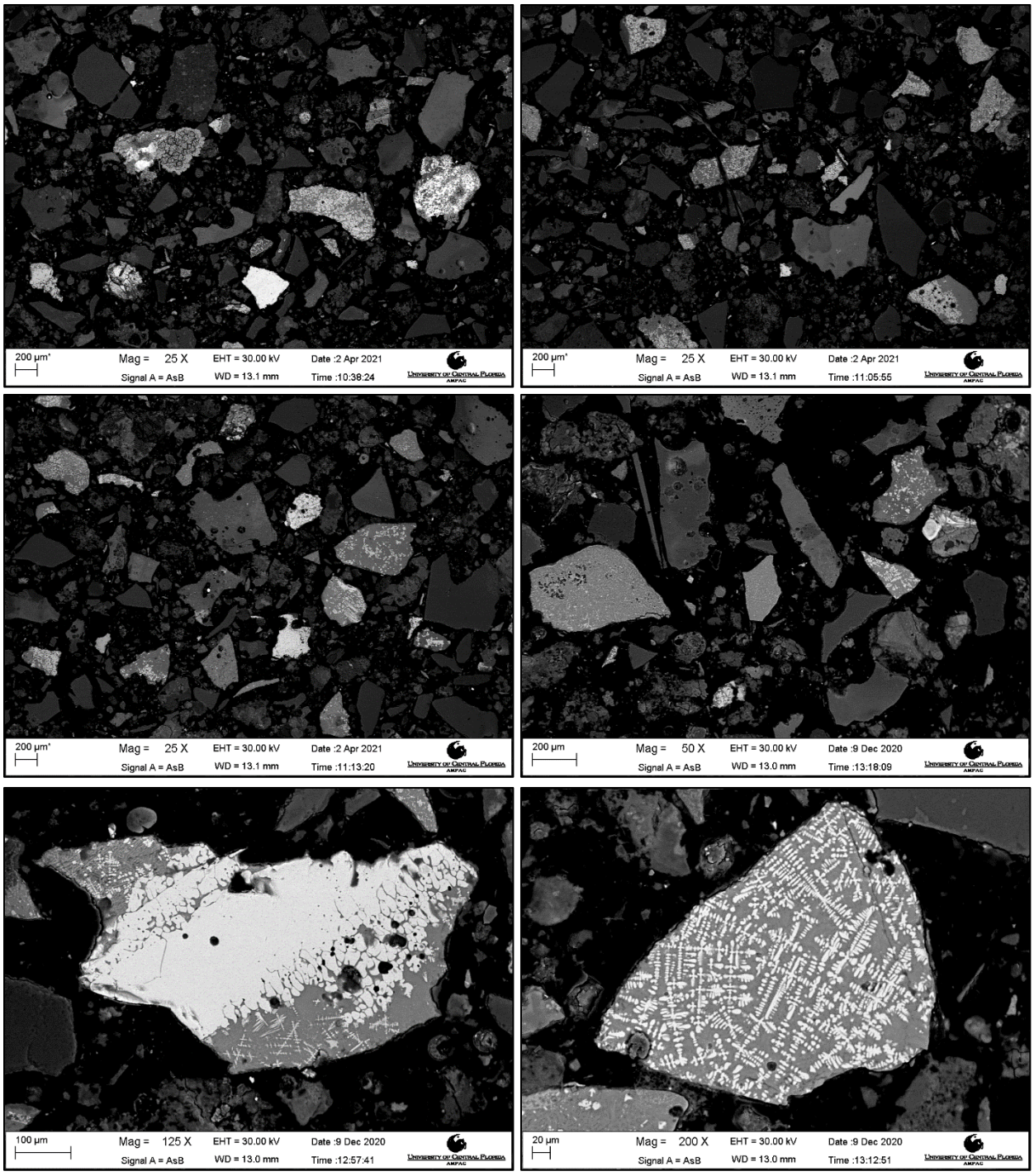

Figure A 10: Representative BSE Images of MSWIA-3

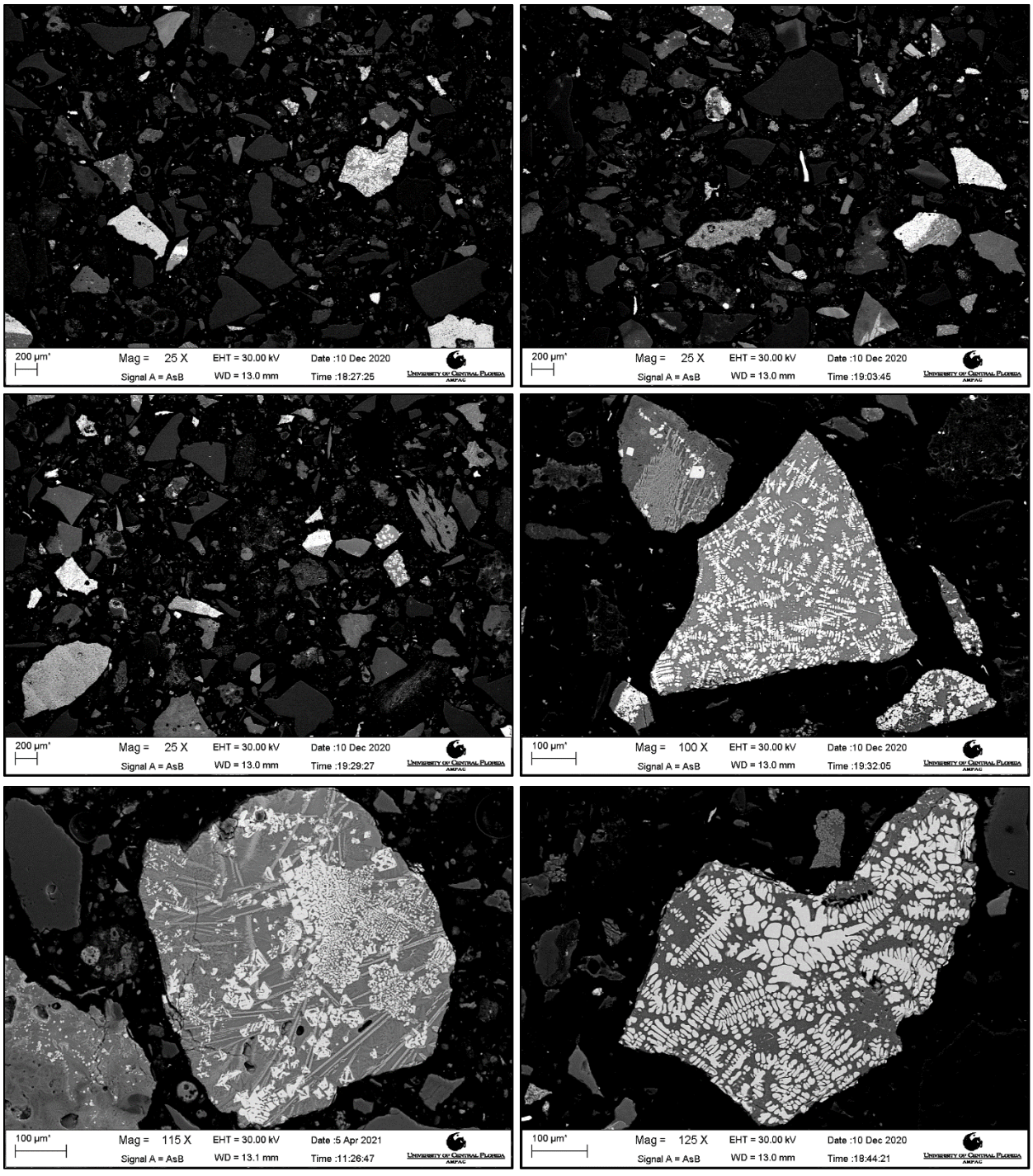

Figure A 11: Representative BSE Images of MSWIA-4

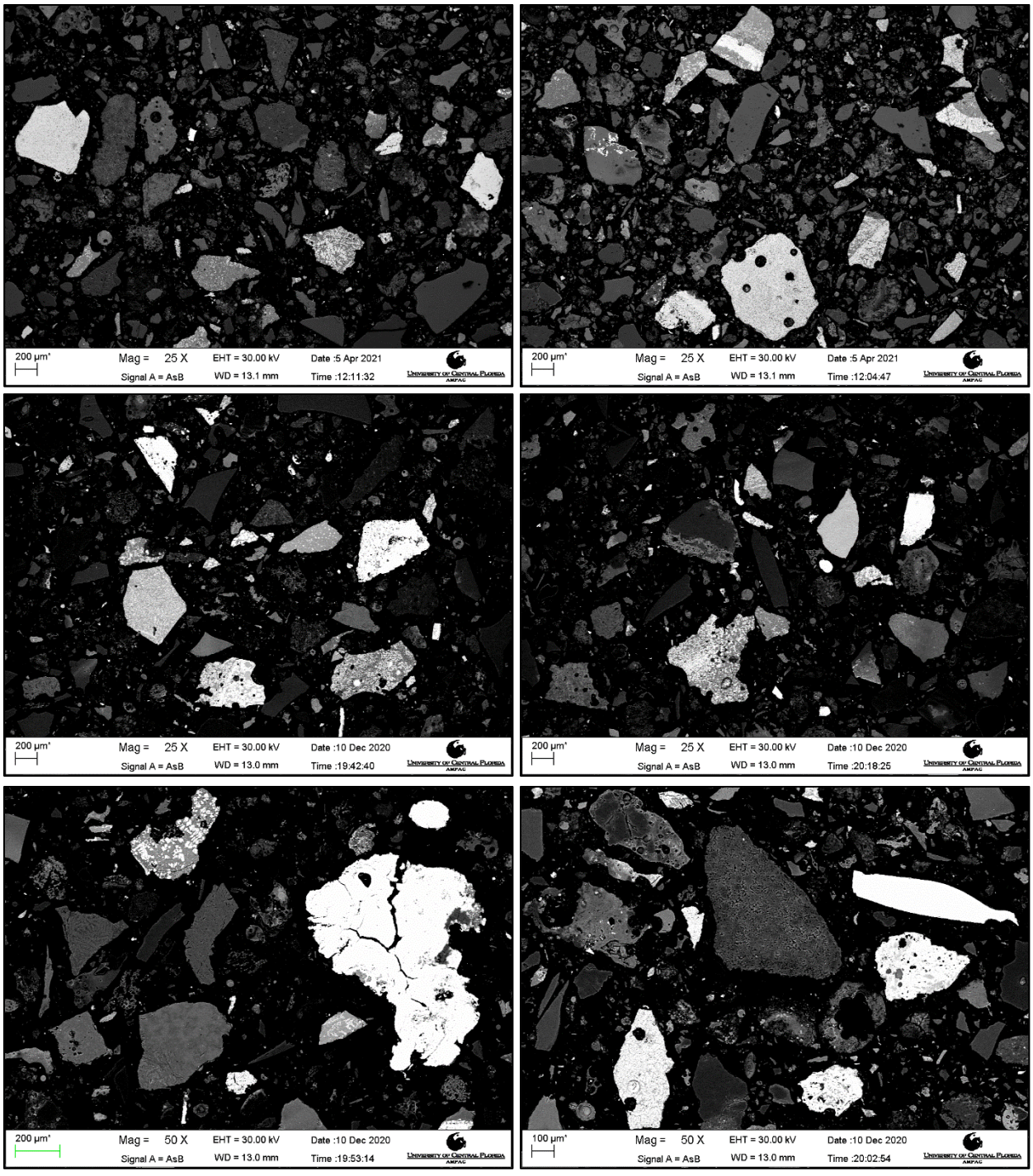

Figure A 12: Representative BSE Images of MSWIA-5

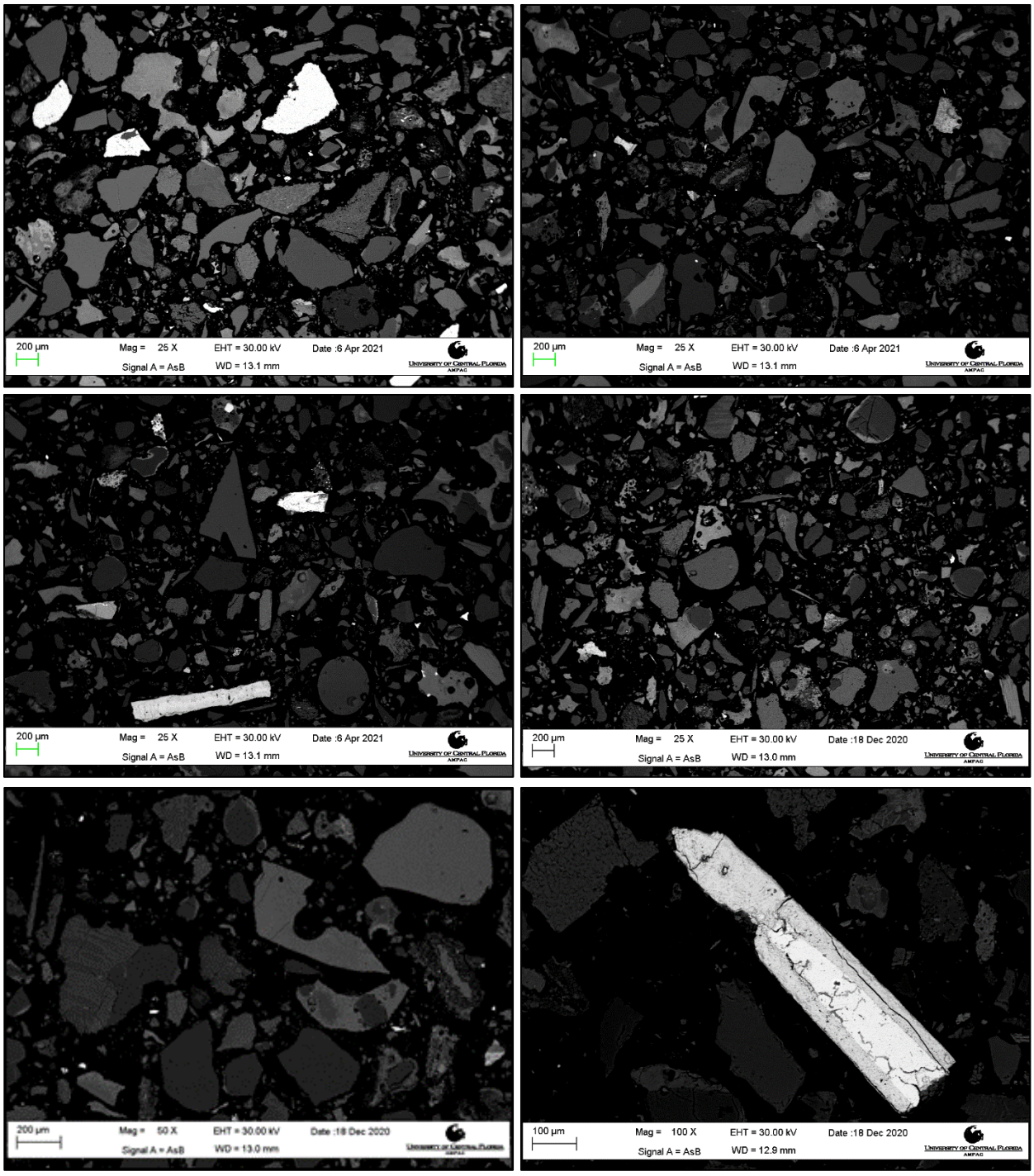

Figure A 13: Representative BSE Images of MSWIA-6

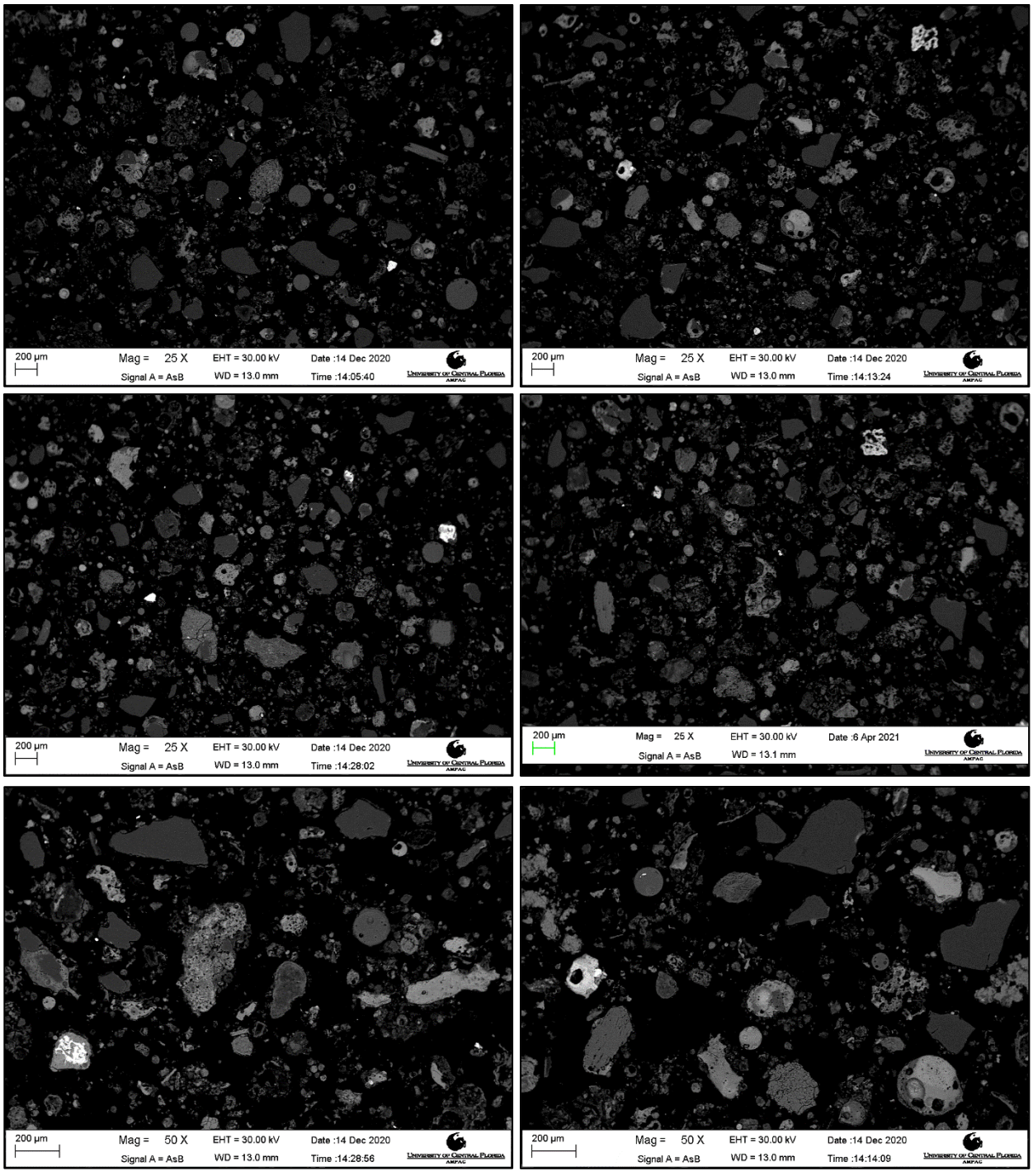

Figure A 14: Representative BSE Images of MSWIA-7

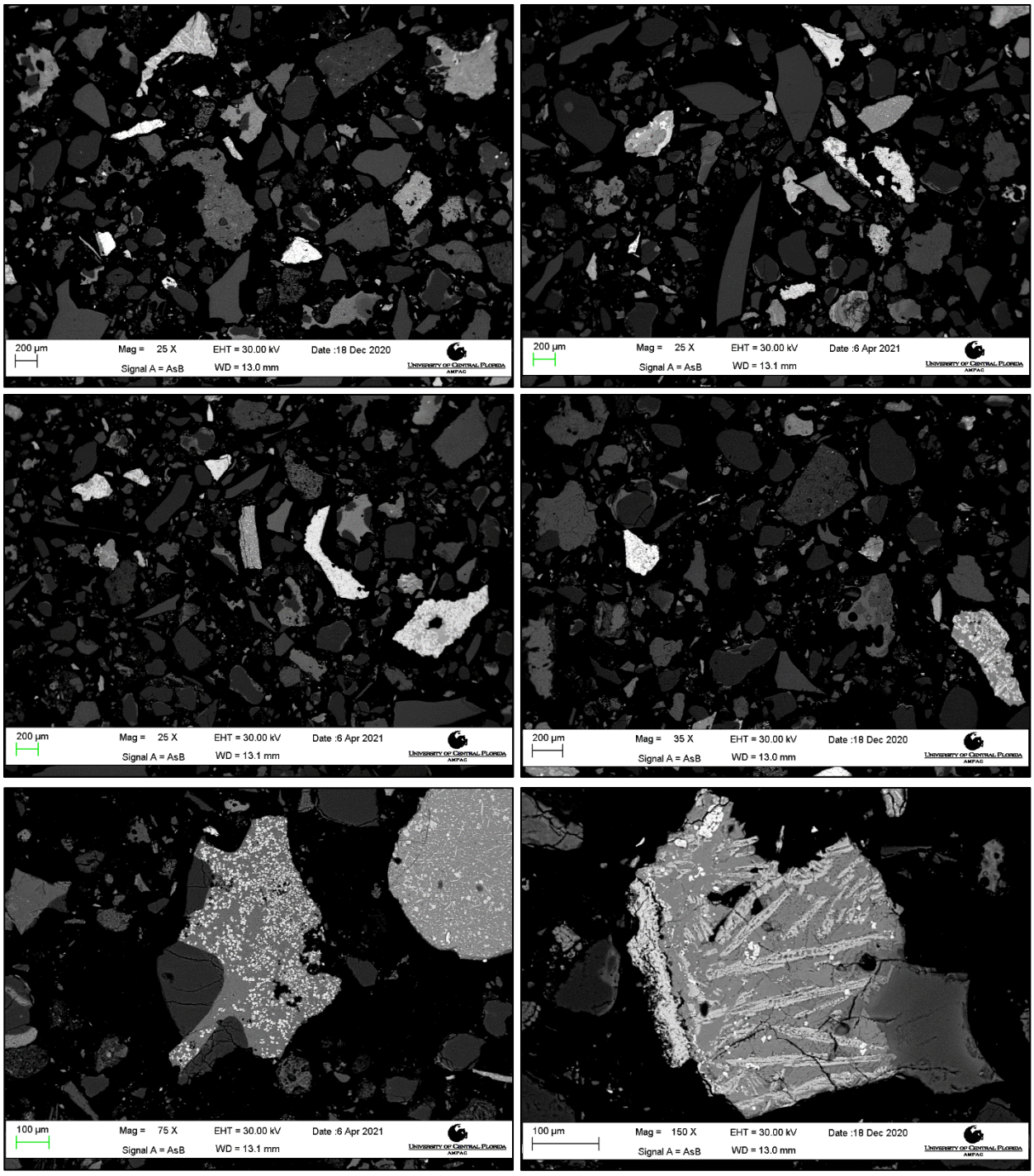

Figure A 15: Representative BSE Images of MSWIA-8

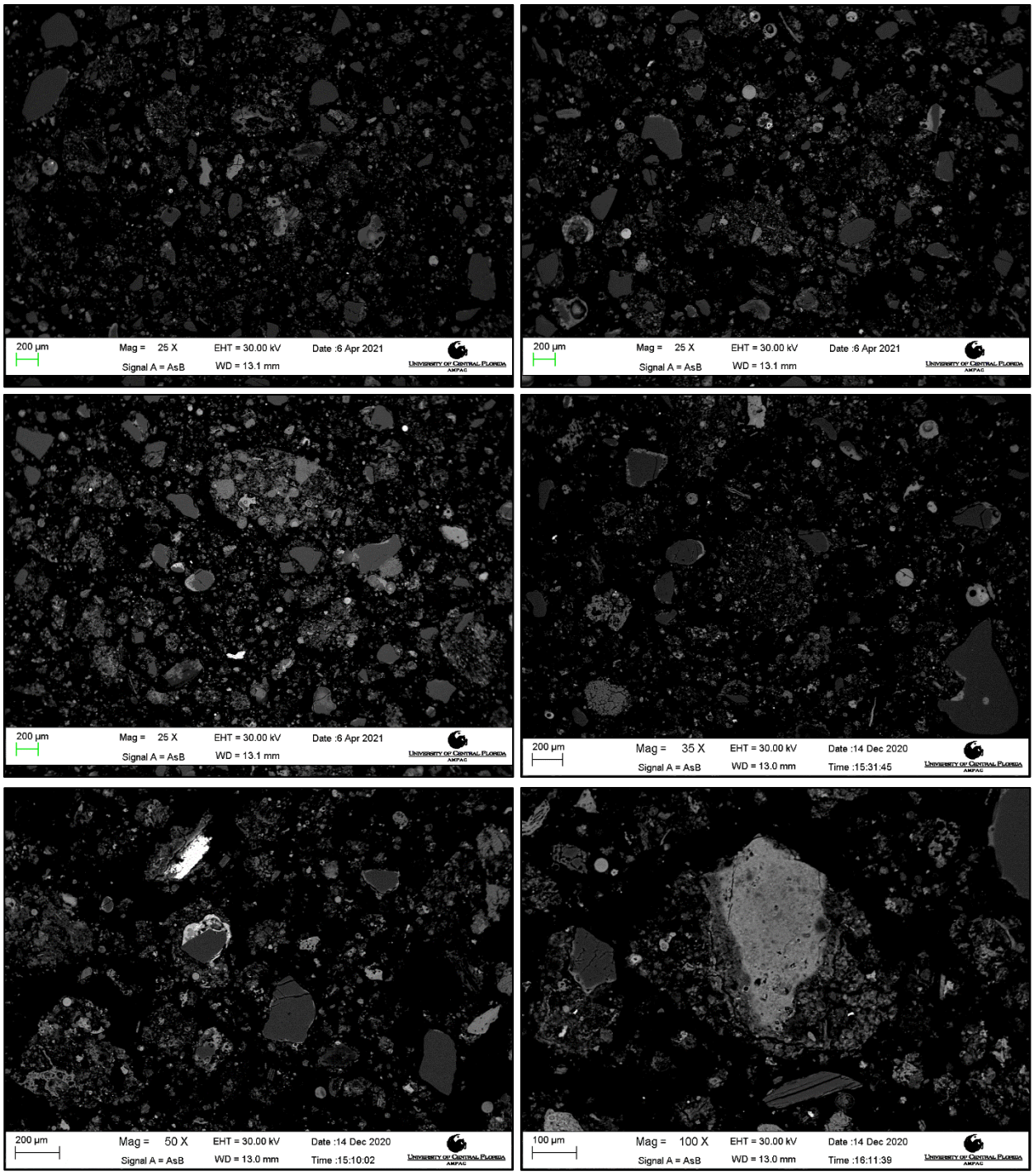

Figure A 16: Representative BSE Images of MSWIA-9

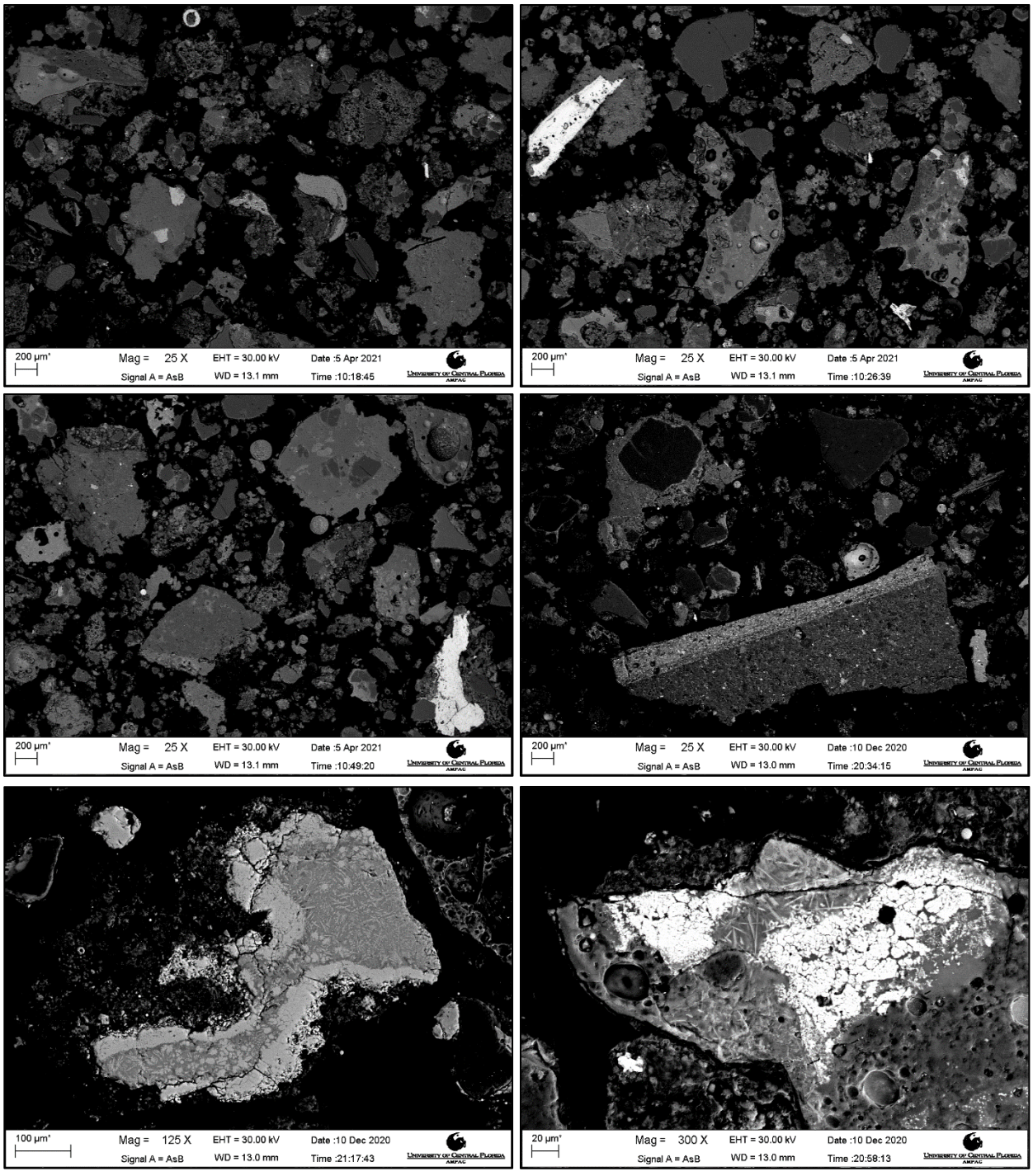

Figure A 17: Representative BSE Images of MSWIA-10

APPENDIX B: XRD PATTERNS WITH ASSOCIATED XRF DATA

Element	Percent Composition (%)
Ca	39.6
Si	23.2
Al	14.0
Fe	13.2
Ti	2.6
S	1.7
P	1.5
Ba	1.4
K	1.2
Sr	1.1
Cl	0.3

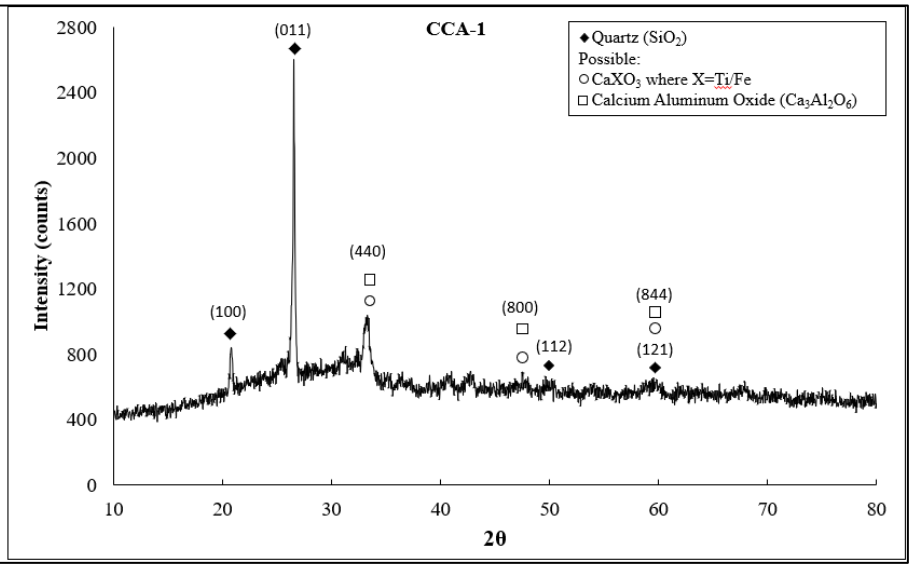

Figure B 1: XRD and XRF Data for CCA-1

Element	Percent Composition (%)
Ca	39.1
Si	22.5
Fe	15.3
Al	12.5
Ti	2.7
Ba	2.0
S	1.6
Sr	1.3
P	1.3
K	1.1
Cl	0.3

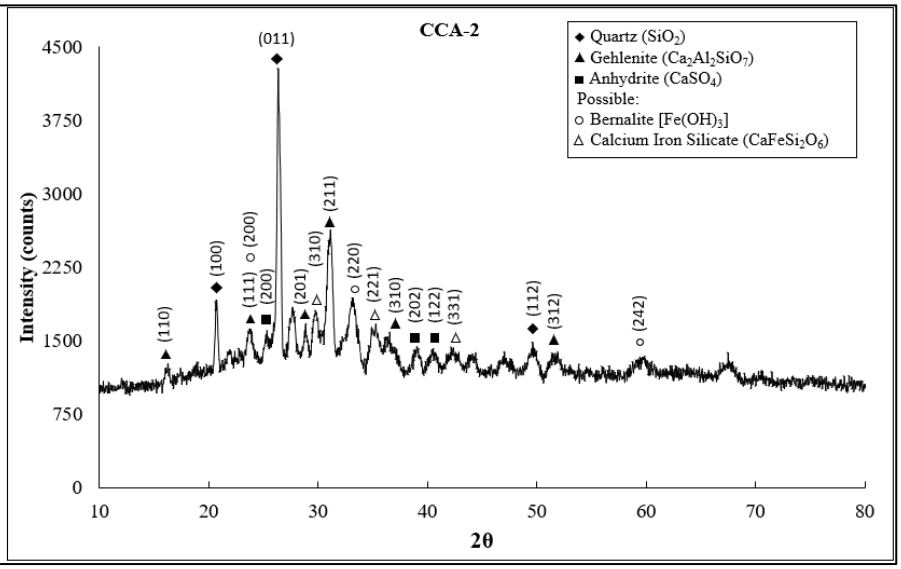

Figure B 2: XRD and XRF Data for CCA-2

Element	Percent Composition (%)
Ca	64.9
Cl	13.3
S	7.7
Fe	5.2
Si	4.2
Al	3.0
K	0.8
Ti	0.4
Br	0.2
Se	0.1

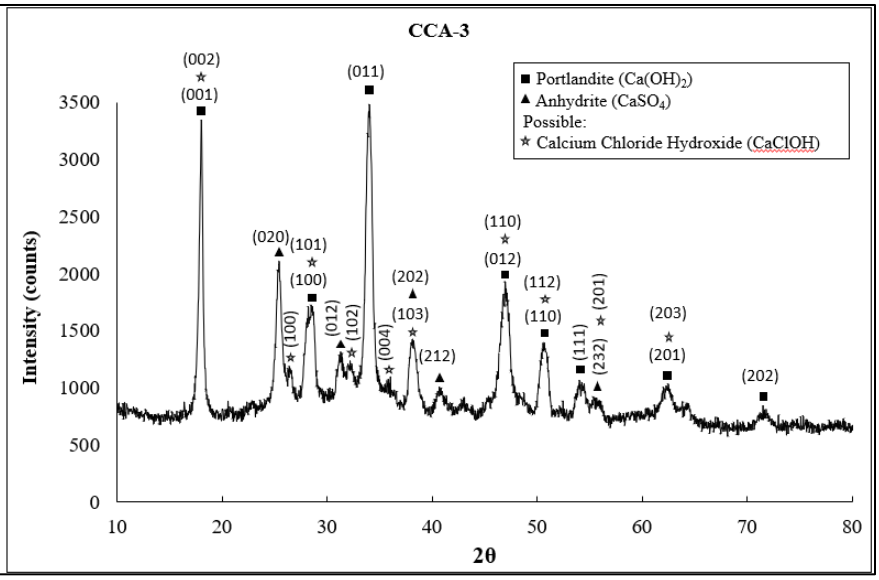

Figure B 3: XRD and XRF Data for CCA-3

Element	Percent Composition (%)
Ca	32.6
S	21.3
Si	17.5
Fe	10.8
Al	10.0
Ti	2.0
P	1.4
K	1.2
Sr	1.0
Ba	1.0

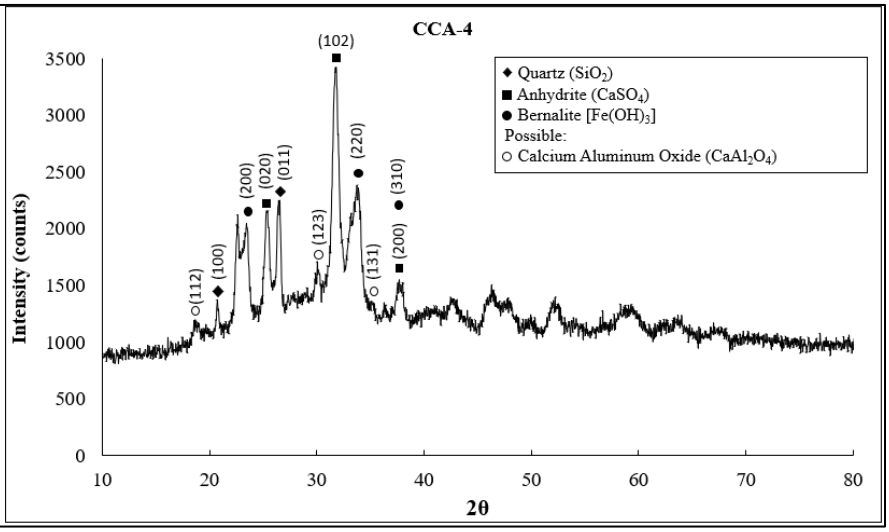

Figure B 4: XRD and XRF Data for CCA-4

Element	Percent Composition (%)
Ca	43.0
Si	23.8
Al	11.5
Fe	8.6
S	7.1
Ti	1.9
K	1.9
Sr	0.9
Mn	0.5
Cl	0.4
Ba	0.2

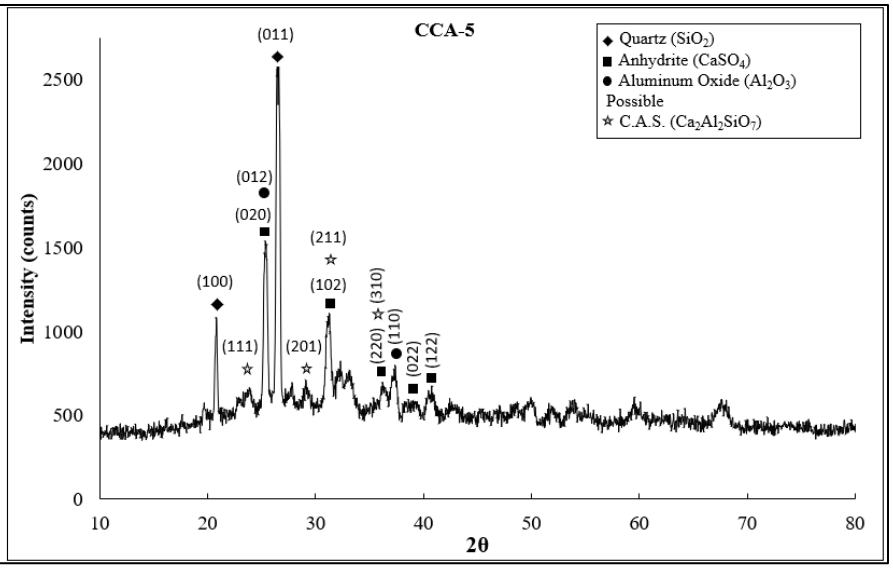

Figure B 5: XRD and XRF Data for CCA-5

Element	Percent Composition (%)
Ca	54.7
Si	13.0
Fe	10.0
Al	8.0
S	7.5
Ti	2.0
K	1.9
P	1.7
Sr	0.5
Cl	0.4
Ni	0.1

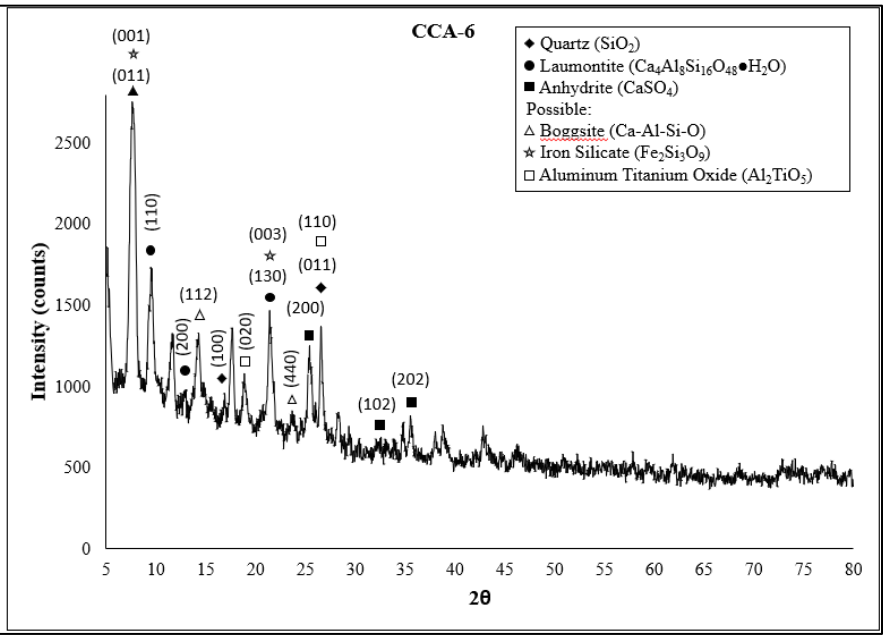

Figure B 6: XRD and XRF Data for CCA-6

Element	Percent Composition (%)
Ca	50.3
Cl	12.9
Si	12.9
Fe	8.7
Al	3.8
S	2.4
K	2.3
Zn	1.9
Ti	1.4
P	1.1
Cu	1.1

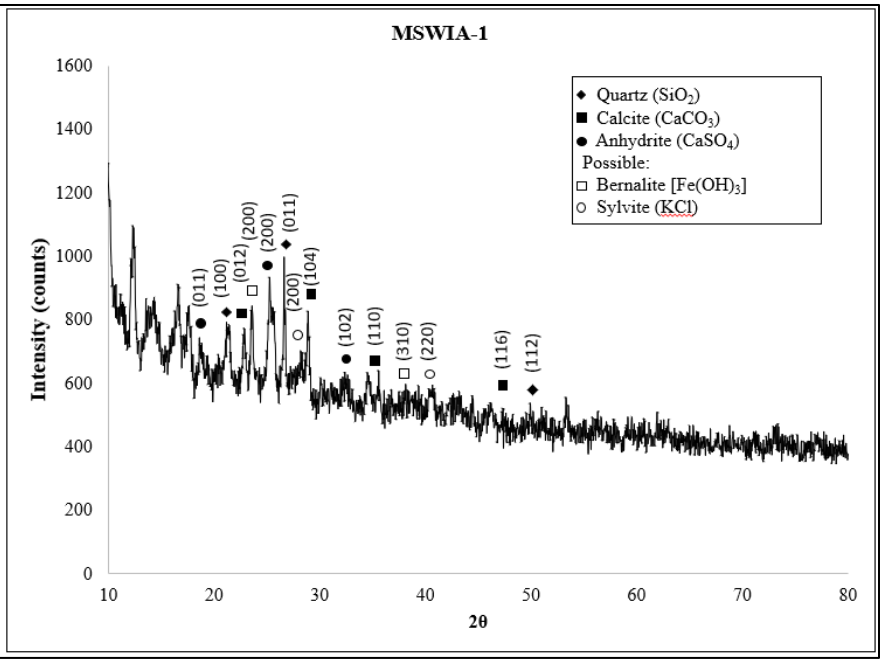

Figure B 7: XRD and XRF Data for MSWIA-1

Element	Percent Composition (%)
Ca	38.2
Cl	26.7
Si	11.2
Fe	8.6
S	4.0
Al	3.1
K	2.9
Zn	1.9
Ti	1.3
P	0.7
Cu	0.5

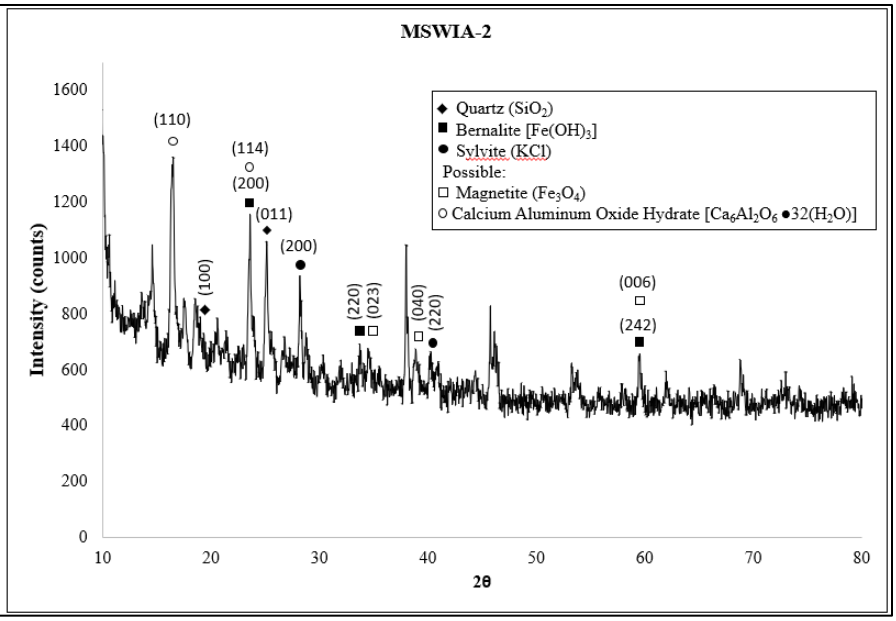

Figure B 8: XRD and XRF Data for MSWIA-2

Element	Percent Composition (%)
Ca	39.9
Cl	22.9
Si	11.4
Fe	10.1
Al	3.6
S	3.5
K	3.0
Zn	2.3
Ti	1.0
P	0.8

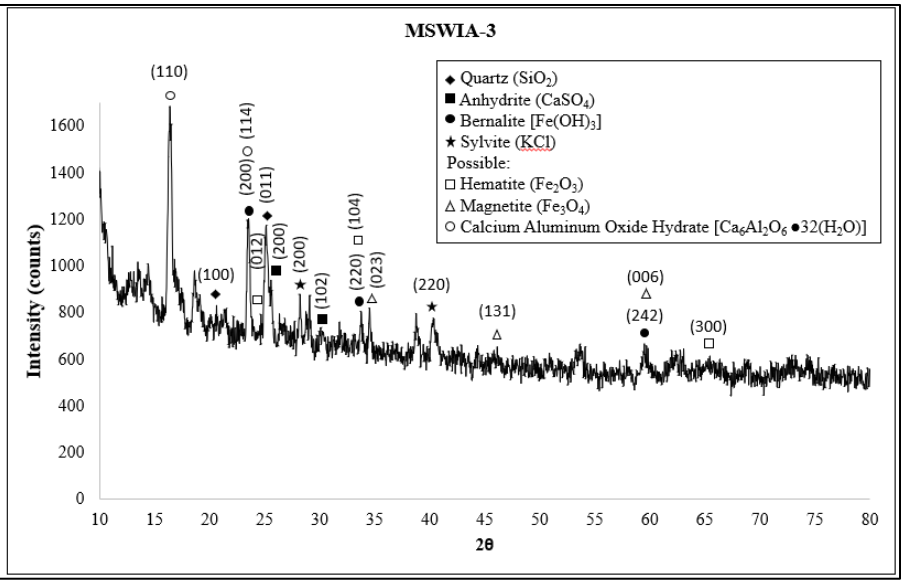

Figure B 9: XRD and XRF Data for MSWIA-3

Element	Percent Composition (%)
Ca	43.3
Si	14.9
Cl	14.3
Fe	8.6
Al	4.3
S	4.3
K	3.3
Ti	2.6
Zn	1.8
P	0.9
Cu	0.4

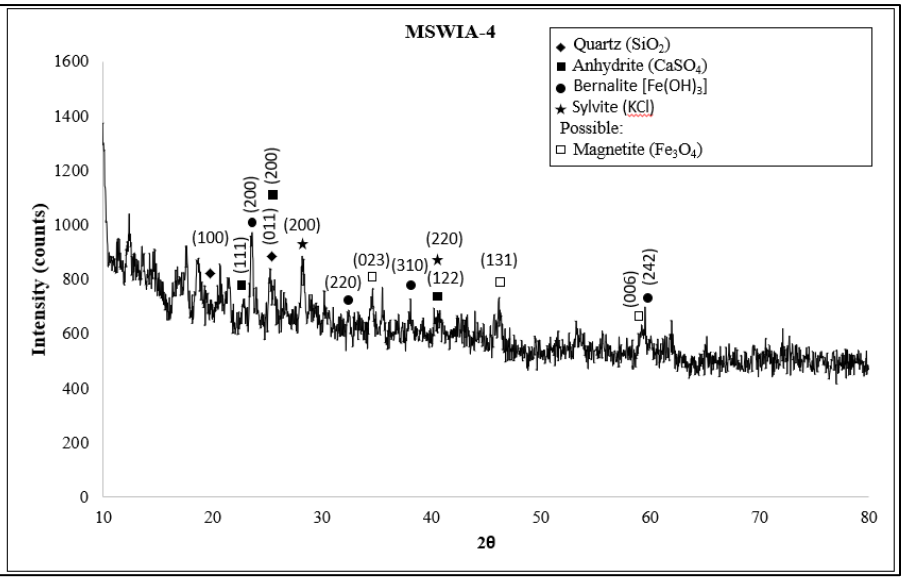

Figure B 10: XRD and XRF Data for MSWIA-4

Element	Percent Composition (%)
Ca	45.9
Cl	14.5
Si	11.8
Fe	9.1
Al	4.8
S	4.7
K	2.8
Zn	1.9
Ti	1.8
P	1.0
Cu	0.6

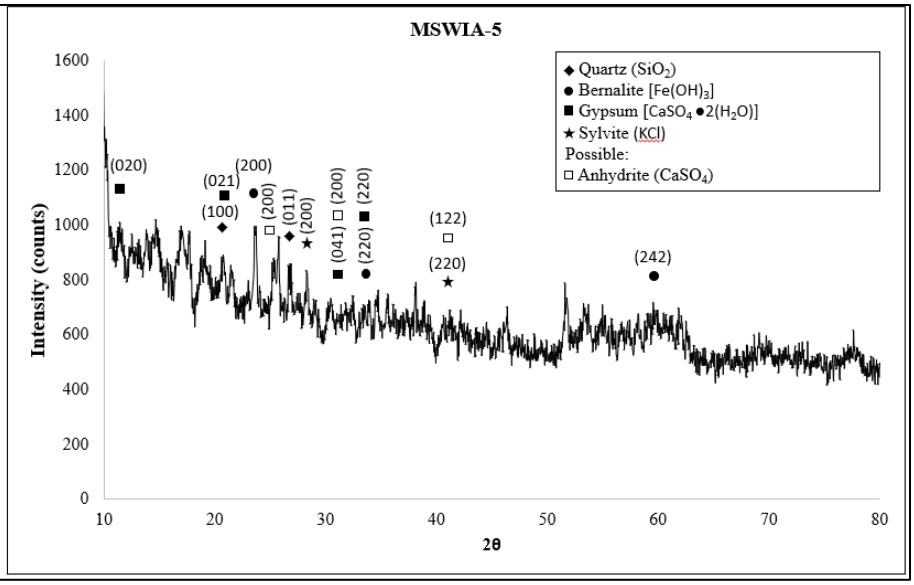

Figure B 11: XRD and XRF Data for MSWIA-5

Element	Percent Composition (%)
Ca	65.5
Si	13.7
Al	4.4
Fe	3.6
Cl	2.9
S	2.6
Ti	2.5
K	1.2
P	1.1
Cu	0.9
Zn	0.6

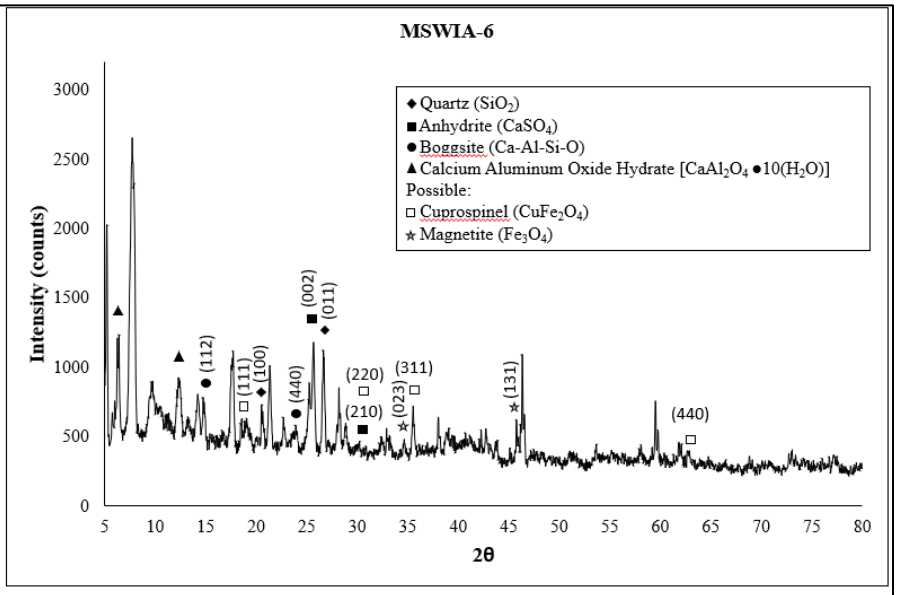

Figure B 12: XRD and XRF Data for MSWIA-6

Note: No miller indices listed for *Calcium Aluminum Oxide Hydrate* because no values were listed in the ICDD reference file.

Element	Percent Composition (%)
Ca	61.5
Cl	22.2
K	3.2
S	3.1
Si	2.9
Fe	1.5
Al	1.5
Ti	1.4
Zn	1.3
Br	0.5

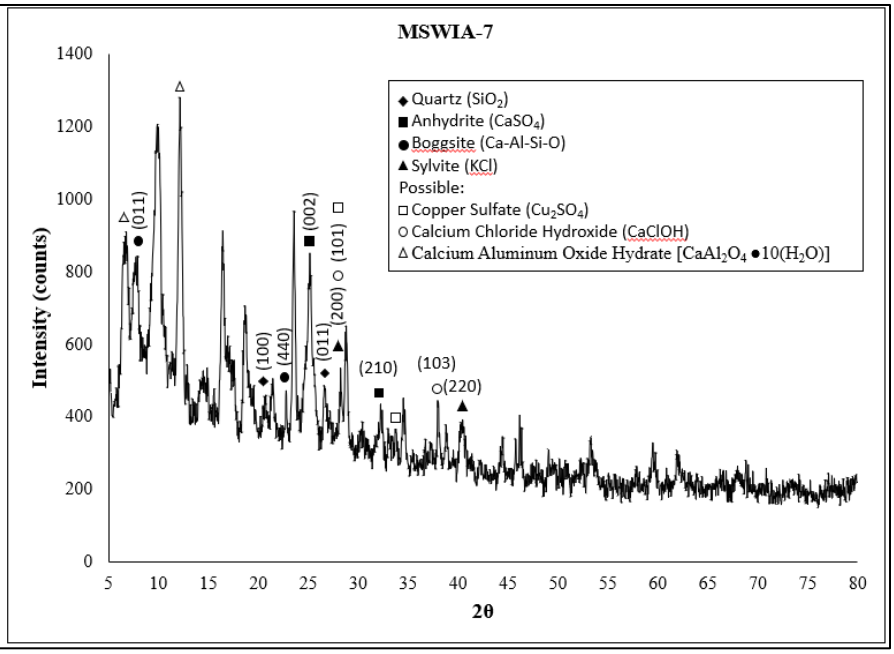

Figure B 13: XRD and XRF Data for MSWIA-7

Note: No miller indices listed for *Copper Sulfate* or *Calcium Aluminum Oxide Hydrate* because no values were listed in the ICDD reference file.

Element	Percent Composition (%)
Ca	56.6
Si	17.2
Fe	12.7
S	4.5
K	2.4
Cl	1.7
Al	1.7
Zn	1.1
Ti	0.9
Cu	0.8

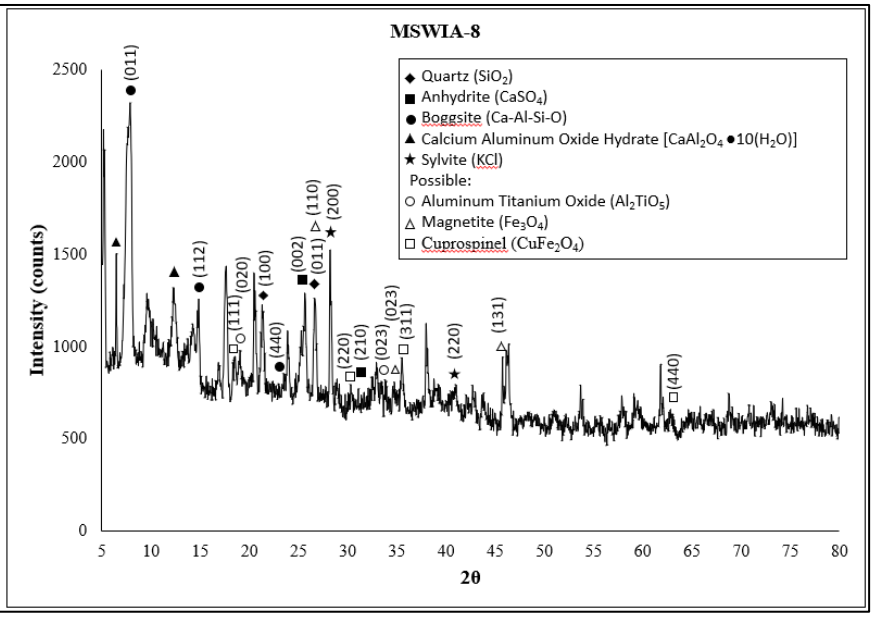

Figure B 14: XRD and XRF Data for MSWIA-8

Note: No miller indices listed for *Calcium Aluminum Oxide Hydrate* because no values were listed in the ICDD reference file.

Element	Percent Composition (%)
Ca	61.5
Cl	22.2
K	3.2
S	3.1
Si	2.9
Fe	1.5
Al	1.5
Ti	1.4
Zn	1.3
Br	0.5

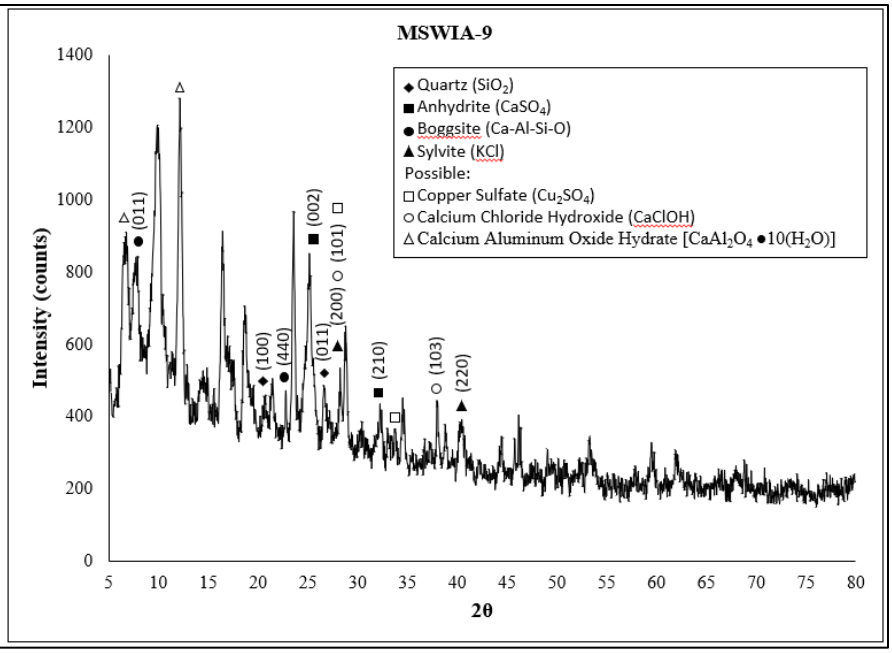

Figure B 15: XRD and XRF Data for MSWIA-9

Note: No miller indices listed for *Copper Sulfate* or *Calcium Aluminum Oxide Hydrate* because no values were listed in the ICDD reference file.

Element	Percent Composition (%)
Ca	55.5
Cl	20.5
Si	5.7
S	4.7
K	2.8
Zn	2.8
Fe	2.6
Al	1.8
Ti	1.2
P	0.7

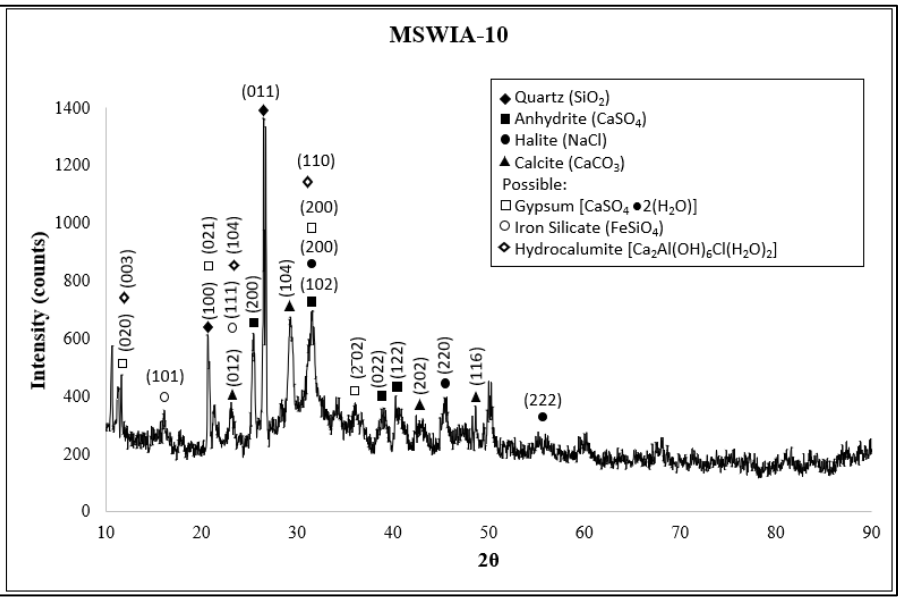

Figure B 16: XRD and XRF Data for MSWIA-10

APPENDIX C: XEDS SPECTRAL MAPS

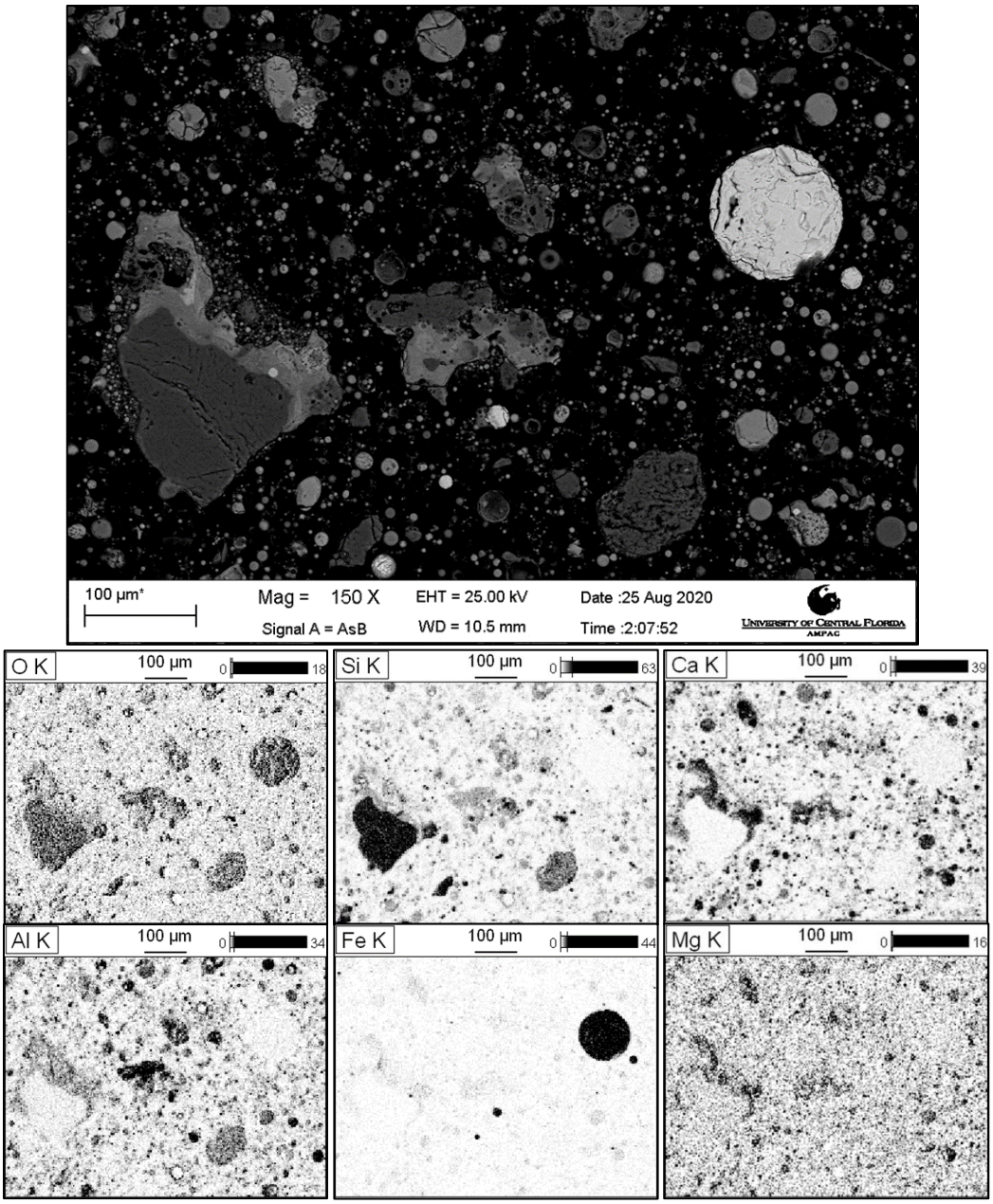

Figure C 1: XEDS Spectral Map Data for CCA-1

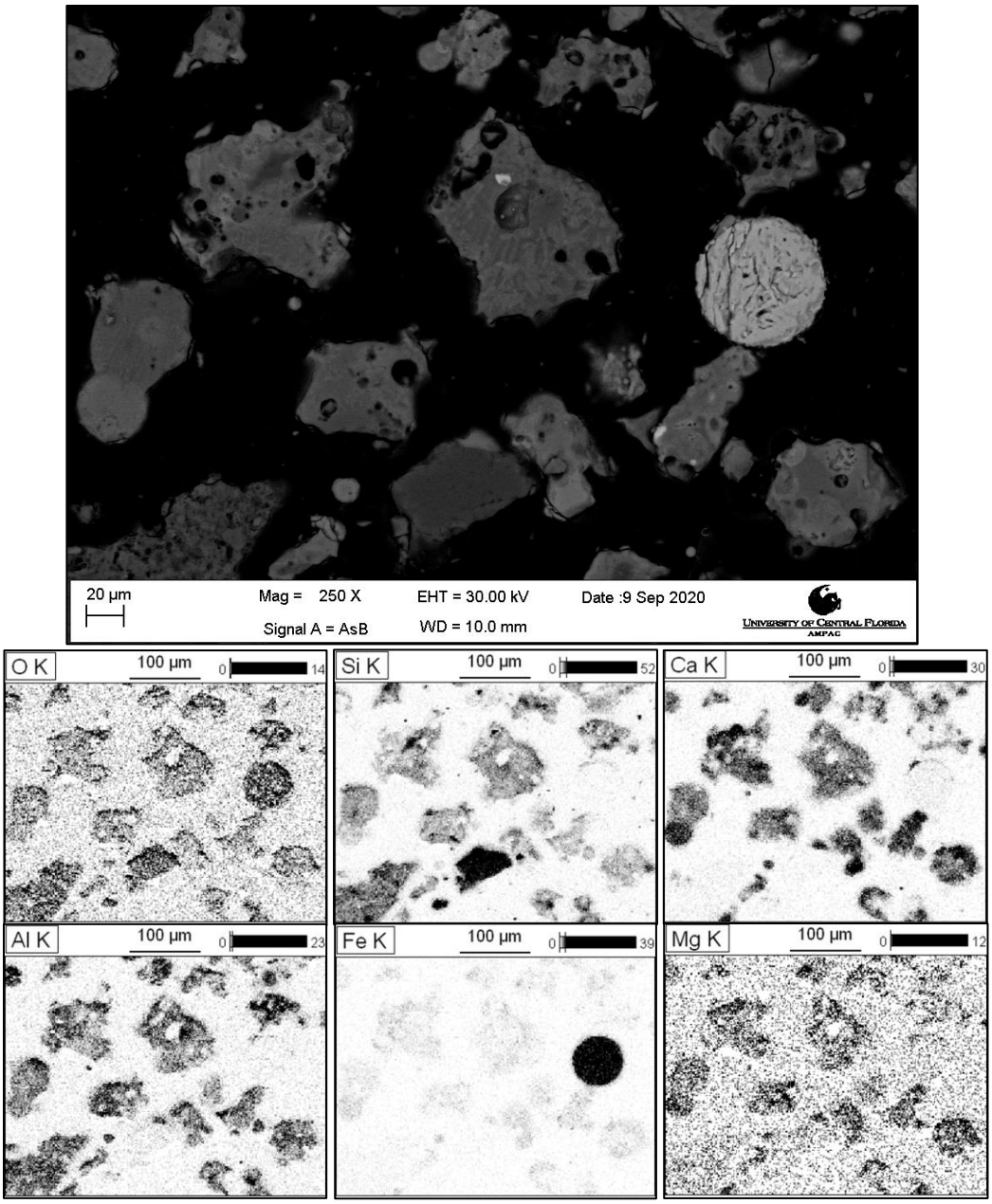

Figure C 2: XEDS Spectral Map Data for CCA-2

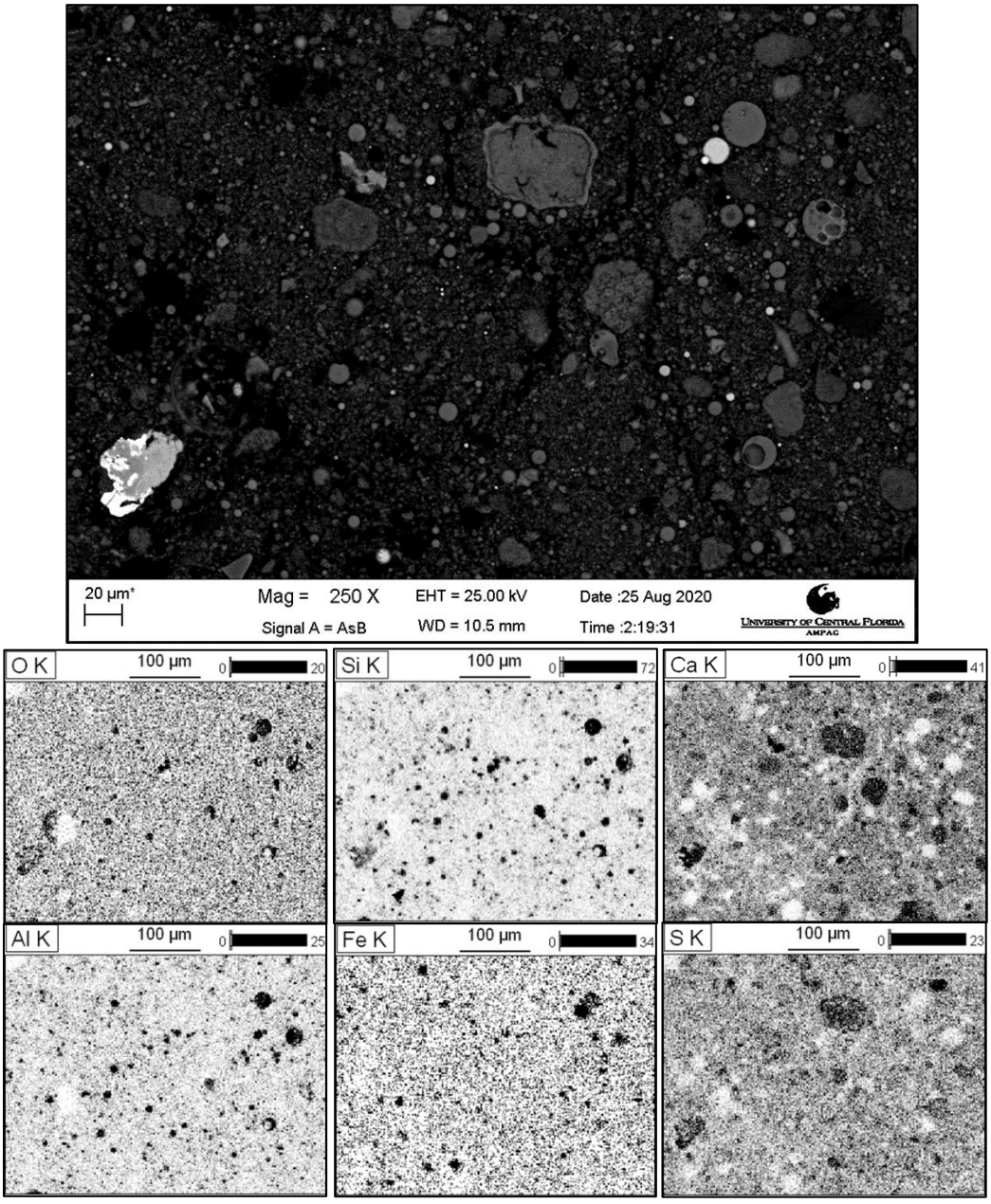

Figure C 3: XEDS Spectral Map Data for CCA-3

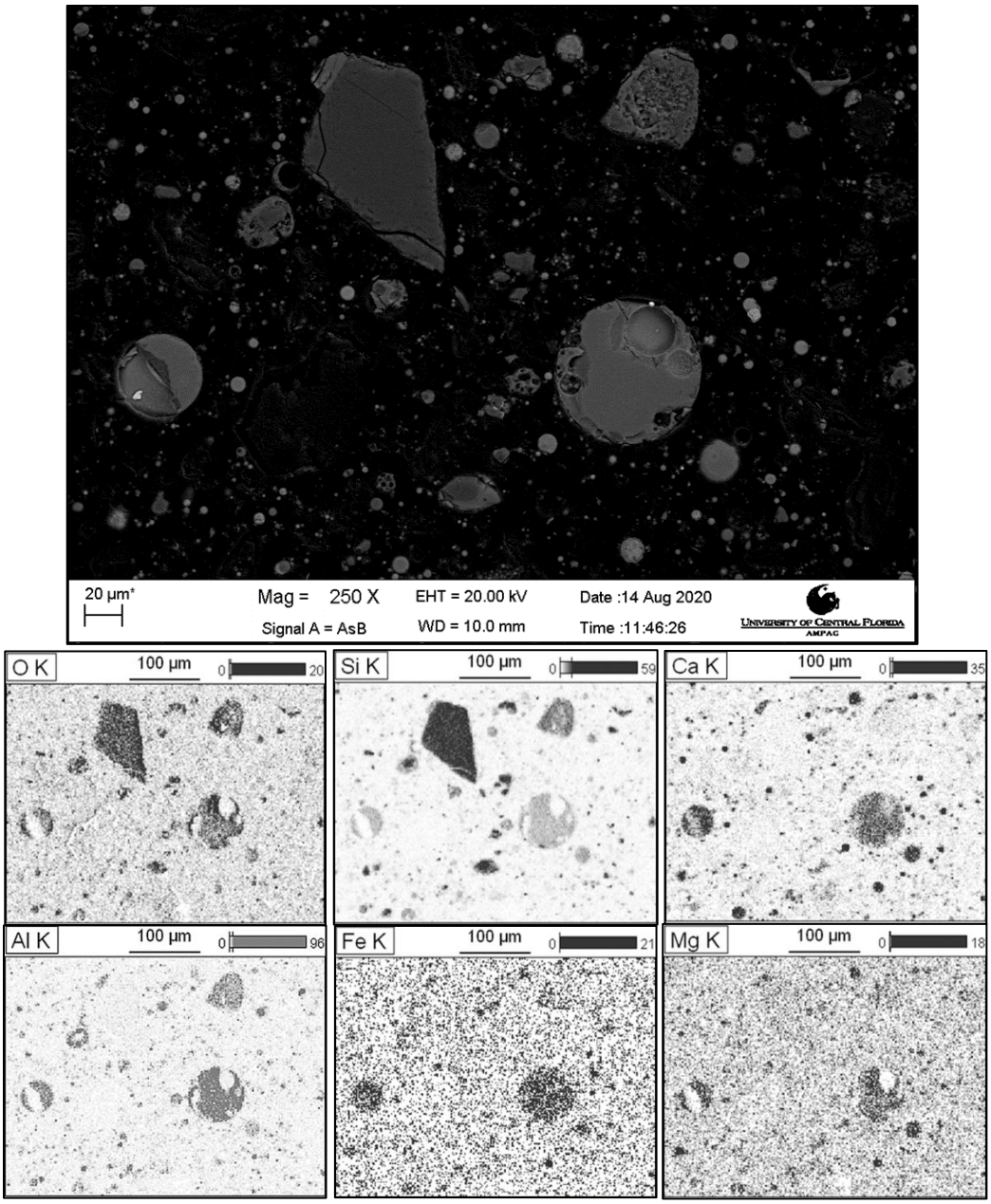

Figure C 4: XEDS Spectral Map Data for CCA-4

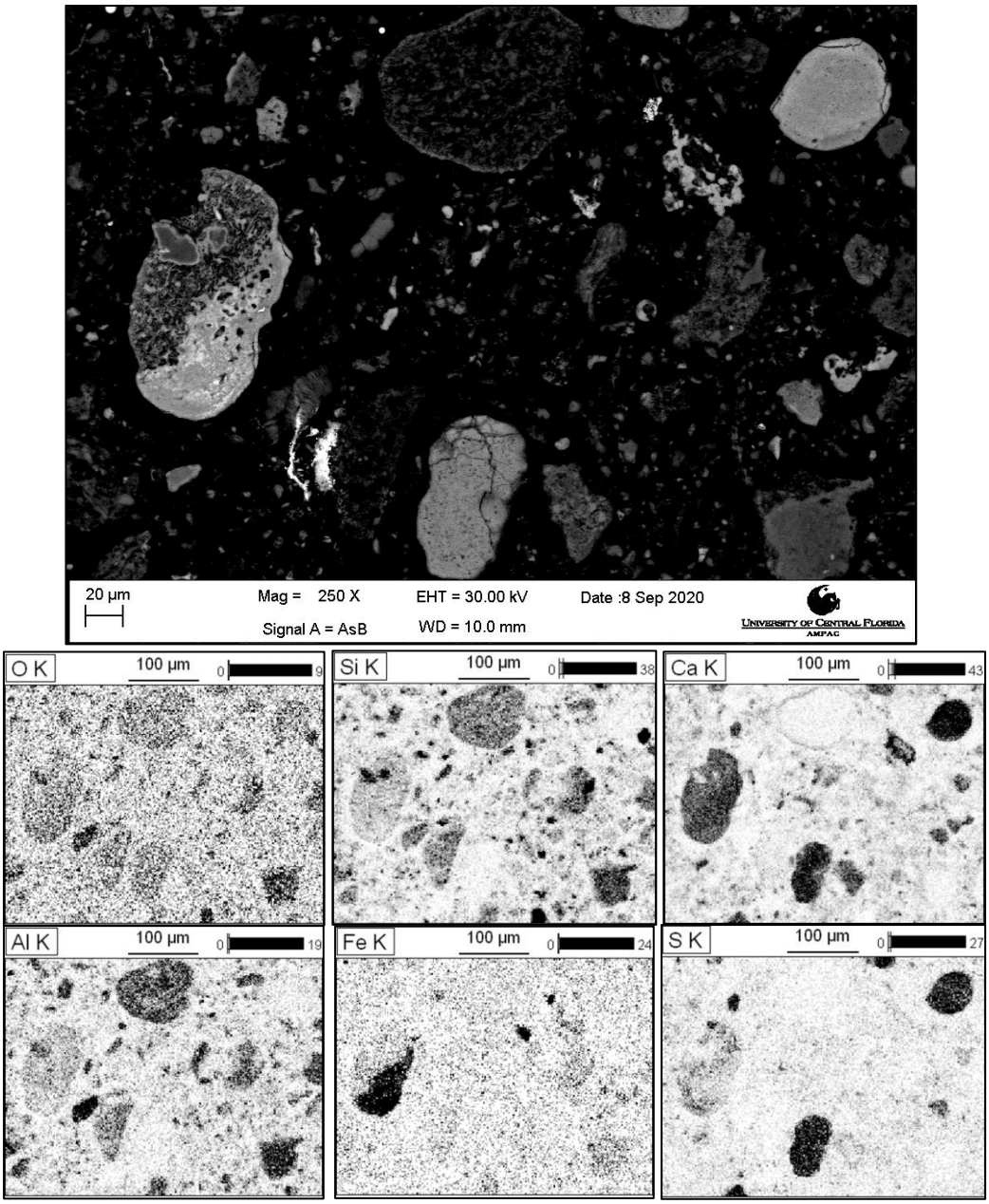

Figure C 5: XEDS Spectral Map Data for CCA-5

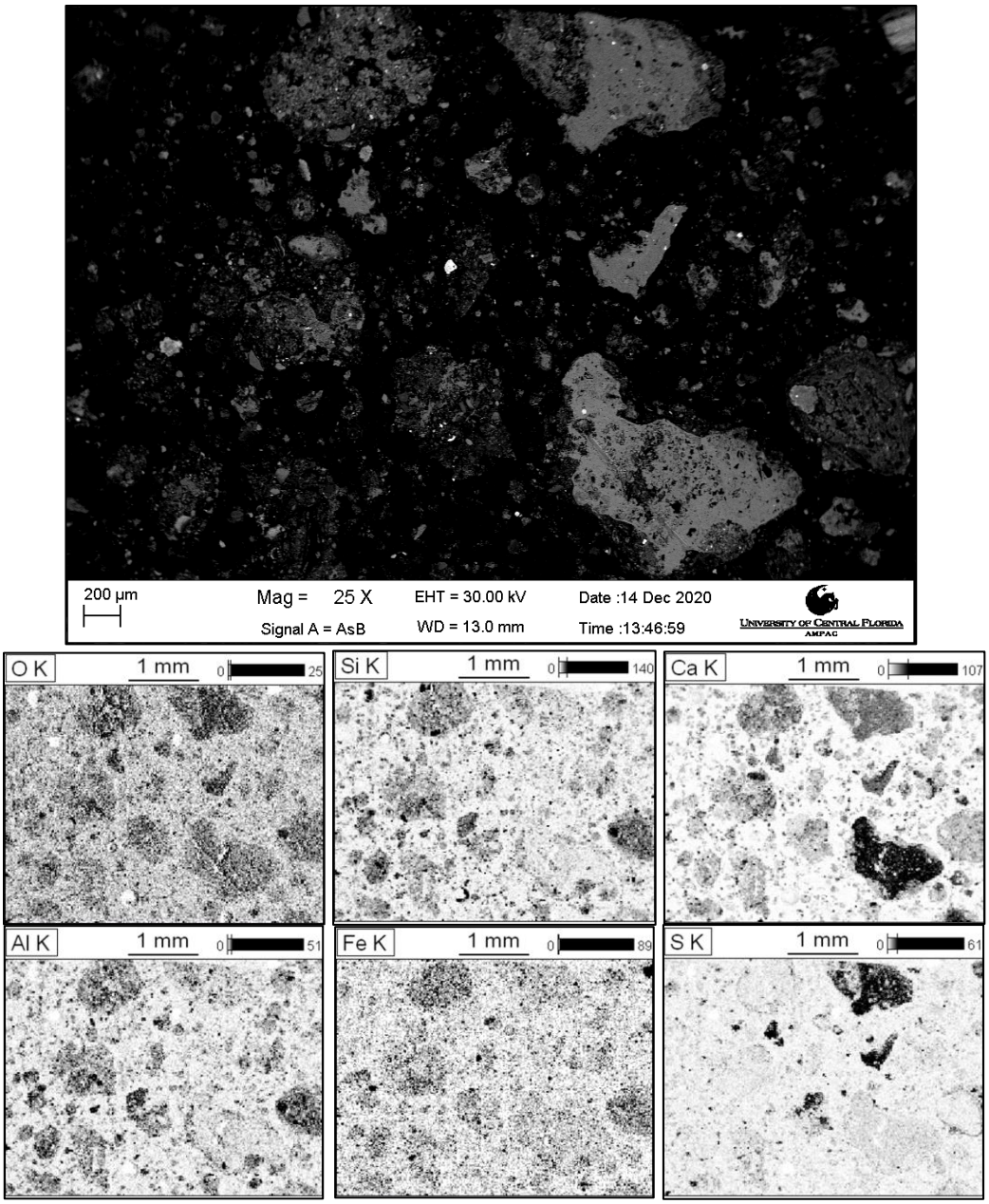

Figure C 6: XEDS Spectral Map Data for CCA-6

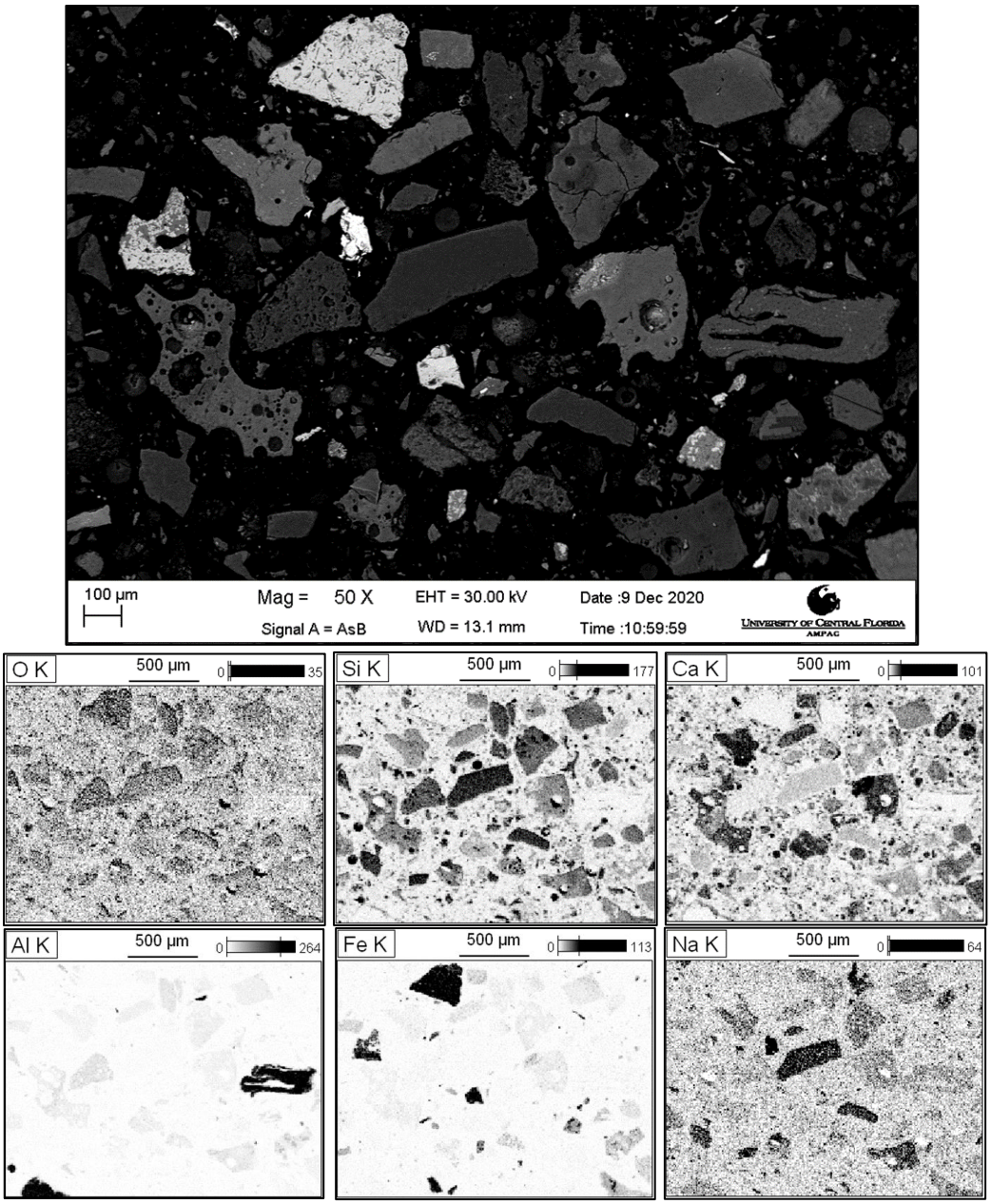

Figure C 7: XEDS Spectral Map Data for MSWIA-1

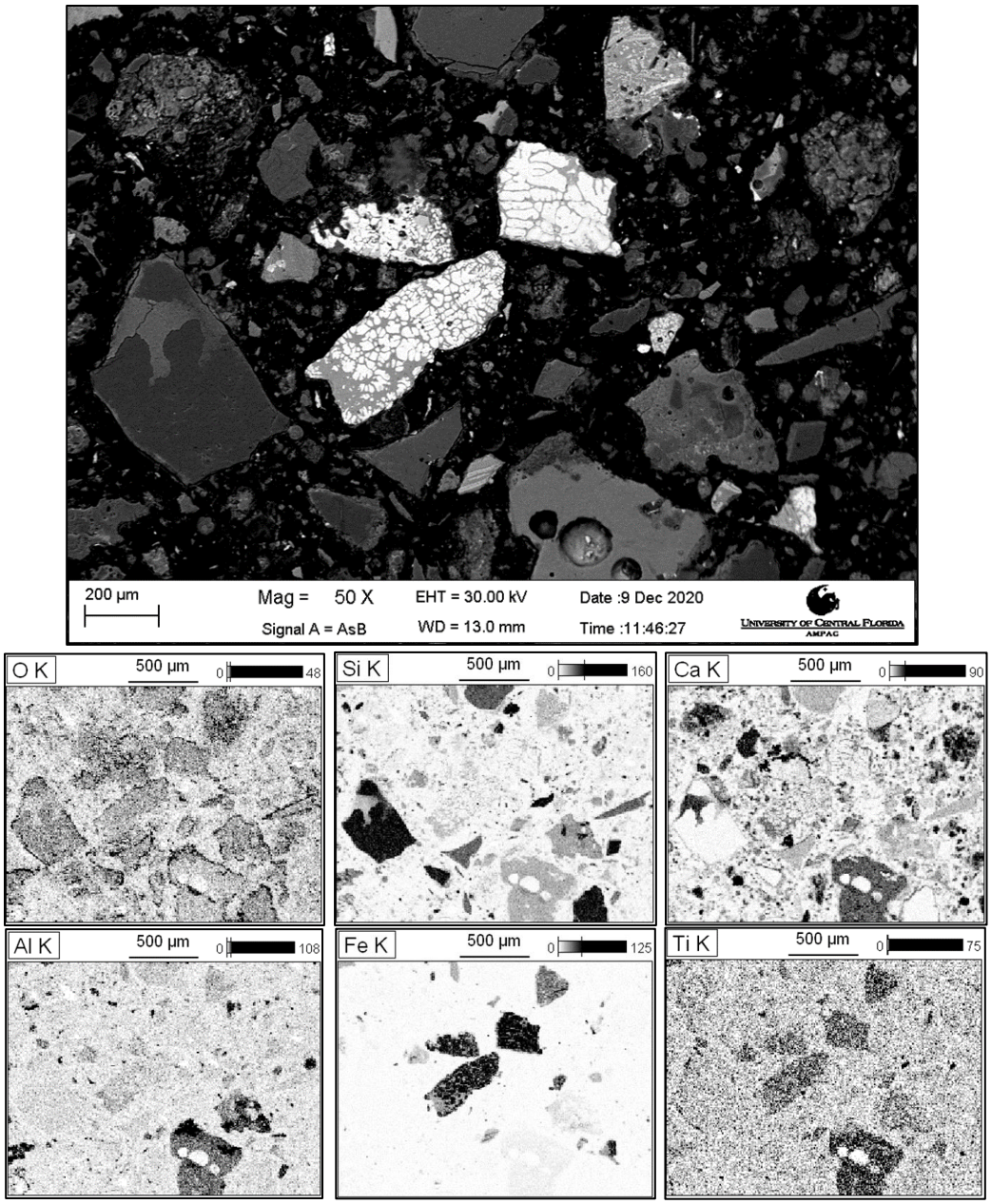

Figure C 8: XEDS Spectral Map Data for MSWIA-2

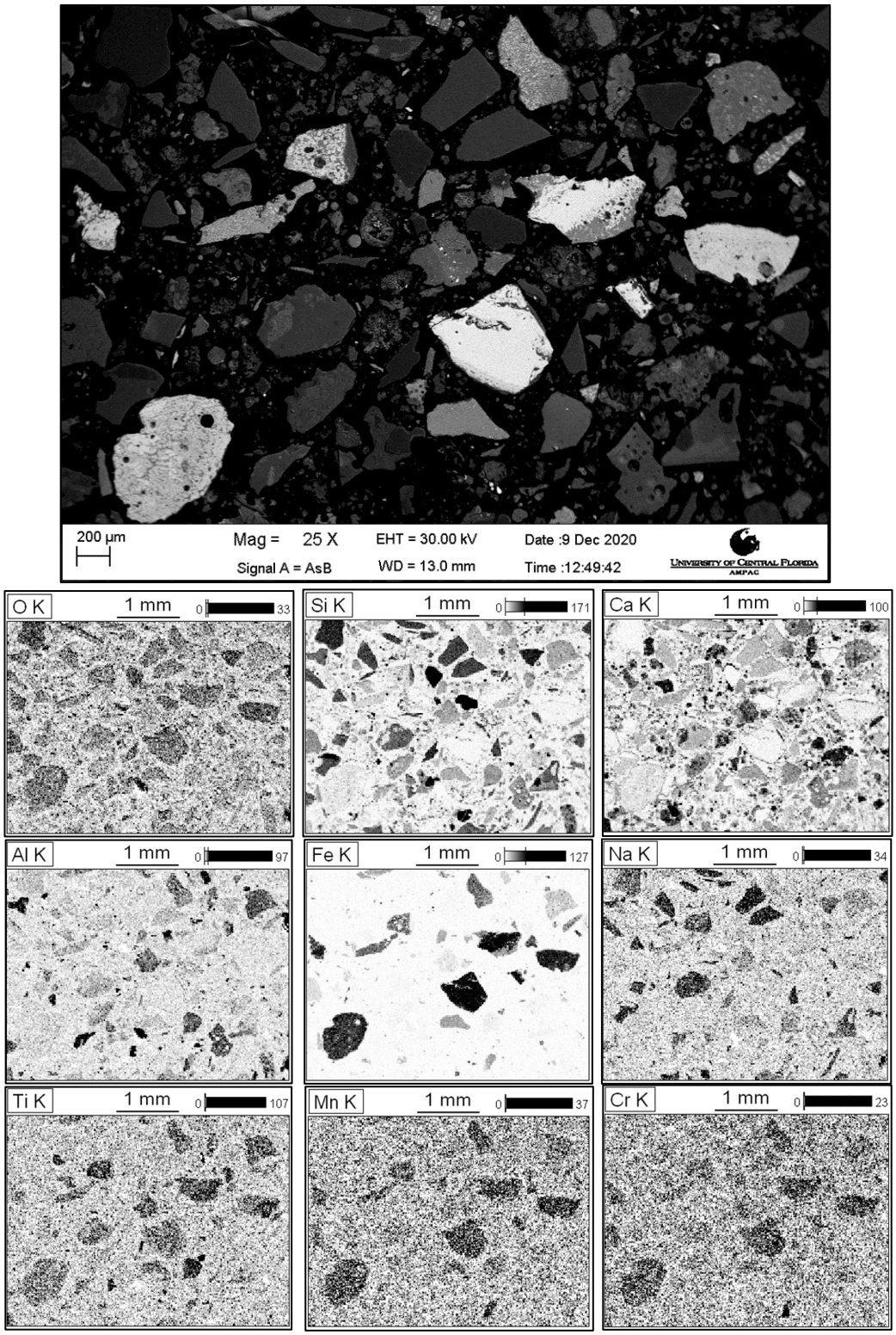

Figure C 9: XEDS Spectral Map Data for MSWIA-3

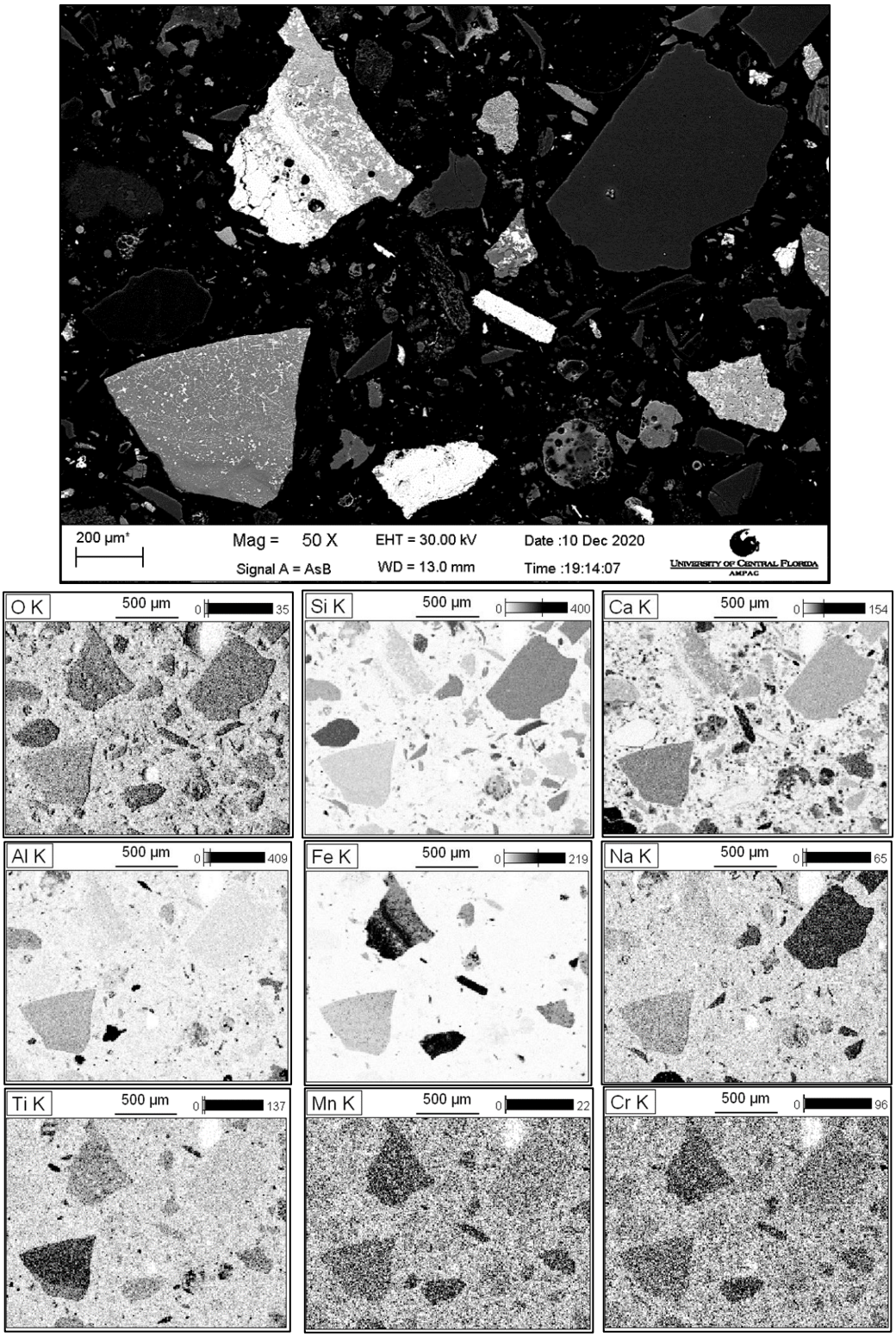

Figure C 10: XEDS Spectral Map Data for MSWIA-4

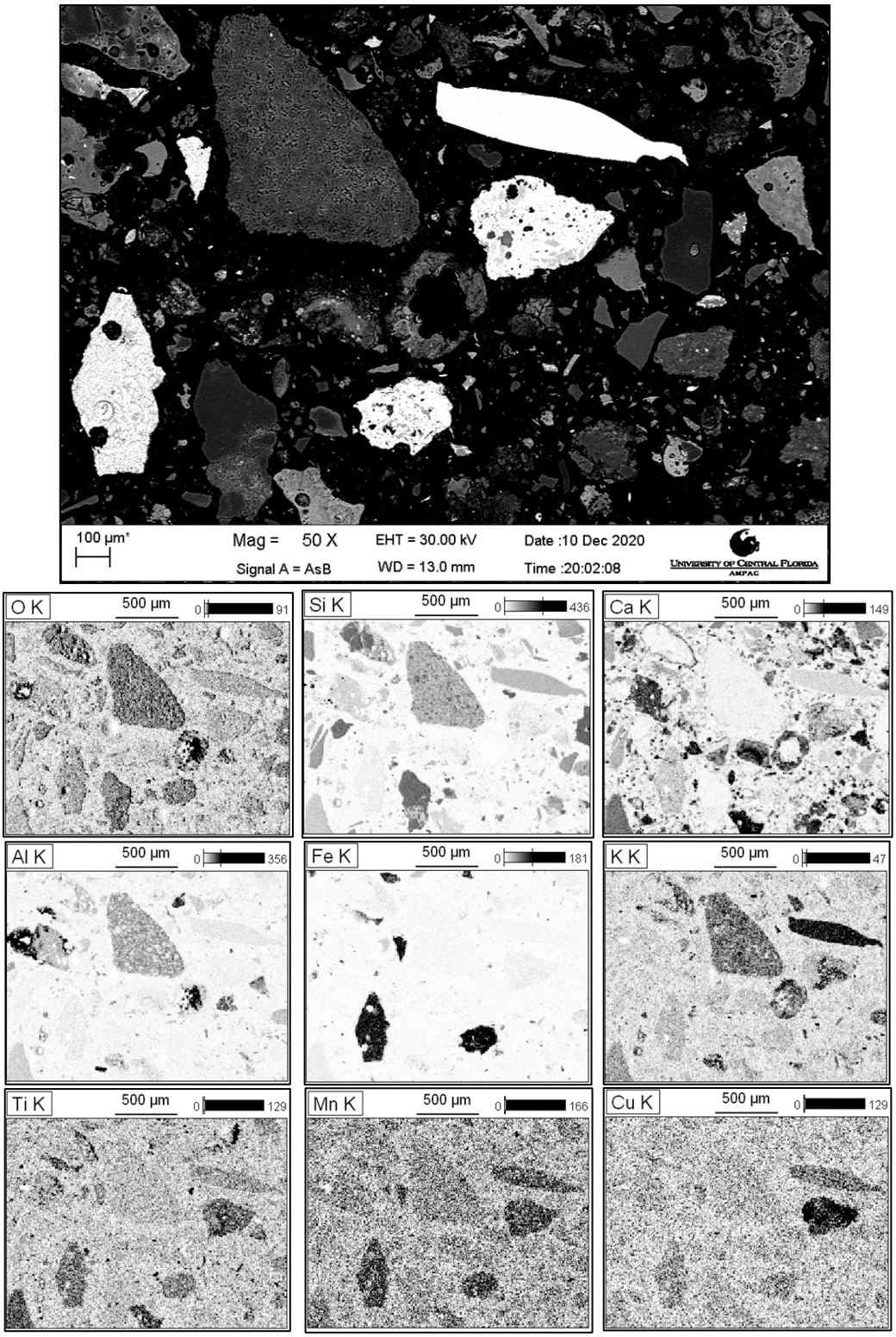

Figure C 11: XEDS Spectral Map Data for MSWIA-5

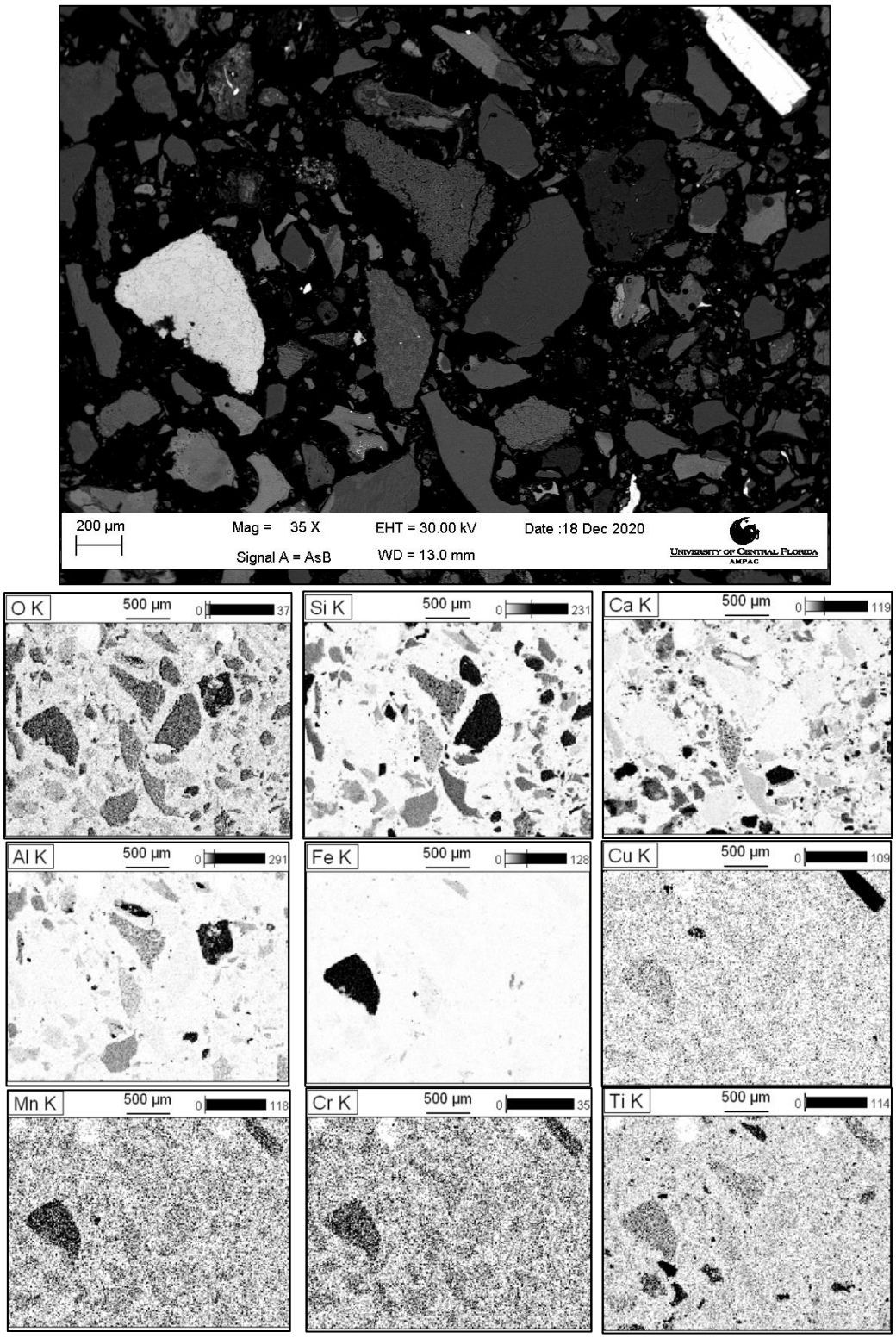

Figure C 12: XEDS Spectral Map Data for MSWIA-6

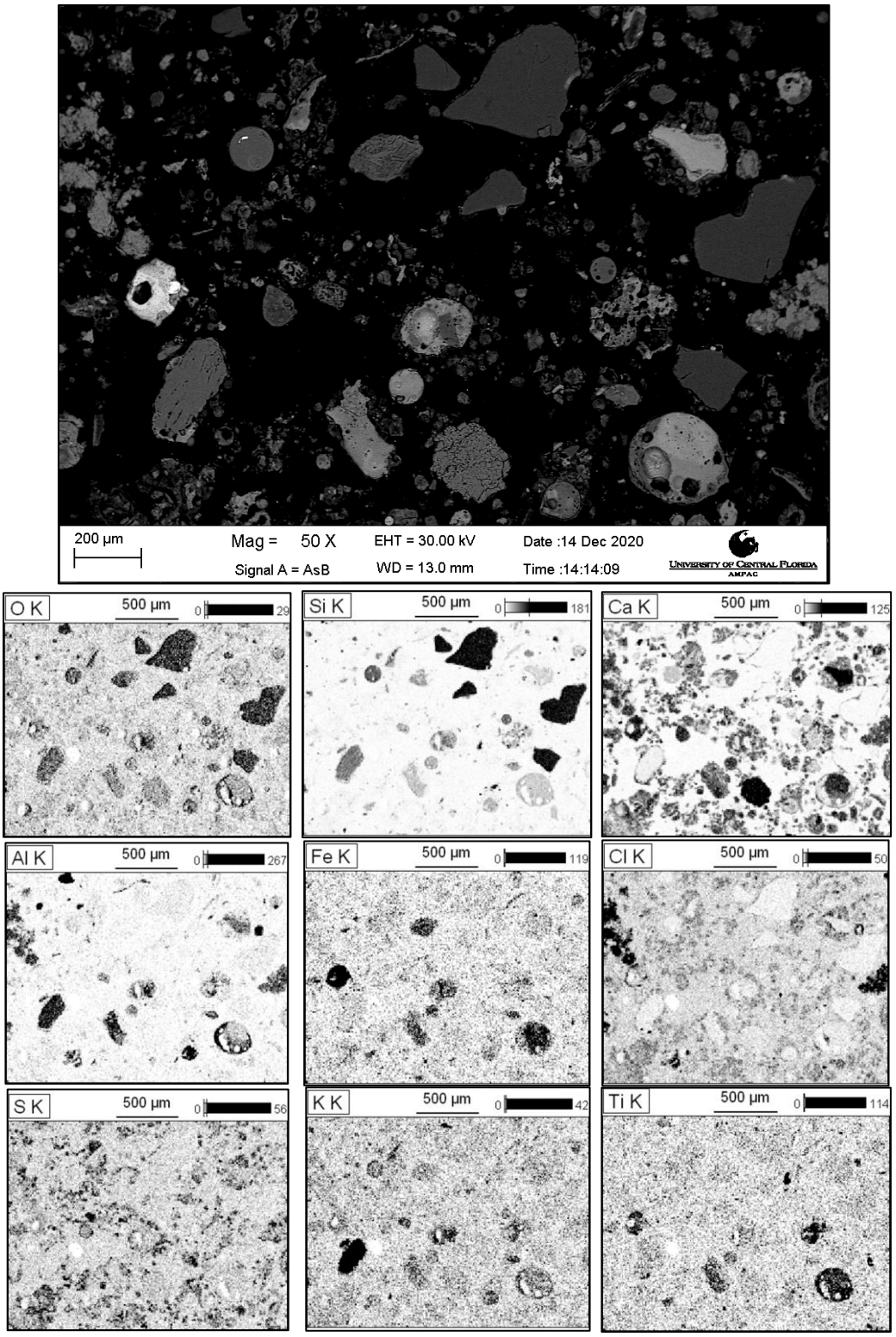

Figure C 13: XEDS Spectral Map Data for MSWIA-7

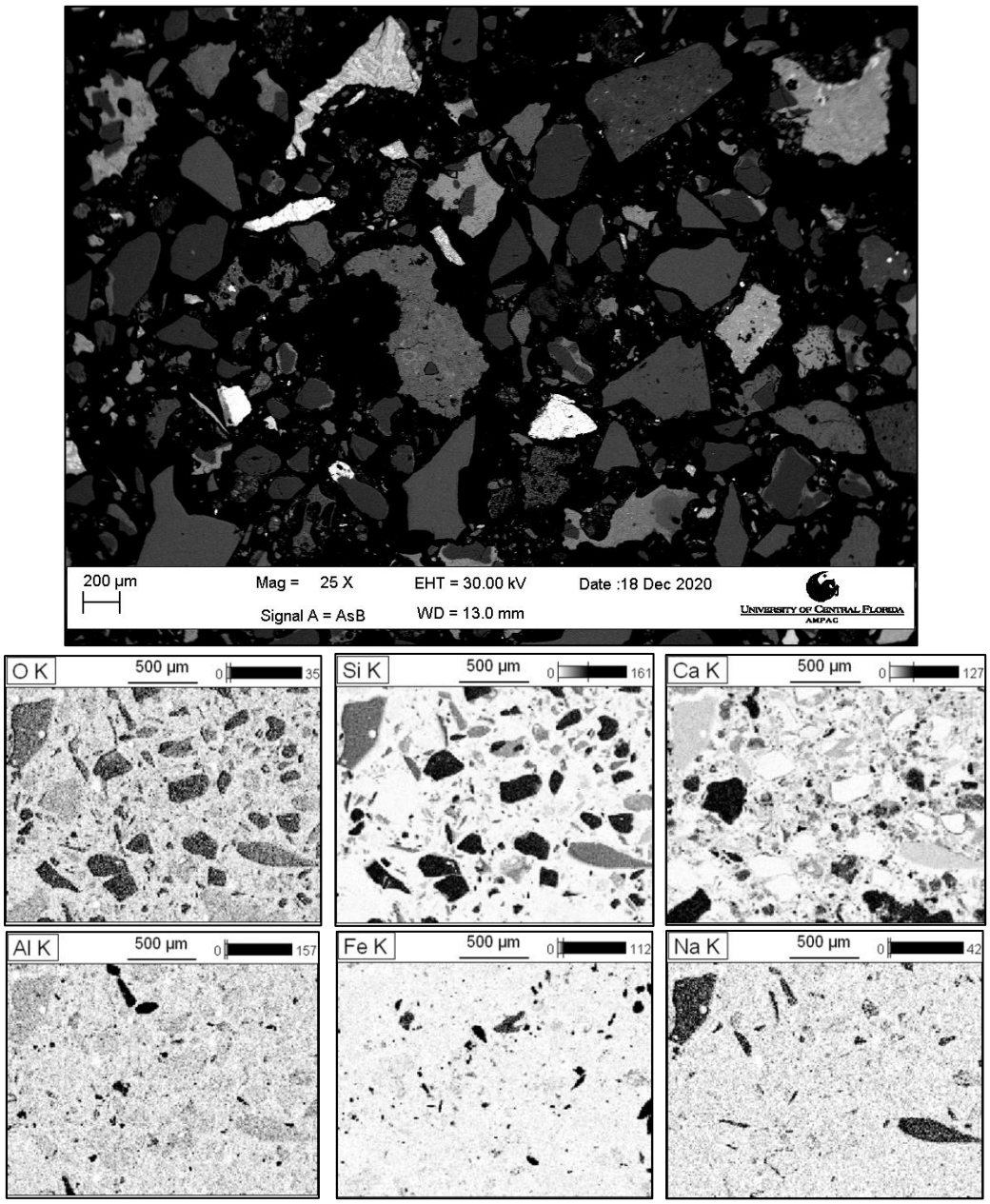

Figure C 14: XEDS Spectral Map Data for MSWIA-8

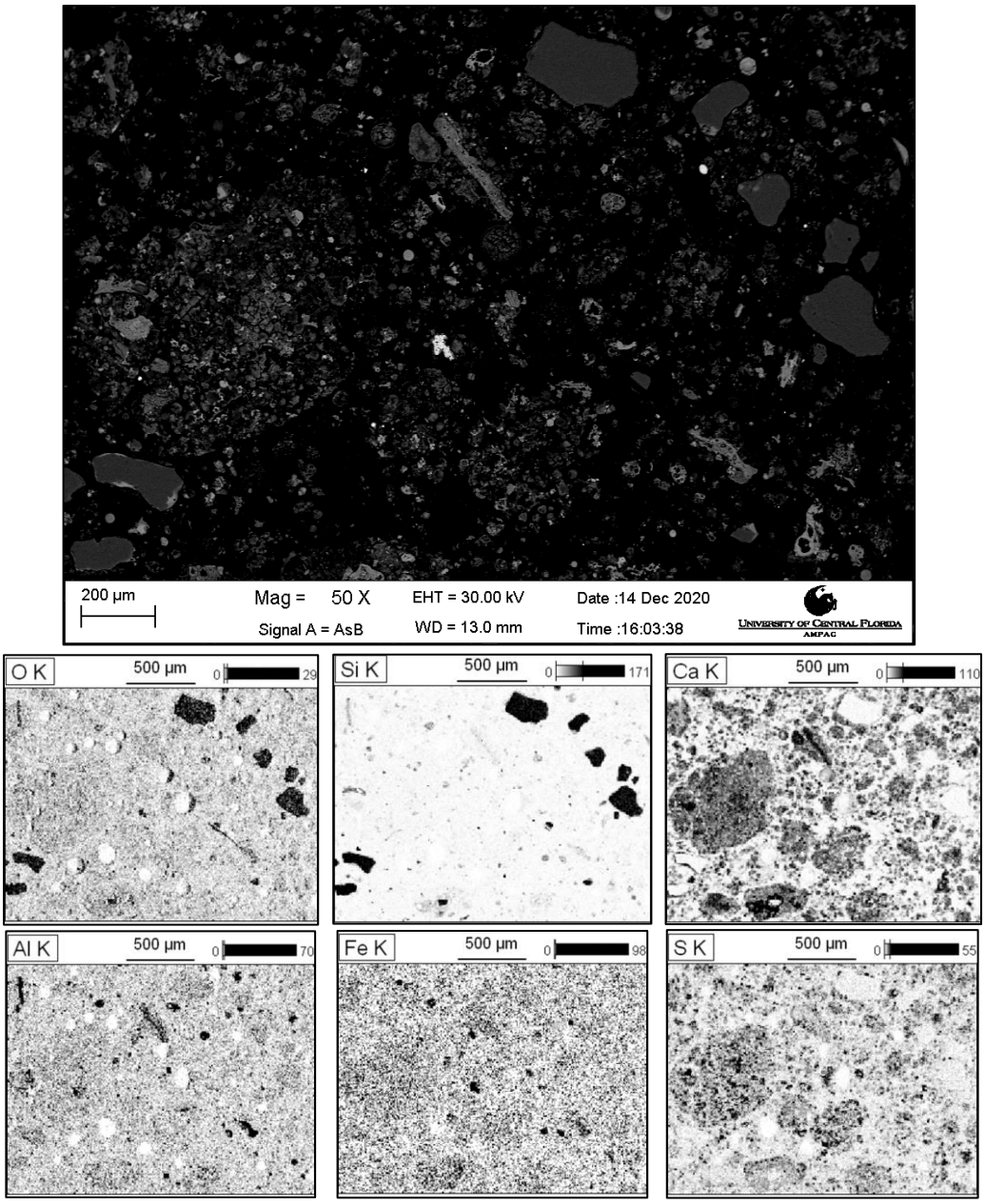

Figure C 15: XEDS Spectral Map Data for MSWIA-9

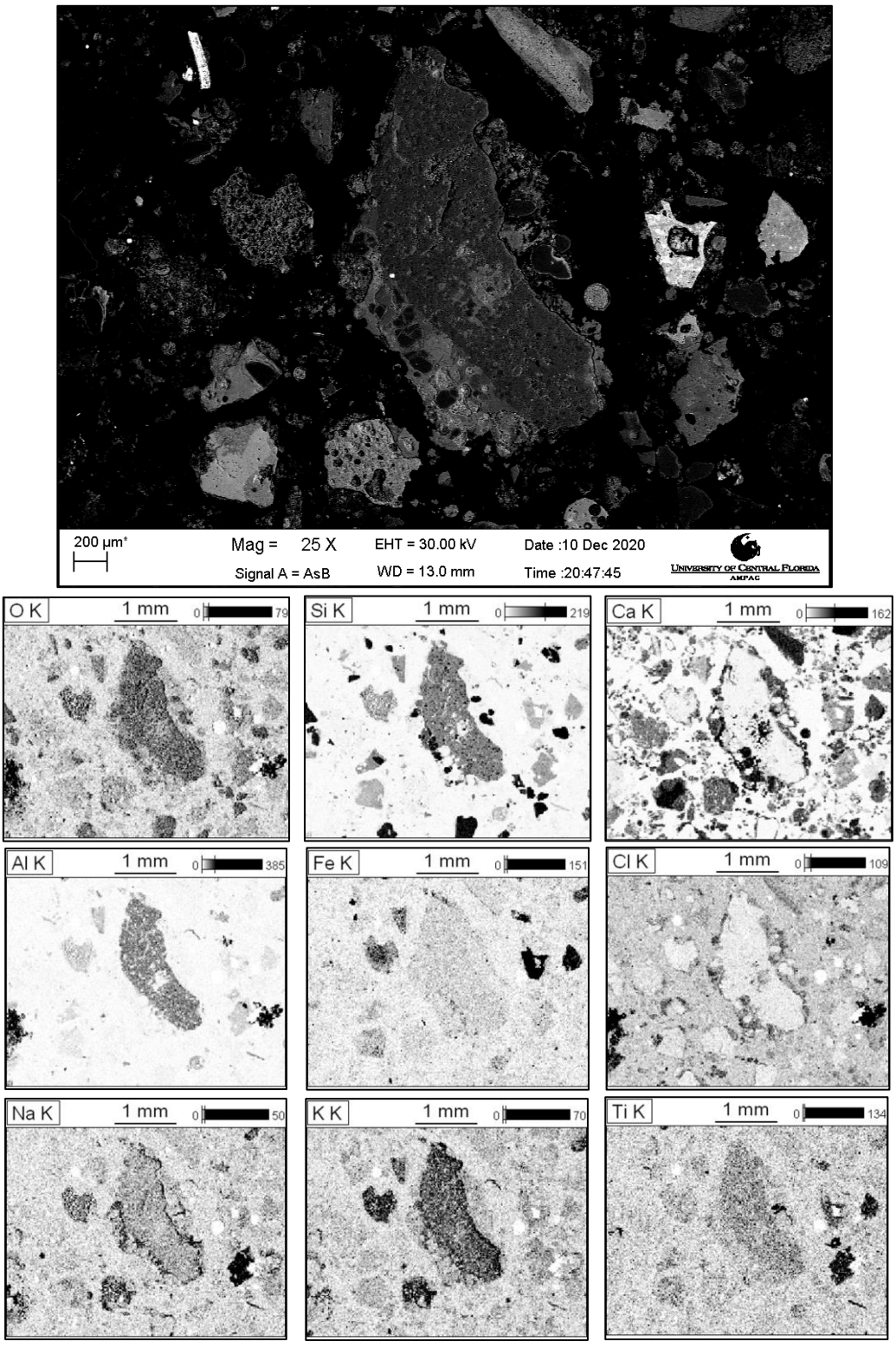

Figure C 16: XEDS Spectral Map Data for MSWIA-10

APPENDIX D: XEDS POINT-AND-SHOOT DATA

Note: Any detected gold (Au) in XEDS spectra is due to sample preparation to ensure conductivity.

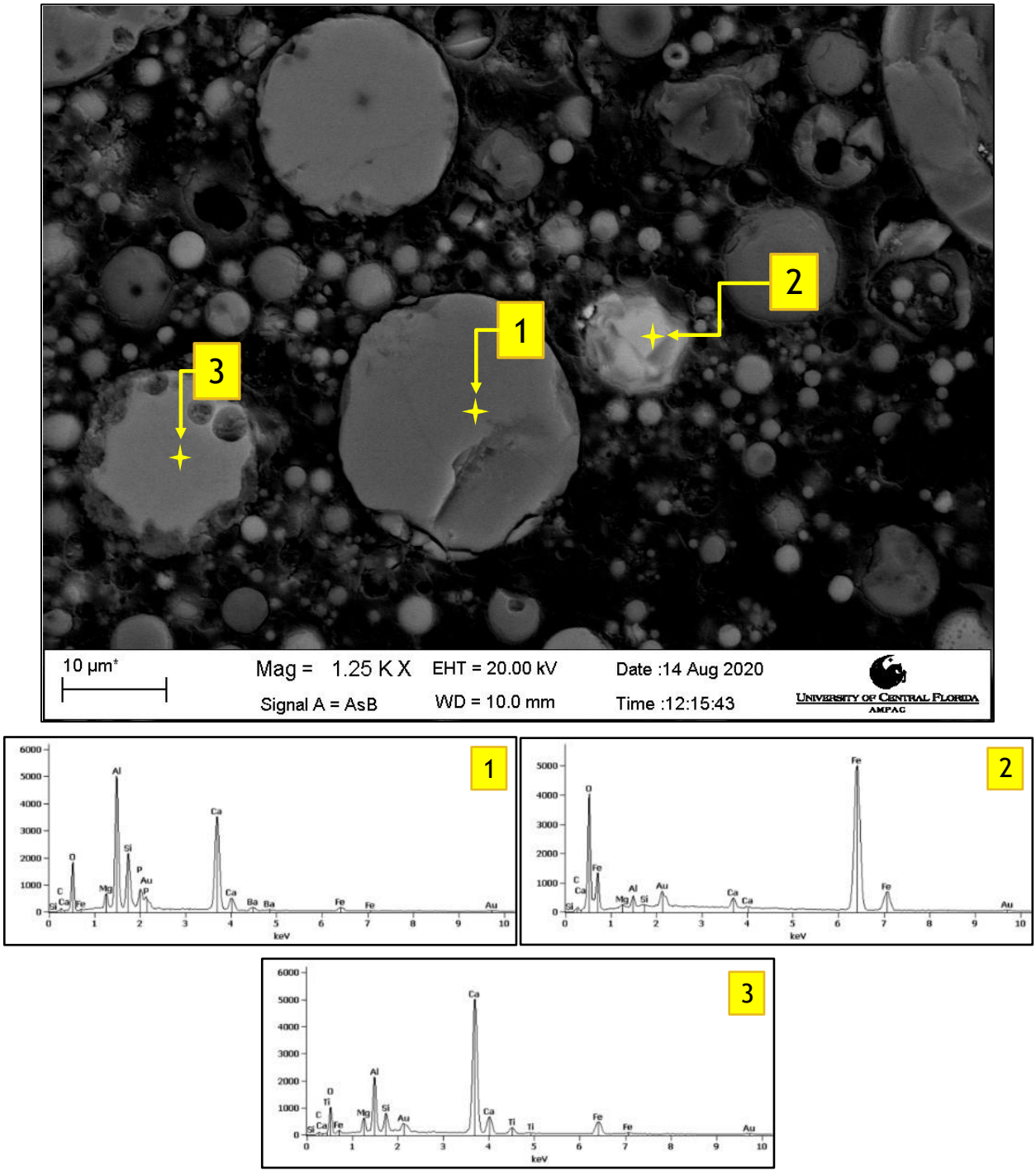

Figure D 1: XEDS Point-and-Shoot Data for CCA-1

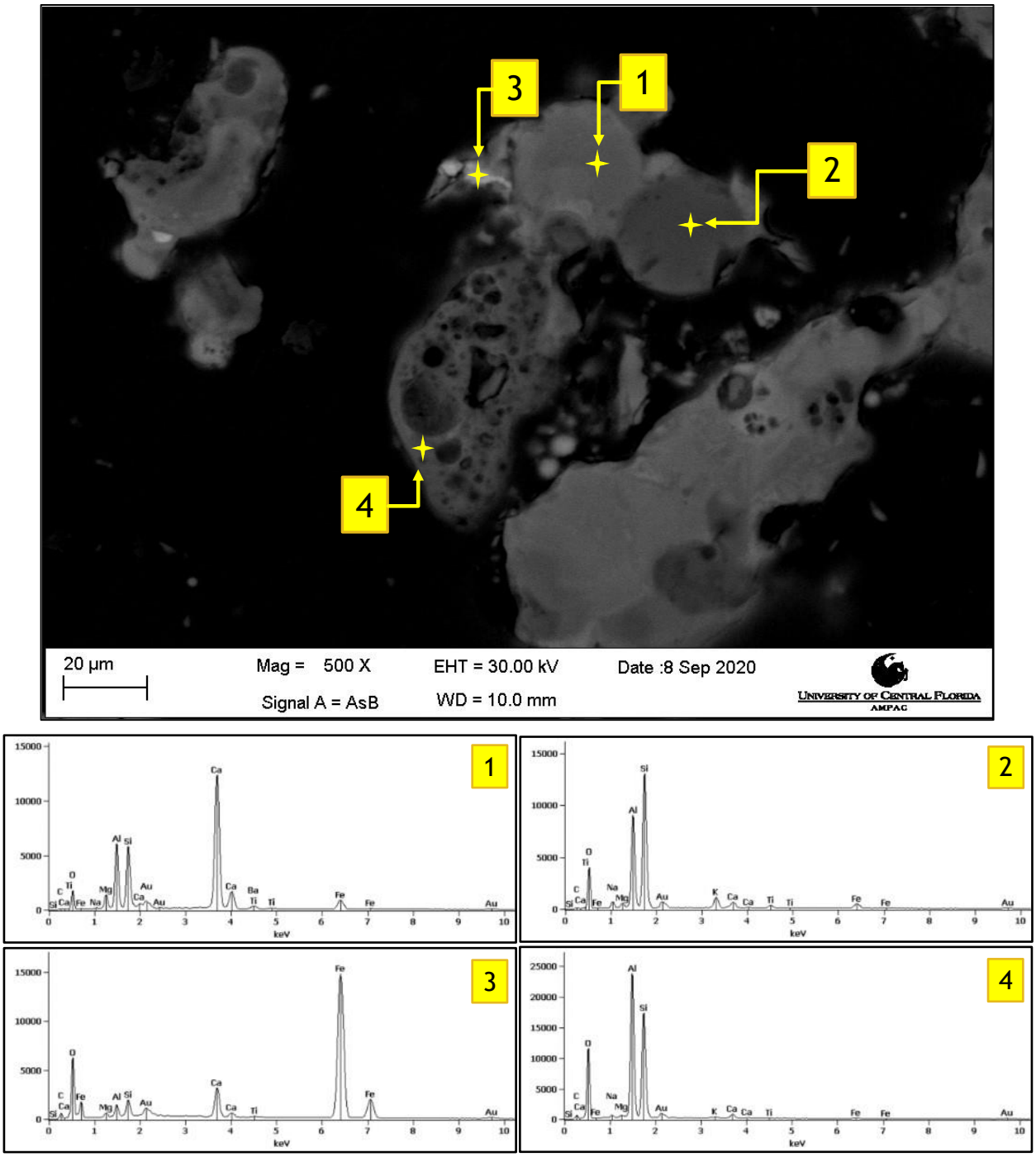

Figure D 2: XEDS Point-and-Shoot Data for CCA-2

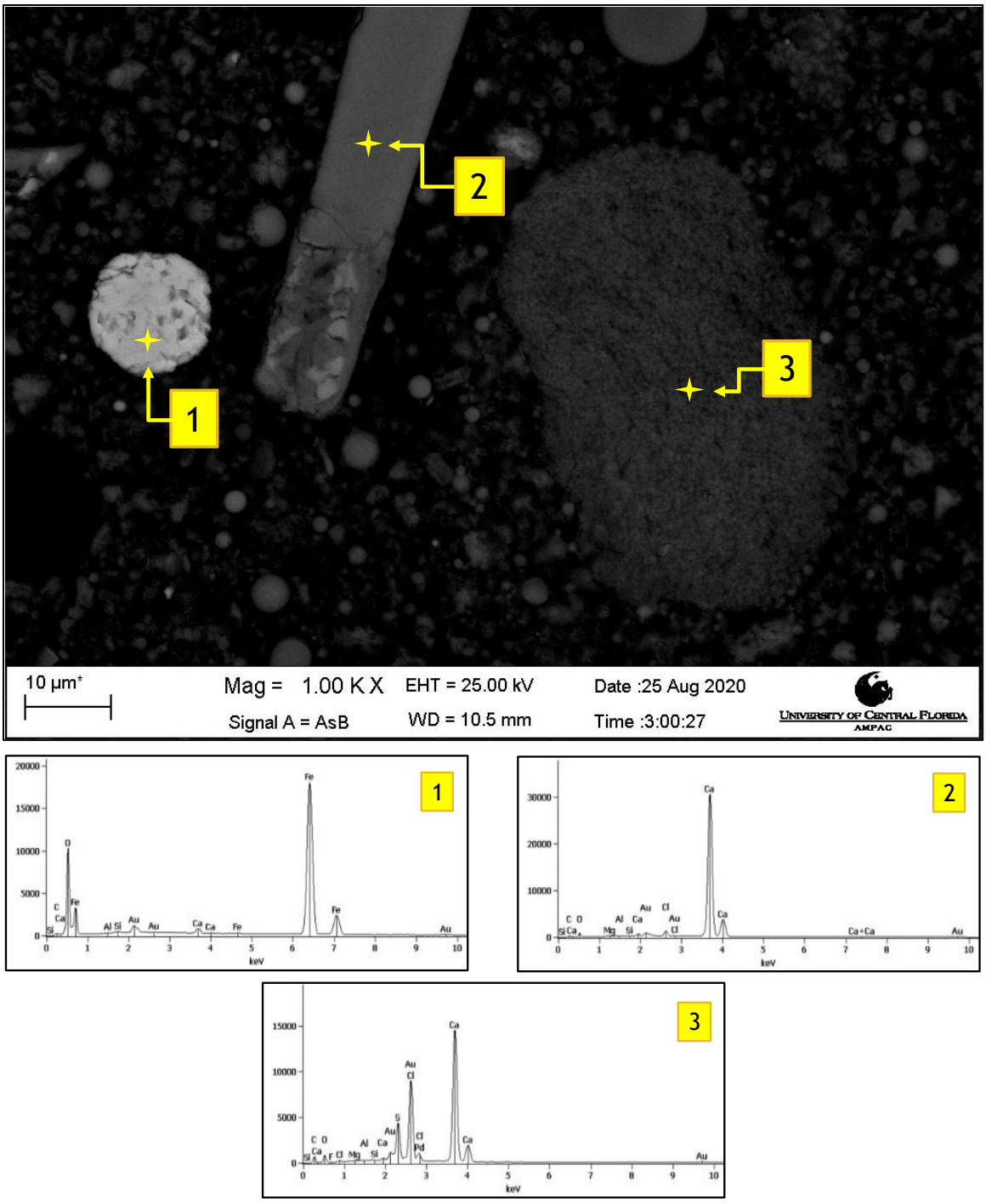

Figure D 3: XEDS Point-and-Shoot Data for CCA-3

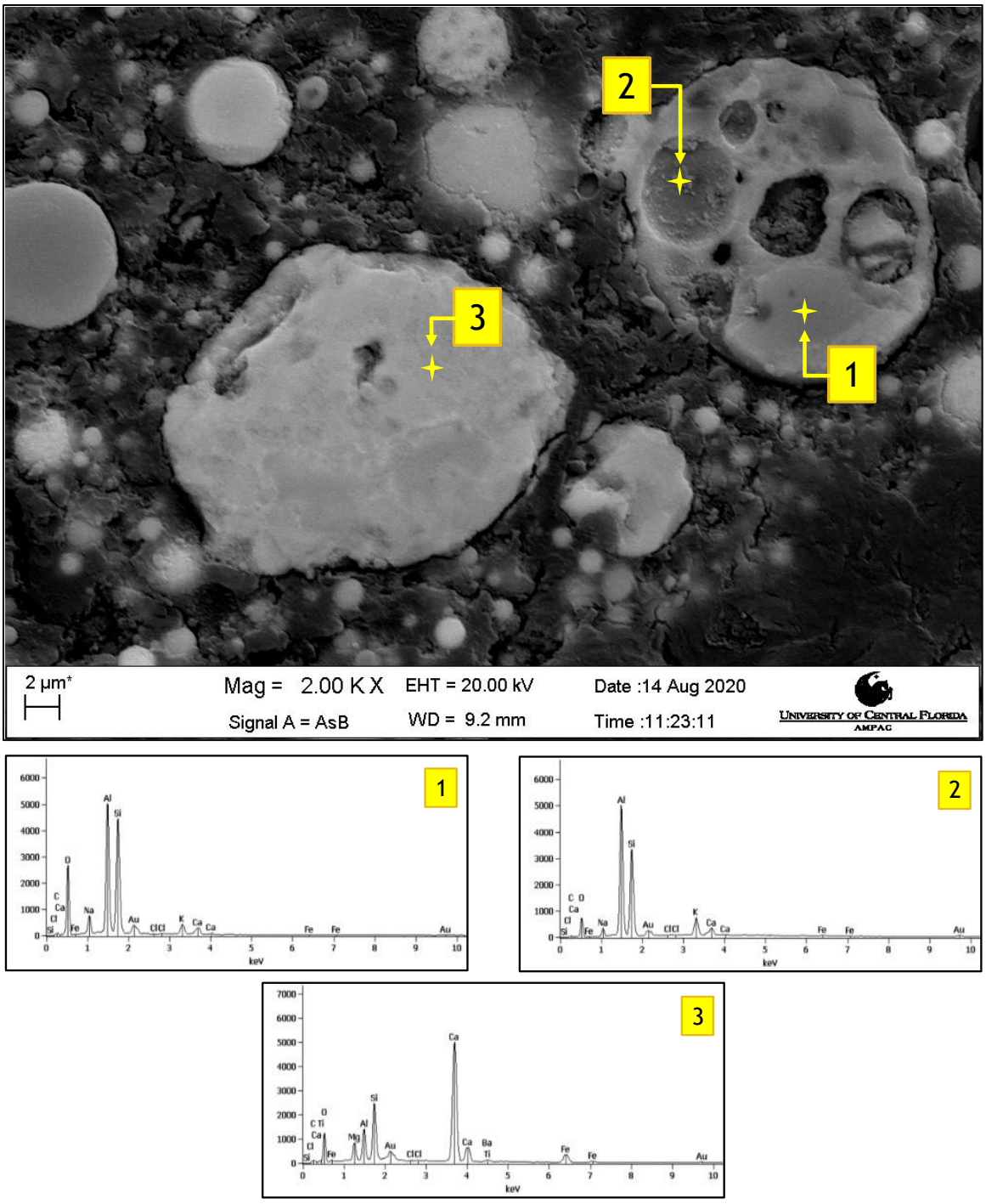

Figure D 4: XEDS Point-and-Shoot Data for CCA-4

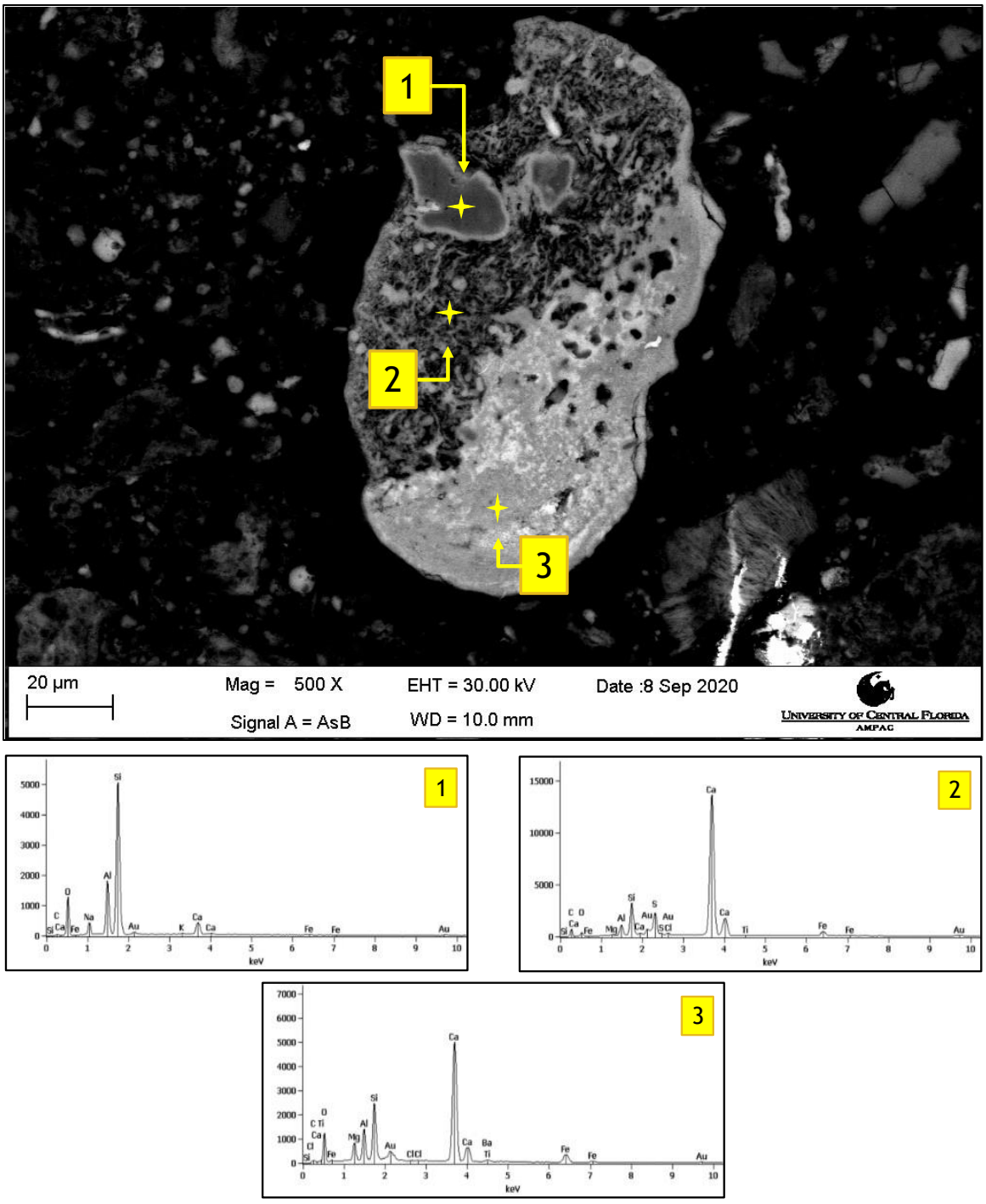

Figure D 5: XEDS Point-and-Shoot Data for CCA-5

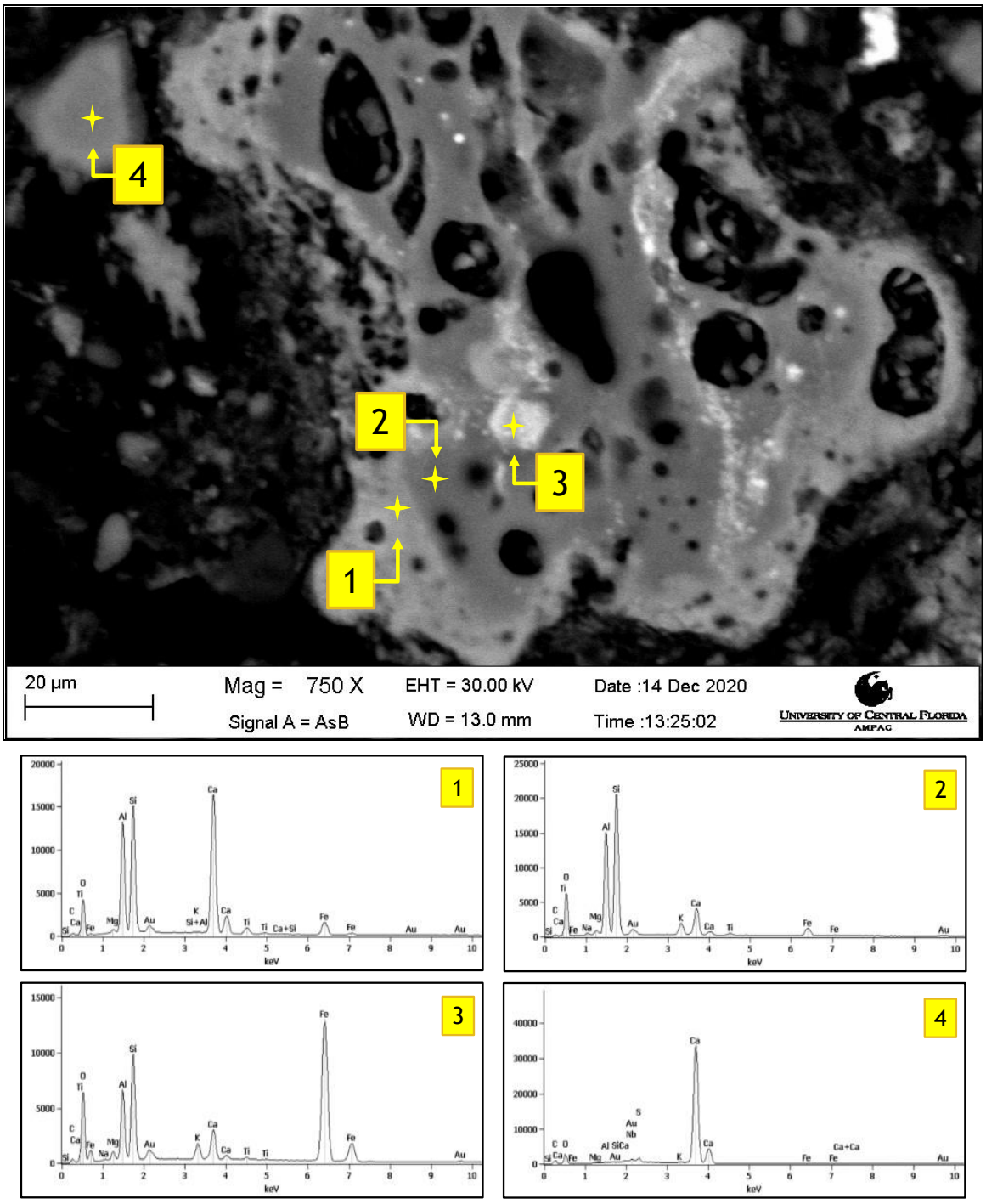

Figure D 6: XEDS Point-and-Shoot Data for CCA-6

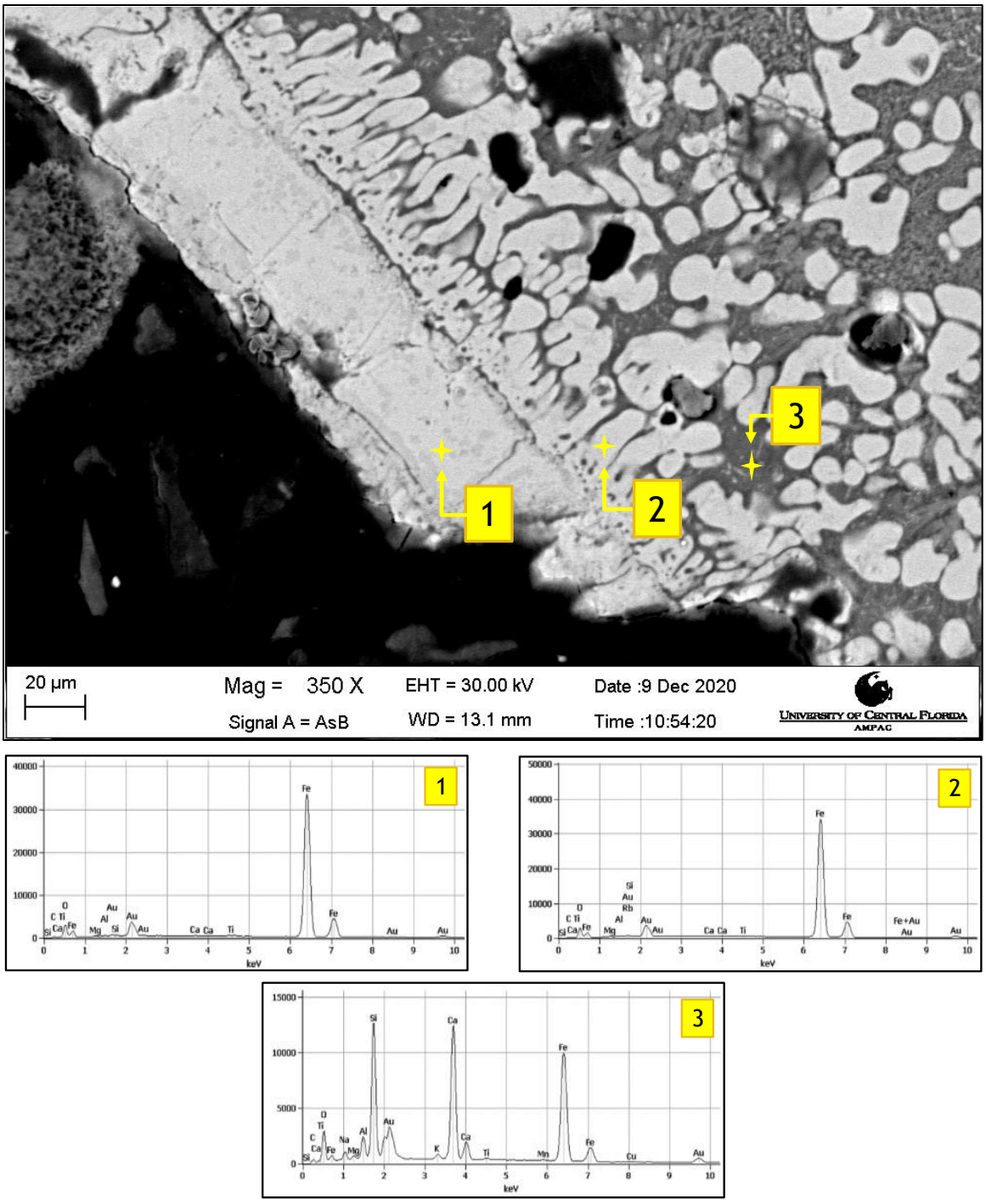

Figure D 7: XEDS Point-and-Shoot Data for MSWIA-1

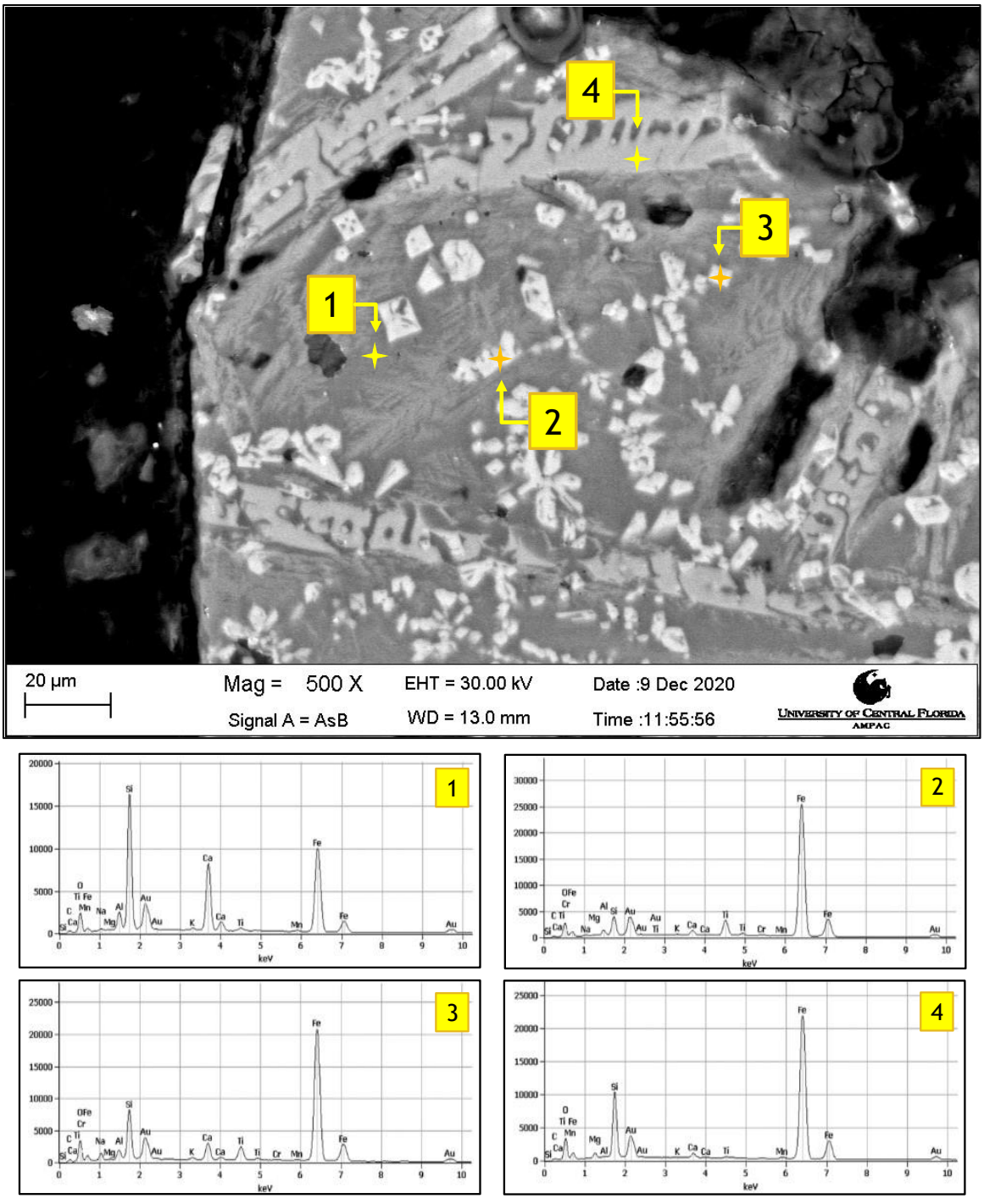

Figure D 8: XEDS Point-and-Shoot Data for MSWIA-2

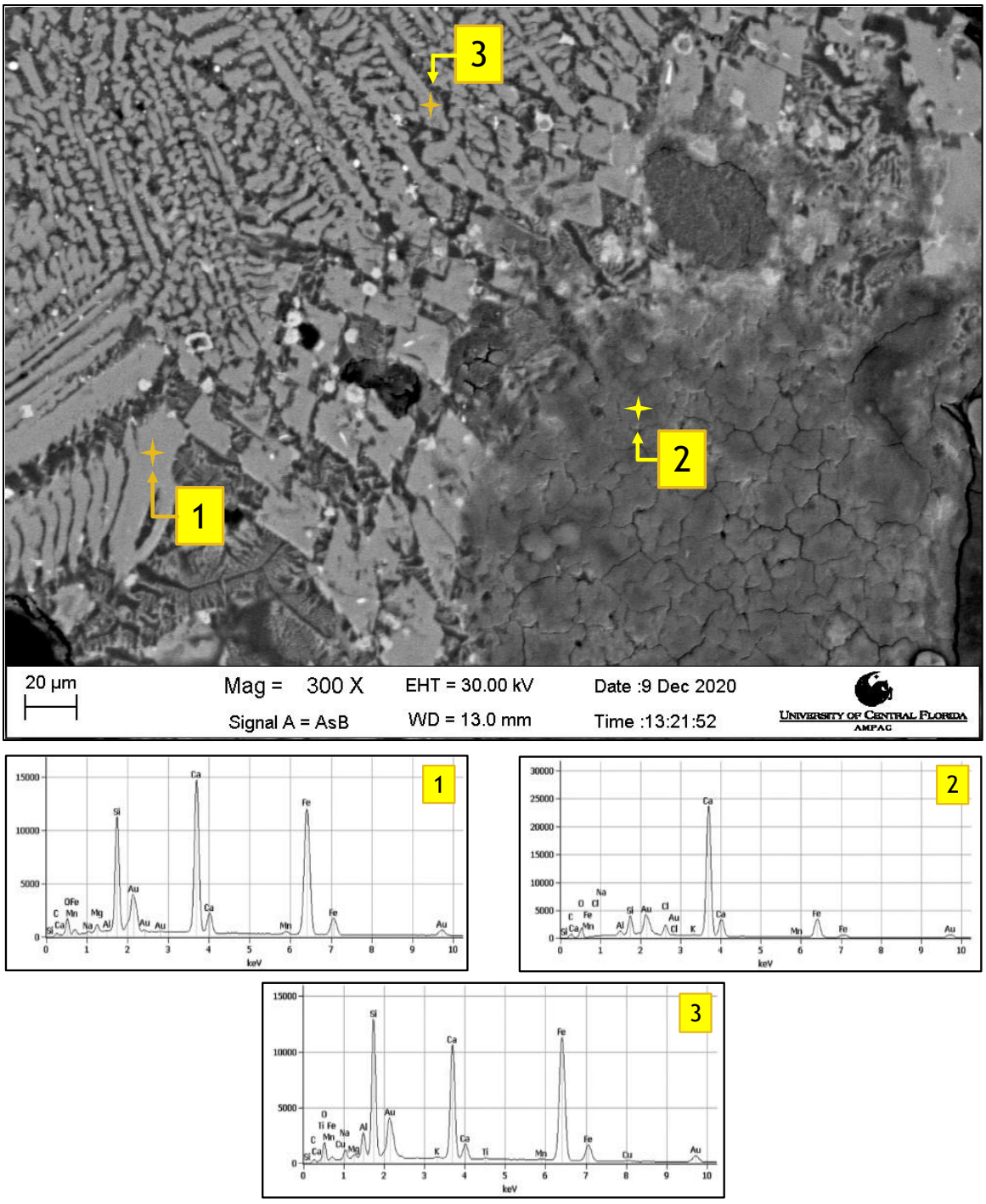

Figure D 9: XEDS Point-and-Shoot Data for MSWIA-3

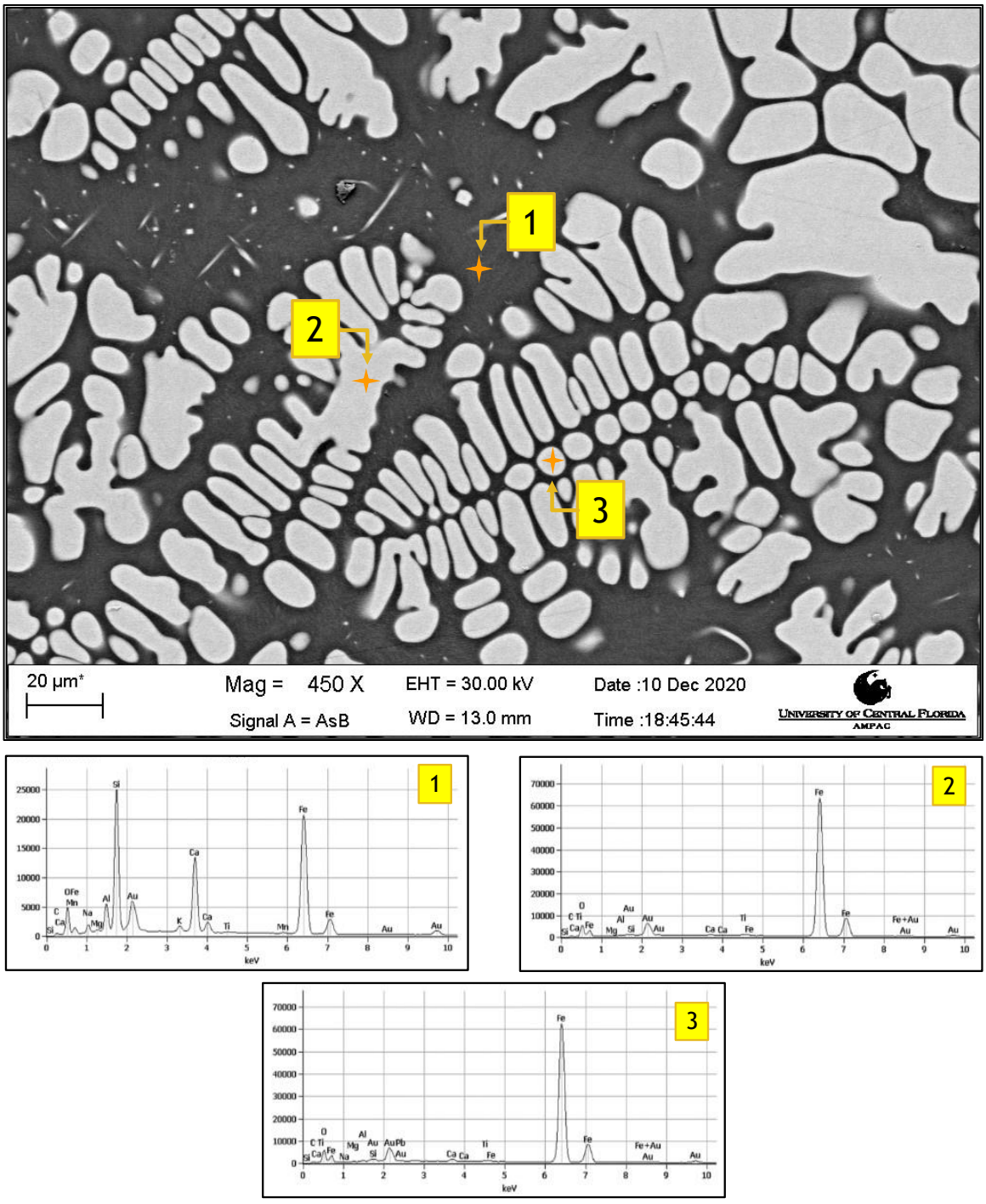

Figure D 10: XEDS Point-and-Shoot Data for MSWIA-4

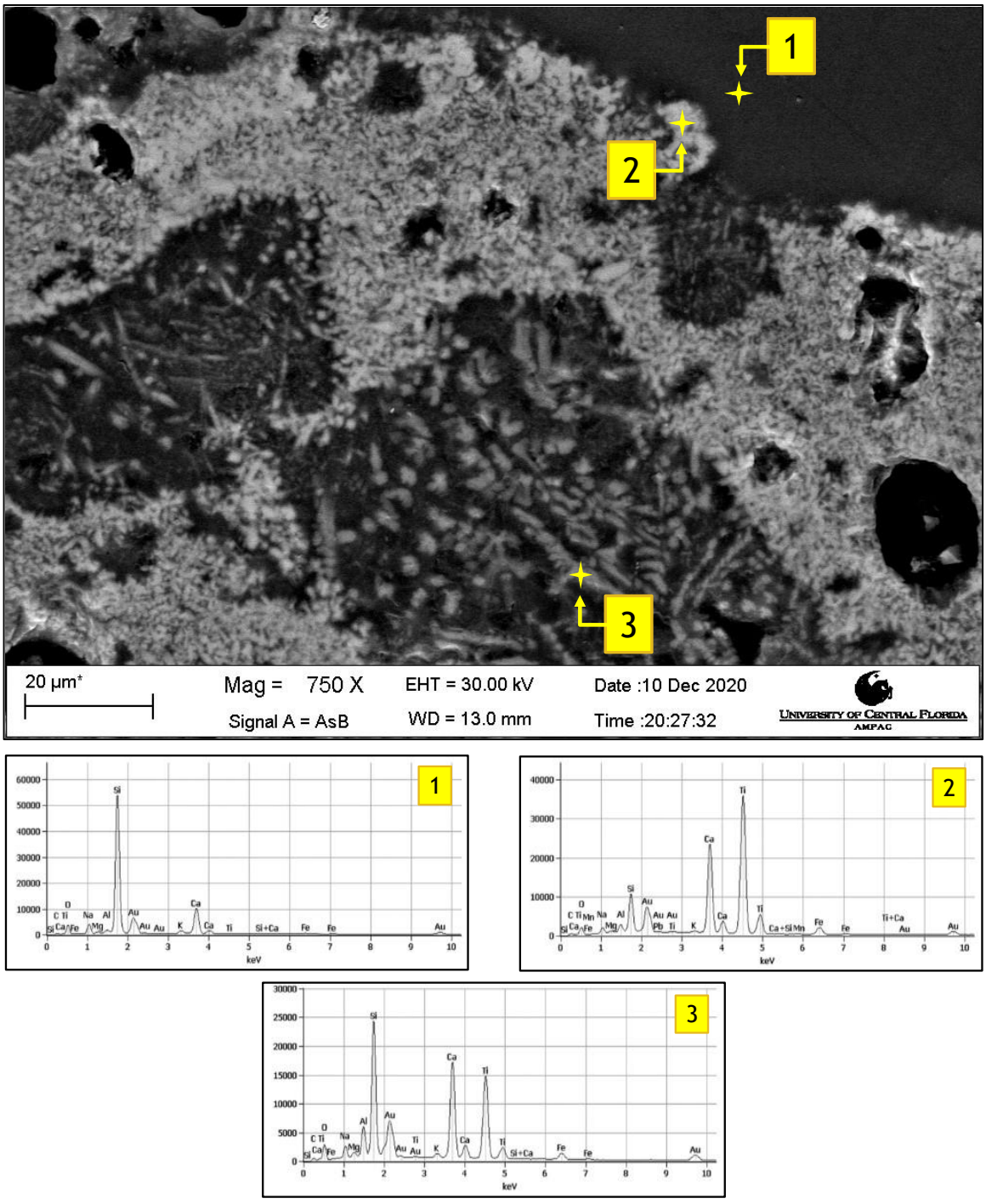

Figure D 11: XEDS Point-and-Shoot Data for MSWIA-5

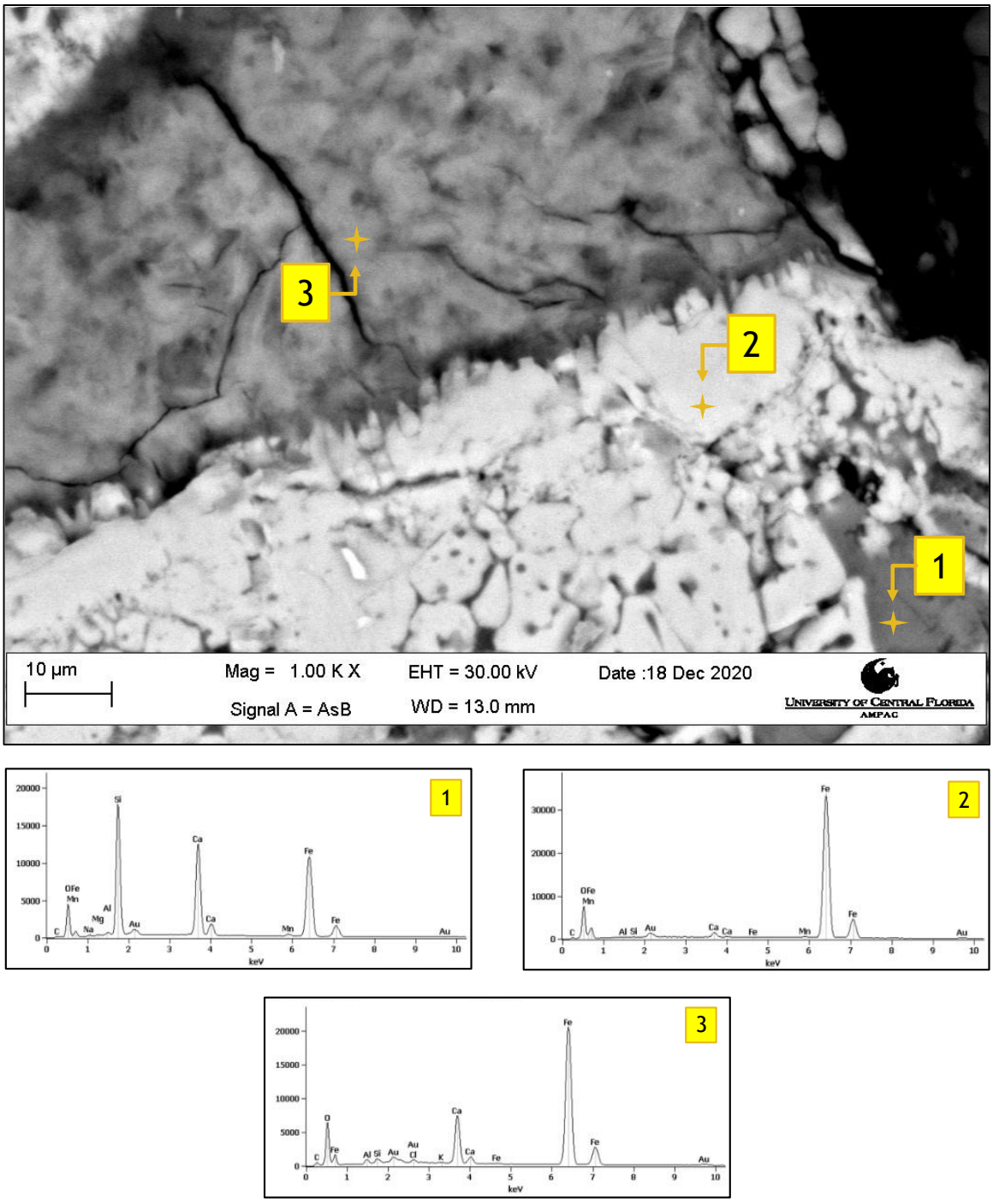

Figure D 12: XEDS Point-and-Shoot Data for MSWIA-6

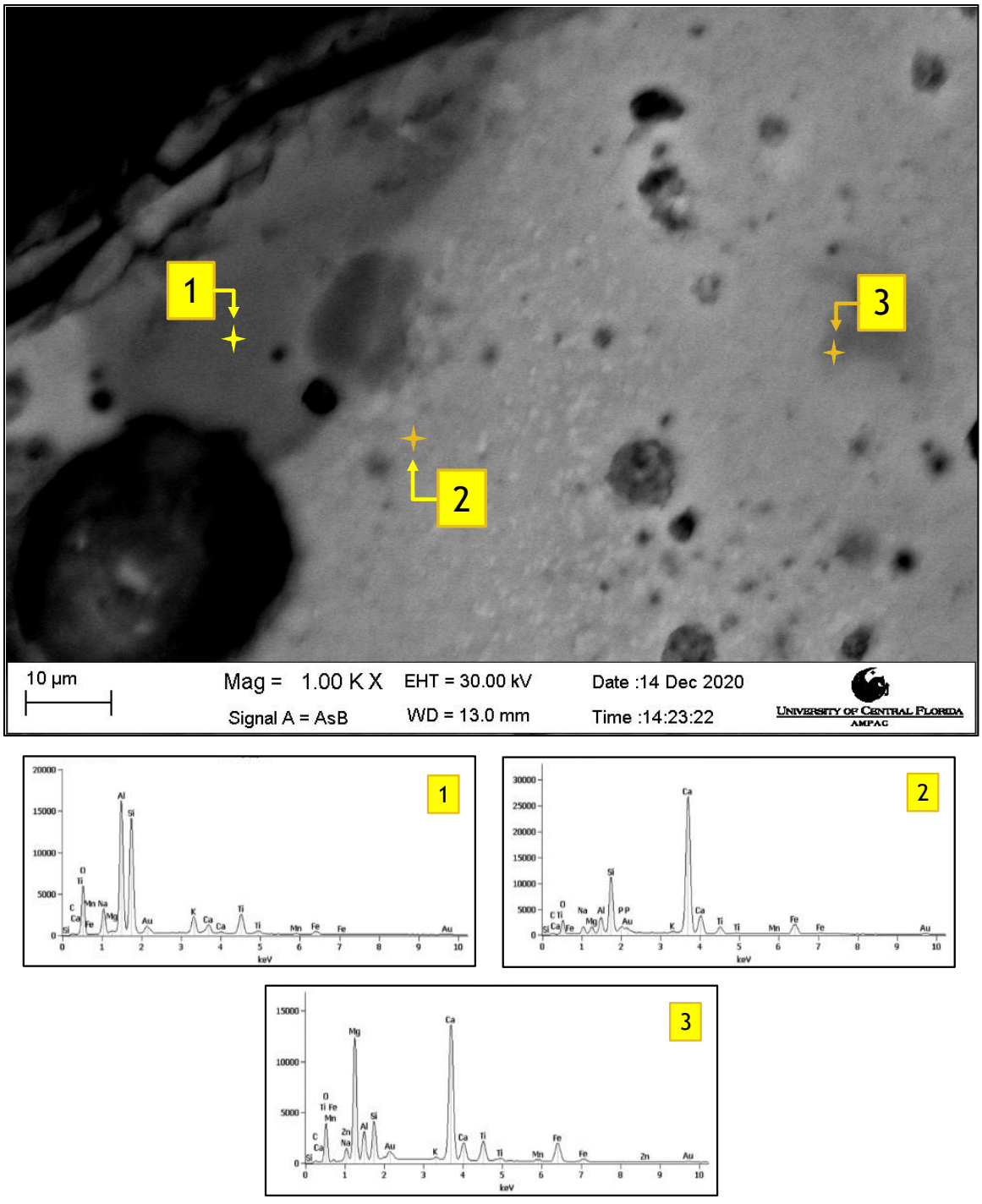

Figure D 13: XEDS Point-and-Shoot Data for MSWIA-7

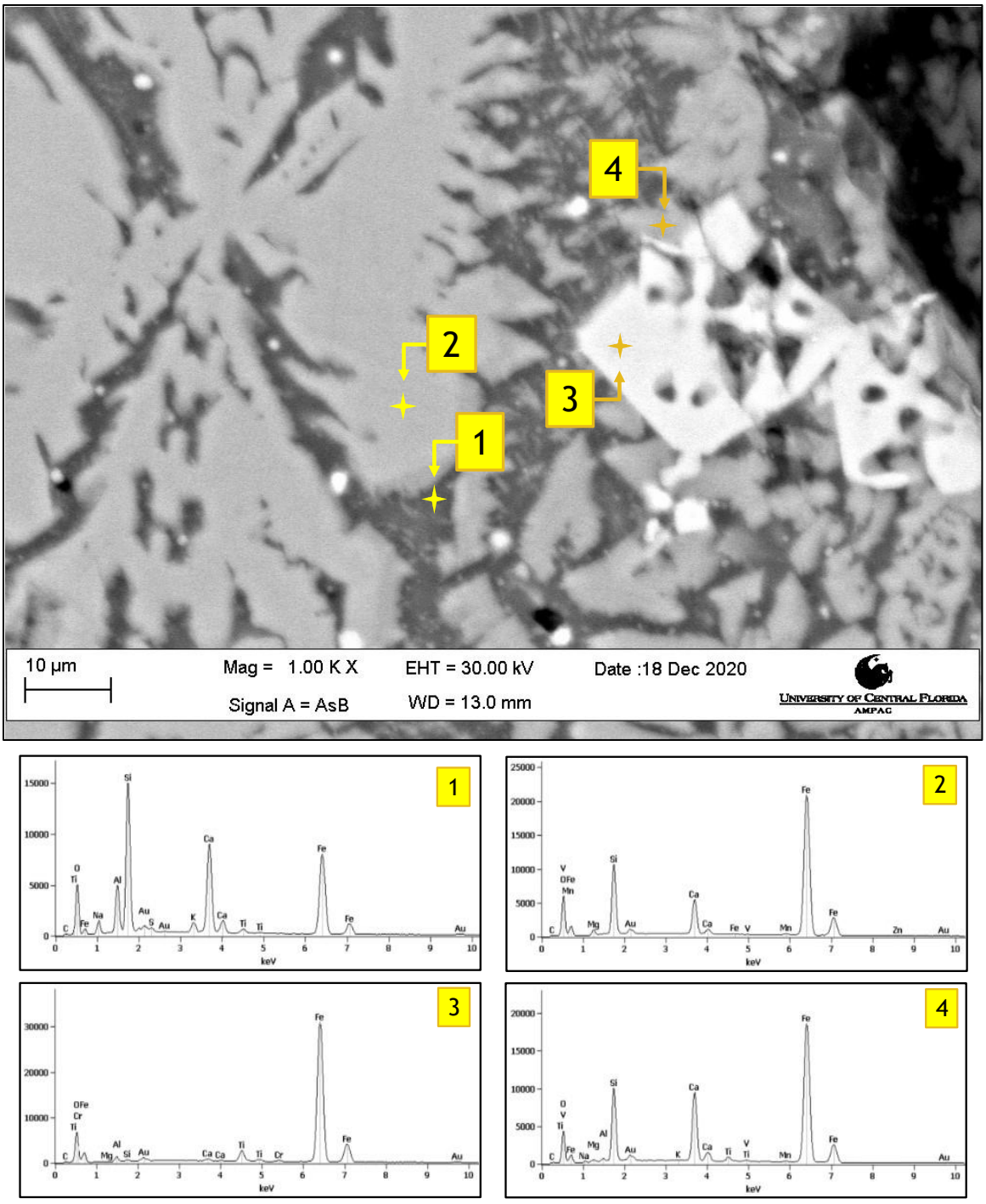

Figure D 14: XEDS Point-and-Shoot Data for MSWIA-8

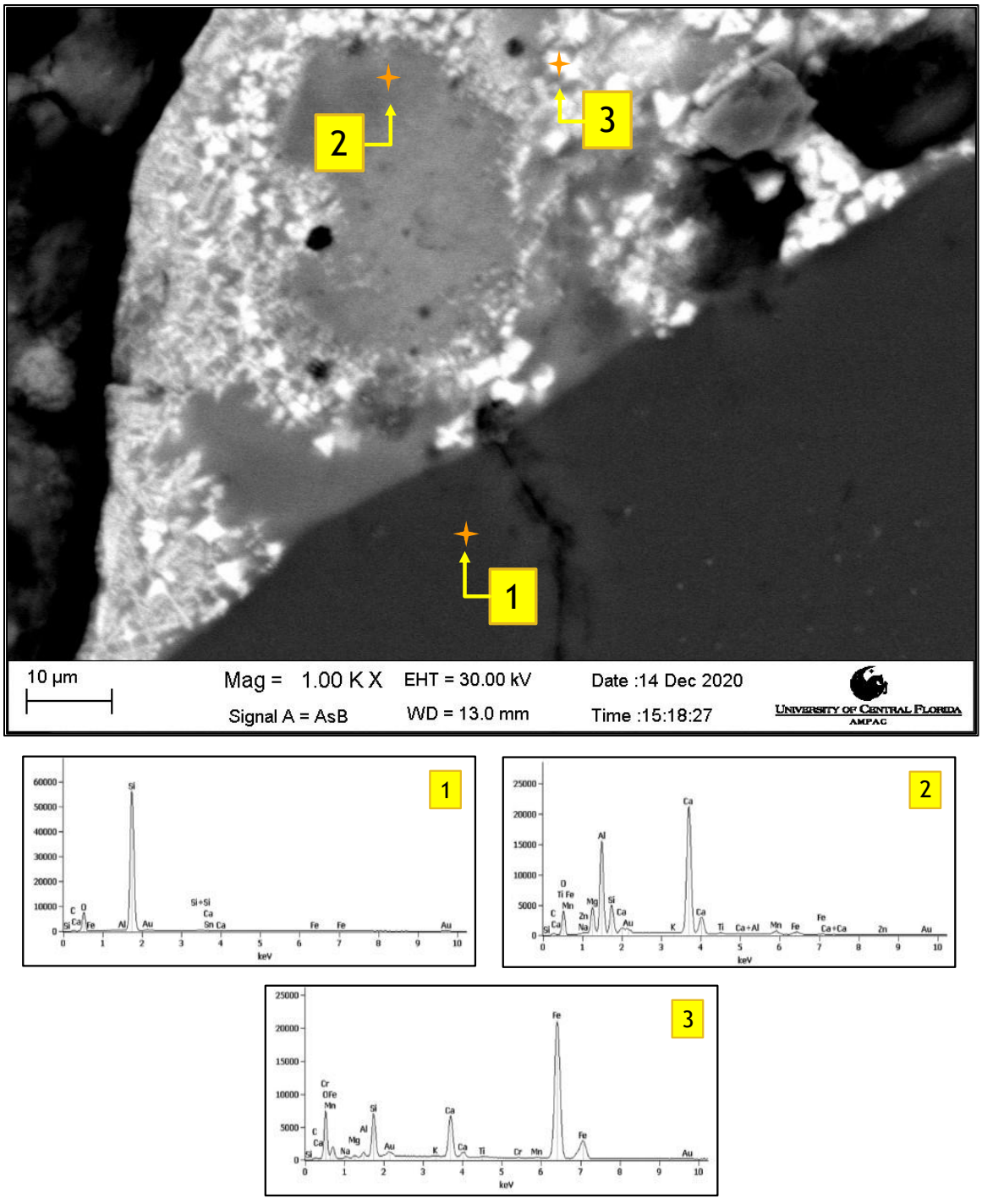

Figure D 15: XEDS Point-and-Shoot Data for MSWIA-9

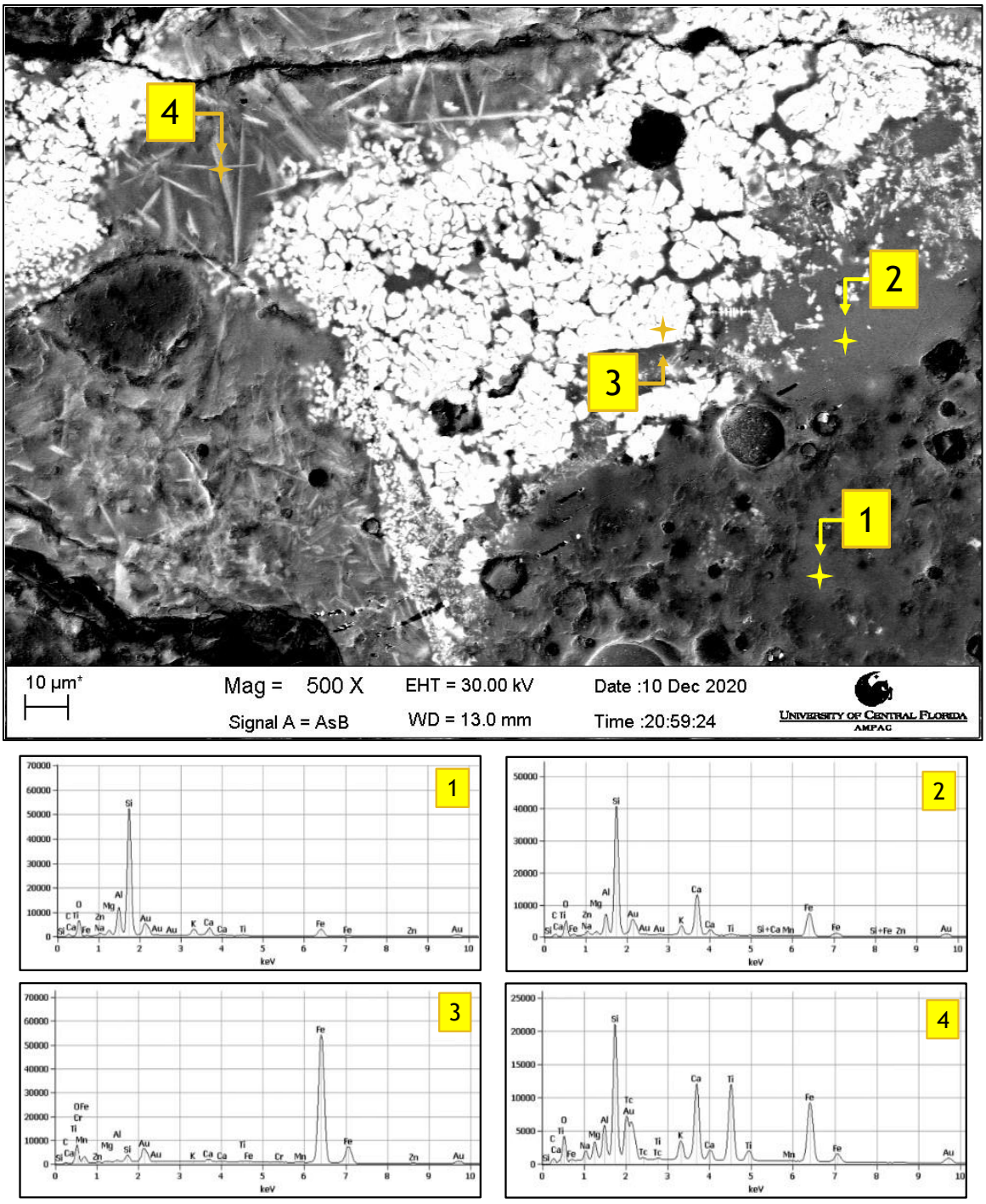

Figure D 16: XEDS Point-and-Shoot Data for MSWIA-10

REFERENCES

N. Alba, S. Gasso, T. Lacorte, and J.M. Baldasano. "Characterization of municipal solid waste incineration residues from facilities with different air pollution control systems." *Journal of the Air & Waste Management Association* 47.11 (1997): 1170-1179.

Adams, Thomas H. 2019. “Coal Combustion Product (CCP) Production & Use Survey Report.” (2019)

An, Jinwoo. “Characterization of Waste-To-Energy (WTE) Bottom and Fly Ashes in Cementitious Materials”. Diss. University of Central Florida, 2015.

Benson, Craig H. "Characteristics of gas and leachate at an elevated temperature landfill." *Geotechnical Frontiers* 2017. (2017). 313-322.

L. Bertonlini, M. Carsana, D. Cassago, A.Q. Curzio, and M. Collepardi. "MSWI ashes as mineral additions in concrete." *Cement and concrete research* 34.10 (2004): 1899-1906.

G.V. Calder and T.D. Stark. "Aluminum reactions and problems in municipal solid waste landfills." *Practice Periodical of Hazardous, Toxic, and Radioactive Waste Management* 14.4 (2010): 258-265.

Chancey, Ryan Thomas. "Characterization of crystalline and amorphous phases and respective reactivities in a class F fly ash." Diss. University of Texas, 2008.

J.M. Chimenos, M. Segarra, M.A. Fernandez, and F. Espiell. "Characterization of the bottom ash in municipal solid waste incinerator." *Journal of hazardous materials* 64.3 (1999): 211-222.

K. Clavier, J.M. Paris, C. Ferraro, E.T. Bueno, C. Tibbetts, and T. Townsend. "Washed waste incineration bottom ash as a raw ingredient in cement production: Implications for lab-scale clinker behavior." *Resources, Conservation and Recycling* 169 (2021): 105513.

Crundwell, Frank K. "On the mechanism of the dissolution of quartz and silica in aqueous solutions." *ACS Omega* 2.3 (2017): 1116-1127.

S. Dontriros, S. Likitlersuang, and D. Janjaroen. "Mechanisms of chloride and sulfate removal from municipal-solid-waste-incineration fly ash (MSWI FA): effect of acid-base solutions." *Waste Management* 101 (2020): 44-53.

J. Fernández, F. Gonzalez, C. Pesquera, A.N. Junior, M.M. Viana, and J. Dweck. "Qualitative and quantitative characterization of a coal power plant waste by TG/DSC/MS, XRF and XRD." *Journal of Thermal Analysis and Calorimetry* 125.2 (2016): 703-710.

F.J. Frandsen, K. Laursen, and S. Arvelakis. "Ash chemistry in MSW incineration plants: Advanced characterization and thermodynamic considerations." Technical Report. CHEC Research Centre at the Dept of Chemical Engineering, Technical University of Denmark, 2004.

Geosyntec Consultants, Inc. “Review of Causes and Mitigation of Subsurface Heating Events in Solid Waste Landfills”. National Risk Management Research Laboratory (NRMRL) of the U.S. Environmental Protection Agency (U.S.EPA), Office of Research and Development (ORD), 2014.

Grillo, Robert J. "Energy recycling–landfill waste heat generation and recovery." Current Sustainable/Renewable Energy Reports 1.4 (2014): 150-156.

Z. Hao, M. Sun, J.J. Ducoste, C. Benson, S. Luettich, M.J. Castaldi, and M. Barlaz. "Heat generation and accumulation in municipal solid waste landfills." *Environmental science & technology* 51.21 (2017): 12434-12442.

K. Inkaew, A. Saffarzadeh, and T. Shimaoka. "Modeling the formation of the quench product in municipal solid waste incineration (MSWI) bottom ash." *Waste Management* 52 (2016): 159-168.

N.H. Jafari, T.D. Stark, and T. Thalhamer. "Progression of elevated temperatures in municipal solid waste landfills." *Journal of Geotechnical and Geoenvironmental Engineering* 143.8 (2017): 05017004.

A.M. Joseph, R. Snellings, P. Van den Heede, S. Matthys, and N. De Belie. "The use of municipal solid waste incineration ash in various building materials: a Belgian point of view." *Materials* 11.1 (2018): 141.

Joslyn, Ryan. "Characterization of Florida Landfills with Elevated Temperatures." Thesis. University of Central Florida, 2019.

C.S. Kirby and J.D. Rimstidt. "Interaction of municipal solid waste ash with water." *Environmental Science & Technology* 28.3 (1994): 443-451.

S. Klemm, S. Strobl, and R. Haubner, "Mediaeval Iron Smelting in the Area of the Iron Mountain at Eisenerz, Styria." *Proceedings for the 2nd Mining in European History Conference of the SFB-HIMAT*, Innsbruck, 7-10 November 2012. 2012.

C.H.K Lam, A.W.M. Ip, J.P. Barford, and G. McKay. "Use of incineration MSW ash: a review." *Sustainability* 2.7 (2010): 1943-1968.

Y. Liu, L. Zheng, X. Li, and S. Xie. "SEM/EDS and XRD characterization of raw and washed MSWI fly ash sintered at different temperatures." *Journal of Hazardous Materials* 162.1 (2009): 161-173.

C.J. Lynn, G.S. Ghataora, and R.K.D. OBE. "Municipal incinerated bottom ash (MIBA) characteristics and potential for use in road pavements." *International Journal of Pavement Research and Technology* 10.2 (2017): 185-201.

D.A.R. Meyer-Dombard, J.E. Bogner, and J. Malas. "A Review of Landfill Microbiology and Ecology: A Call for Modernization With ‘Next Generation’Technology." *Frontiers in Microbiology* 11 (2020): 1127.

A. Narode, M. Pour-Ghaz, J.J. Ducoste, and M. Barlaz. "Measurement of heat release during hydration and carbonation of ash disposed in landfills using an isothermal calorimeter." *Waste Management* 124 (2021): 348-355.

National Resource Council. "Waste incineration and public health." Technical Report, 2000.

I. Pane, and W. Hansen. "Investigation of blended cement hydration by isothermal calorimetry and thermal analysis." *Cement and Concrete Research* 35.6 (2005): 1155-1164.

Phua, Zhenghui, et al. "Characteristics of incineration ash for sustainable treatment and reutilization." *Environmental Science and Pollution Research* 26.17 (2019): 16974-16997.

C.S. Psomopoulos, A. Bourka, and N.J. Themelis. "Waste-to-energy: A review of the status and benefits in USA." *Waste management* 29.5 (2009): 1718-1724.

D. Reinhart, R. Joslyn, and C.T. Emrich. "Characterization of Florida, US landfills with elevated temperatures." *Waste Management* 118 (2020): 55-61.

A. Saffarzadeh, T. Shimaoka, Y. Wei, and K.H. Gardner. "Impacts of natural weathering on the transformation/neoformation processes in landfilled MSWI bottom ash: a geoenvironmental perspective." *Waste Management* 31.12 (2011): 2440-2454.

A. Saffarzadeh, and T. Shimaoka. "Occurrence and Significance of Secondary Iron-rich Products in Landfilled MSWI Bottom Ash." *International Journal of Waste Resources* 4.150 (2014): 2.

A. Saffarzadeh, N. Arumugam, and T. Shimaoka. "Aluminum and aluminum alloys in municipal solid waste incineration (MSWI) bottom ash: A potential source for the production of hydrogen gas." *International Journal of Hydrogen Energy* 41.2 (2016): 820-831.

R.M. Santos, G. Martens, M. Salman, and O. Cizer. "Comparative study of ageing, heat treatment and accelerated carbonation for stabilization of municipal solid waste incineration bottom ash in view of reducing regulated heavy metal/metalloid leaching." *Journal of Environmental Management* 128 (2013): 807-821.

S. Schupp, F.B. De la Cruz, Q. Cheng, and D.F. Call. "Evaluation of the Temperature Range for Biological Activity in Landfills Experiencing Elevated Temperatures." *ACS ES&T Engineering* (2020).

C. Speiser, T. Baumann, and R. Niessner. "Morphological and chemical characterization of calcium-hydrate phases formed in alteration processes of deposited municipal solid waste incinerator bottom ash." *Environmental Science & Technology* 34.23 (2000): 5030-5037.

C. Speiser, T. Baumann, and R. Niessner. "Characterization of municipal solid waste incineration (MSWI) bottom ash by scanning electron microscopy and quantitative energy dispersive X-ray microanalysis (SEM/EDX)." *Fresenius' Journal of Analytical Chemistry* 370.6 (2001): 752-759.

S. Tupsakhare, T. Moutushi, and M.J. Castaldi. "The impact of pressure, moisture and temperature on pyrolysis of municipal solid waste under simulated landfill conditions and

relevance to the field data from elevated temperature landfill." *Science of The Total Environment* 723 (2020): 138031.

U.S. Environmental Protection Agency (U.S. EPA) (2019) “Energy Recovery from the Combustion of Municipal Solid Waste (MSW).”

U.S. Environmental Protection Agency (U.S. EPA), “Advancing Sustainable Materials Management: 2018 Fact Sheet.” (2020).

U.S. Energy Information Administration (U.S. EIA) - Independent Statistics and Analysis, “Biomass Explained: Waste-to-Energy (MSW).” EIA, Nov. 2020, www.eia.gov/energyexplained/biomass/waste-to-energy.php.

I. Vateva and D Laner. "Grain-Size Specific Characterization and Resource Potentials of Municipal Solid Waste Incineration (MSWI) Bottom Ash: A German Case Study." *Resources* 9.6 (2020): 66.

K.S. Wang, K.L. Lin, T.Y. Lee, and B.Y. Tzeng. "The hydration characteristics when C2S is present in MSWI fly ash slag." *Cement and Concrete Composites* 26.4 (2004): 323-330.

Y. Wei, T. Shimaoka, and A. Saffarzadeh. "Mineralogical characterization of municipal solid waste incineration bottom ash with an emphasis on heavy metal-bearing phases." *Journal of Hazardous Materials* 187.1-3 (2011): 534-543.

Y. Xia, H. Zhang, K. Phoungthong, D.X. Shi, and W.H. Shen. "Leaching characteristics of calcium-based compounds in MSWI Residues: From the viewpoint of clogging risk." *Waste Management* 42 (2015): 93-100.

J. Yu, L. Sun, J. Xiang, L. Jin, and S. Hu. "Physical and chemical characterization of ashes from a municipal solid waste incinerator in China." *Waste Management & Research* 31.7 (2013): 663-673.